Aberration Free Extended Depth of Field Microscopy

A thesis submitted for the Degree of Doctor of Philosophy
at the University of Oxford

Edward Botcherby
St. Hugh's College

Michaelmas Term, 2007

Edward Botcherby
St. Hugh's College

Thesis submitted for D. Phil. Degree
Michaelmas term, 2007

Abstract

In recent years, the confocal and two photon microscopes have become ubiquitous tools in life science laboratories. The reason for this is that both these systems can acquire three dimensional image data from biological specimens. Specifically, this is done by acquiring a series of two-dimensional images from a set of equally spaced planes within the specimen. The resulting image stack can be manipulated and displayed on a computer to reveal a wealth of information. These systems can also be used in time lapse studies to monitor the dynamical behaviour of specimens by recording a number of image stacks at a sequence of time points. The time resolution in this situation is, however, limited by the maximum speed at which each constituent image stack can be acquired. Various techniques have emerged to speed up image acquisition and in most practical implementations a single, in-focus, image can be acquired very quickly. However, the real bottleneck in three dimensional imaging is the process of refocusing the system to image different planes. This is commonly done by physically changing the distance between the specimen and imaging lens, which is a relatively slow process. It is clear with the ever-increasing need to image biologically relevant specimens quickly that the speed limitation imposed by the refocusing process must be overcome.

This thesis concerns the acquisition of data from a range of specimen depths without requiring the specimen to be moved. A new technique is demonstrated for two photon microscopy that enables data from a whole range of specimen depths to be acquired simultaneously so that a single two dimensional scan records extended depth of field image data directly. This circumvents the need to acquire a full three dimensional image stack and hence leads to a significant improvement in the temporal resolution for acquiring such data by more than an order of magnitude.

In the remainder of this thesis, a new microscope architecture is presented that enables scanning to be carried out in three dimensions at high speed without moving the objective lens or specimen. Aberrations introduced by the objective lens are compensated by the introduction of an equal and opposite aberration with a second lens within the system enabling diffraction limited performance over a large range of specimen depths. Focusing is achieved by moving a very small mirror, allowing axial scan rates of several kHz; an improvement of some two orders of magnitude. This approach is extremely general and can be applied to any form of optical microscope with the very great advantage that the specimen is not disturbed. This technique is developed theoretically and experimental results are shown that demonstrate its potential application to a broad range of sectioning methods in microscopy.

Acknowledgements

I would like to take this opportunity to thank those who have advised, supported, and encouraged me during the course of my D. Phil. in Oxford. I would especially like to thank my supervisor, Prof. Tony Wilson, without whose unwavering support, encouragement, and guidance, this thesis would not have been possible. I should also like to thank Tony for his tireless provision of reference letters in my support. I am indebted to both Dr. Rimas Juškaitis and Dr. Martin Booth who I have had the privilege to work alongside during the course of this program and would like to thank them for their patience, advice and instruction in all matters experimental and theoretical.

I would also like to express my gratitude to Dr. Richard Cook and Prof. Tim Watson from the School of Dentistry, Biomaterials Department at the Guy's, King's College and St Thomas' Hospitals' School of Medicine and Dentistry. My funding was provided entirely by a grant from the Medical Research Council / Department of Health held by Dr. Richard Cook. It has been a pleasure to work as part of this collaboration between the London and Oxford groups. My thanks go to Richard and Tim for their kind support, enthusiasm and fruitful discussions over the past few years.

I am indebted to all my friends in Oxford for having made my time here such an enriching experience. In particular, I would like to thank Prof. Steve Elston, Dr. Zsolt Laczik, Maynard Marrion, Claudius Kischka, Kate Grieve, Michael Schwertner and Harald Baumann. I should also like to thank Prof. Chris Foot, from the Department of Physics, for his sound advice and for providing me with the opportunity to teach so many undergraduate students at St. Peter's College.

I should also like to mention Kilian Weinberger and Delphine Débarre, whose enthusiasm for scientific research has been an inspiration. Special thanks go to Katharina Lewis for her support and encouragement over the years as well as to Simon Fox with whom I have spent many entertaining hours over the past fifteen years.

Most of all, thanks must go to my parents to whom I am truly grateful for their support and enthusiasm in everything that I have always done.

Table of Contents

1 Introduction **1**
- 1.1 Historical overview . . . 1
- 1.2 Conventional fluorescence microscopy . . . 3
- 1.3 Optical sectioning in microscopy . . . 6
  - 1.3.1 The confocal fluorescence microscope . . . 6
  - 1.3.2 The two photon fluorescence microscope . . . 8
- 1.4 Three dimensional imaging . . . 10
- 1.5 Scanning techniques . . . 13
  - 1.5.1 Object scanning in X, Y & Z . . . 14
  - 1.5.2 Beam scanning in X & Y, object scanning in Z . . . 15
  - 1.5.3 Parallel acquisition of data points . . . 16
  - 1.5.4 Beam scanning in Z . . . 20
- 1.6 Conclusions and overview of thesis . . . 22

2 Extended depth of field microscopy using annular illumination **24**
- 2.1 Introduction . . . 25
- 2.2 Theory and system design . . . 27
- 2.3 Point spread function measurements . . . 34
- 2.4 Imaging . . . 38
- 2.5 Stereo Imaging . . . 40
- 2.6 Conclusion . . . 41

3 Remote focusing in microscopy **43**
- 3.1 Introduction . . . 43
- 3.2 Imaging in three dimensions . . . 45
- 3.3 The general pupil funcion . . . 48
- 3.4 A technique for remote focusing . . . 51
- 3.5 Range of operation . . . 55
- 3.6 Conclusions . . . 59

4 Point spread function measurements **62**
- 4.1 Measuring the PSF . . . 62
- 4.2 Experimental results . . . 68
- 4.3 Conclusions . . . 71

5 Applications of remote focusing in sectioning microscopy 73
5.1 Practical implementation of remote focusing 73
5.2 Nipkow disc confocal microscope 77
5.2.1 Extended depth of field microscopy 81
5.2.2 Stereo imaging 84
5.3 Slit scanning microscopy 87
5.4 Structured illumination microscopy 89
5.5 Two-photon microscopy 95
5.6 Conclusions and discussion 97

6 Conclusions and discussion 100

Appendices 104

A Imaging theory and the point spread function 104
A.1 Kirchhoff-Fresnel scalar diffraction theory 104
A.2 The point spread function 106

B The generalized microscope 110
B.1 Fluorescence confocal imaging 112
B.2 Two-photon fluorescence imaging 113

C High NA scalar theory and spherical aberration 115

D High NA vectorial theory 119
D.1 The Debye theory 119
D.2 Vectorial Debye theory 121

Bibliography 124

Chapter 1

Introduction

1.1 Historical overview

Historically, the effects of optical magnification and focusing were known to ancient civilizations, who used vases and carafes of water to concentrate the rays of the sun to start fires and magnify small objects for examination. There is no sign, however, that lenses were used as optical instruments until the thirteenth century when Roger Bacon introduced for the first time what may be termed a magnifying glass. Further steps were taken by others and by the end of that century spectacles are reported to have been used in Italy.

In 1590, or shortly afterwards, Hans Jansen in the Netherlands was the first to report the construction of a compound system of lenses in a tube with an adjustable distance to enter his name in history as the probable inventor of the compound microscope as well as paving the way for the invention of the telescope, which is just a microscope used in reverse. Such was the significance of this discovery that when news of this invention reached Galileo Galilei in Italy at the beginning of the 17th century, he constructed his own system of lenses and promptly announced a multitude of scientific discoveries about the universe, reporting that the Moon had volcanoes and craters, the Sun had spots and that the Milky way in fact consisted

of a myriad of stars.

As for the compound microscope, further developments were carried out in Italy by Eustachio Divini which lead to the introduction of plano-convex lenses. These could be used in microscopes to reduce the effects of spherical aberration and hence improve the quality of observed images. At the same time Robert Hooke, in England, invented a machine that could grind lenses with any conceivable curvature and hence was able to construct precise optical elements. His craftsmanship extended beyond this and he produced, for the first time, a system with an adjustable stand, a moveable stage and equipment for effective illumination. In 1665, he published a work, *Micrographia* [1], which became epoch making in the history of the microscope, with thirty-eight outstanding illustrations of minute animals and vegetation that he observed with his optical instrument.

Meanwhile, in the Netherlands, Antony Leeuwenhoek, a talented self-taught amateur, developed lenses that could gain extraordinarily high optical magnifications so that the smallest details could be observed. Realizing that the magnification of a single lens could be increased by increasing the curvature of the surface, he developed small spherical lenses with radii as small as 0.75mm that could effect magnifications of up to 275X.

Over the next two centuries, improvements in lens design were introduced so as to further reduce the effects of aberrations and improve image quality. Although this was done with great precision, the lenses produced varied widely in terms of the resolution that could be achieved until 1873 when Ernst Abbe, while working with Carl Zeiss in Germany, published a number of experimental studies and a sensational theory of image formation in the microscope [2]. In this work, he set out the fundamental limitations on image resolution and explained that was intimately related to the numerical aperture of the lens, showing that higher resolutions could be achieved if the lens collected light emanating at higher angles from the specimen. This result can be expressed in terms of a simple equation that prescribes the

smallest distance between two points, d, that can be resolved:

$$d = \frac{\lambda}{2n \sin \alpha} = \frac{\lambda}{2NA} \tag{1.1}$$

where λ is the illumination wavelength, n is the refractive index of the immersion media and α the semi-angular aperture of the objective lens. The refractive index and angular dependence can also be recast as $NA = n \sin \alpha$, which is commonly referred to as the numerical aperture. So famous was this result that it is carved on Abbe's memorial in Jena. Over the next few decades, lens design became a refined art and objectives could be produced with almost no aberrations that operated close to the fundamental limit of resolution.

1.2 Conventional fluorescence microscopy

Further developments soon lead to a range of imaging techniques for interrogating the properties of common specimens, each employing slightly different contrast mechanisms. One such technique, that proved to be particularly useful in the biological sciences, was that of *fluorescence microscopy*. A schematic diagram of such a conventional microscope system, in its modern manifestation, is shown in Fig. 1.1. In operation, light from an arc lamp source is focused by the objective lens into the specimen, where it excites fluorophores that either may be a natural part of the specimen or deliberately introduced as a contrast agent. The fluorescent emission is then collected by the same objective lens and passes through a dichroic beam splitter (DBS) that separates the emission light from the excitation light. The emission light is imaged with a CCD camera, placed in the image plane of the microscope, which is conjugate to the focal plane of the objective lens (shown as a dashed line). This then records a two dimensional image of the specimen.

An example image of a random array of fluorescent polymer beads with a di-

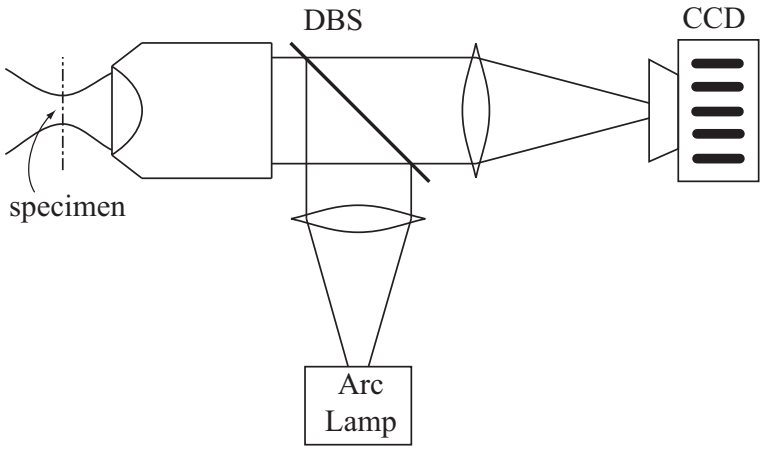

Figure 1.1: *A conventional fluorescence microscope in its modern manifestation.*

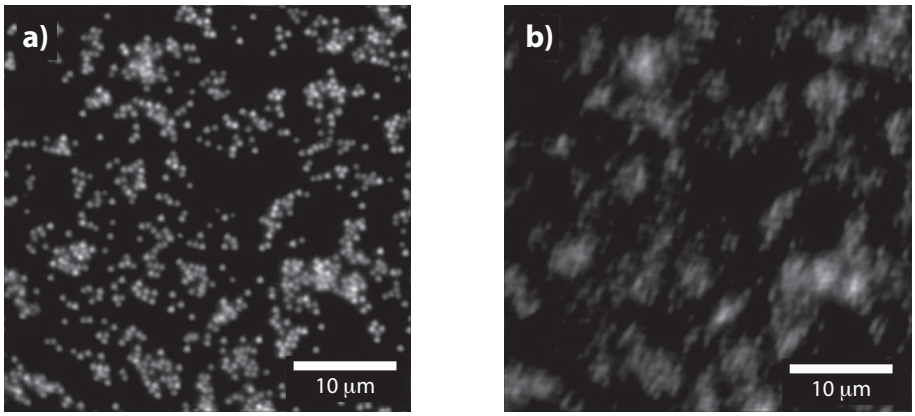

Figure 1.2: *A conventional fluorescence image of a random array of fluorescent polymer beads lying in a single plane a) in focus and b) displaced axially from focus.*

ameter of $0.5\mu m$ is shown in Fig. 1.2a. The beads are dried onto a coverglass and essentially lie in the focal plane of the objective lens. This image was acquired using a 1.4NA 63X oil immersion objective lens and an excitation filter was used to provide an illumination spectrum in the range 432-482nm. Eq. 1.1 predicts that details as small as $0.25\mu m$ should be observable and this is borne out in practice as each of the constituent beads can be individually resolved, even when in contact with others. In Fig. 1.2b, an image of the same specimen is shown for the case where it is displaced along the optical axis by a few microns. As the specimen remains in the illumination path of the microscope, fluorescent emissions are still initiated across

the whole field of view. The process of moving the specimen, however, has taken it out-of-focus and so the resulting image on the CCD camera is somewhat blurred. As we can see, clear, high-resolution images only arise when the specimen lies in the focal plane of the microscope.

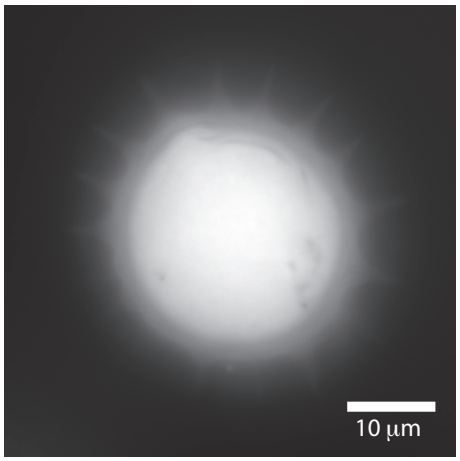

Figure 1.3: *A conventional fluorescence image of a pollen grain*

This specimen is, of course, rather artificial as it is essentially a two dimensional object. In practice, specimens are usually three dimensional and extend along the optical axis of the microscope as well. Fig. 1.3 shows the image of a three dimensional fluorescent pollen grain obtained with the same microscope. In this case, the entire specimen lies in the illumination path and so the resulting image consists of a clear contribution from the parts of the specimen that lie in the focal plane of the microscope on top of which is superposed the blurred signal that arises from all parts of the pollen grain that lie out-of-focus. The blurred contributions therefore introduce a background noise that essentially obscures the details in focus.

One brute force approach that can be used to remove this background noise to obtain high quality images of single planes in the specimen would be to physically cut the three dimensional object into a series of two dimensional slices and to image each of these in turn. This *sectioning* process is not always possible, however, and is highly invasive to the specimen. Fortunately, more sophisticated *optical sectioning*

approaches exist that remove the out-of-focus contributions using optical techniques without altering the specimen physically. This is discussed in the following section.

1.3 Optical sectioning in microscopy

An important breakthrough in the mid-fifties lead to the concept of the *optical sectioning* in microscopy. This permitted the out-of-focus blur in conventional images to be eliminated in order to obtain a clean in-focus image of a single specimen plane ([3], [4]). Various techniques can be used to achieve this and in the next two sections we will discuss the underlying principles of two such techniques that have made considerable impact in the field of biological imaging, namely the confocal microscope and the two photon microscope.

1.3.1 The confocal fluorescence microscope

Historically, Minsky [5] and Petráň et al. [6] were the first to describe systems exhibiting the standard properties of a confocal microscope. However, it was not until 1978, after the development of the coherent laser source, that the first practical demonstration of a high resolution system was performed by Brakenhoff et al. [7, 8]. A simplified schematic of the confocal microscope is shown in Fig. 1.4 and illustrates the basic principle of operation.

In summary, light from a laser passes through a source pinhole and is focused by an objective lens into the specimen, where it excites fluorophores. In contrast to the conventional microscope, which uses an extended light source, the laser illumination in this case produces a diffraction-limited spot in the focal plane of the objective lens. Fluorescent emission, which is initiated throughout the illumination cone, is then collected by the same objective lens and passes through a dichroic beam splitter in the same way as before. The emission light is now focused onto a detection pinhole placed in front of a photodetector (PD). This pinhole, which is in

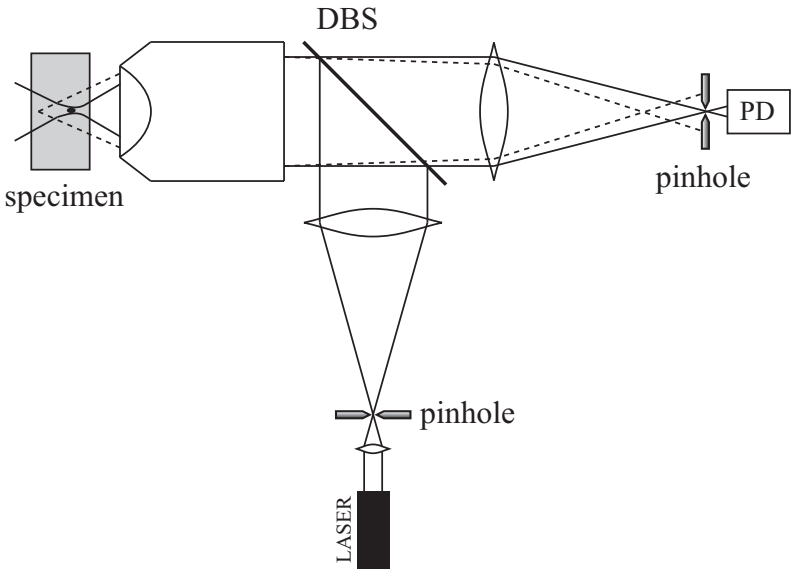

Figure 1.4: *A confocal fluorescence microscope.*

the same position optically as the source pinhole, obscures fluorescent light emitted by fluorophores lying outside the focal plane and only admits light emanating from the focal region. As a result, this system measures the fluorescence intensity arising from a diffraction-limited spot in the specimen. An image can be constructed, with the aid of a computer, by scanning the interrogation point relative to the specimen across the focal plane to measure the fluorescence strength at different positions in a two dimensional array of points. An image can then be displayed afterwards on a computer. There are a number of methods that can be used to perform the scanning and these will be discussed shortly.

An example image taken with a confocal microscope is shown in Fig. 1.5. This is the same pollen grain specimen used previously. Comparison of this image and the conventional image in Fig. 1.3 shows the significant improvement that clearly arises from the elimination of contributions from out-of-focus regions of the specimen.

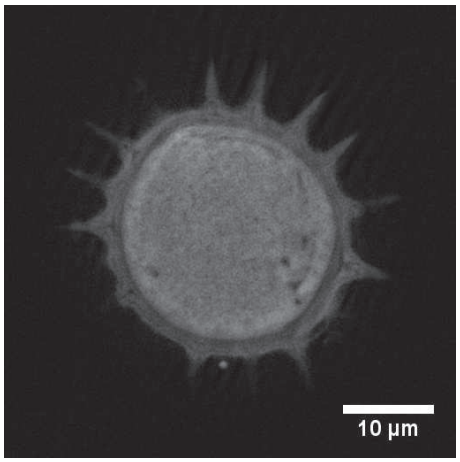

Figure 1.5: *A confocal fluorescence image of a pollen grain.*

1.3.2 The two photon fluorescence microscope

The two photon fluorescence microscope was first demonstrated experimentally by Denk et al. [9] in 1990. This technique essentially relies on the non-linear nature of the two-photon absorption process that is initiated in fluorophores lying in the most intense regions of the focal spot in the specimen.

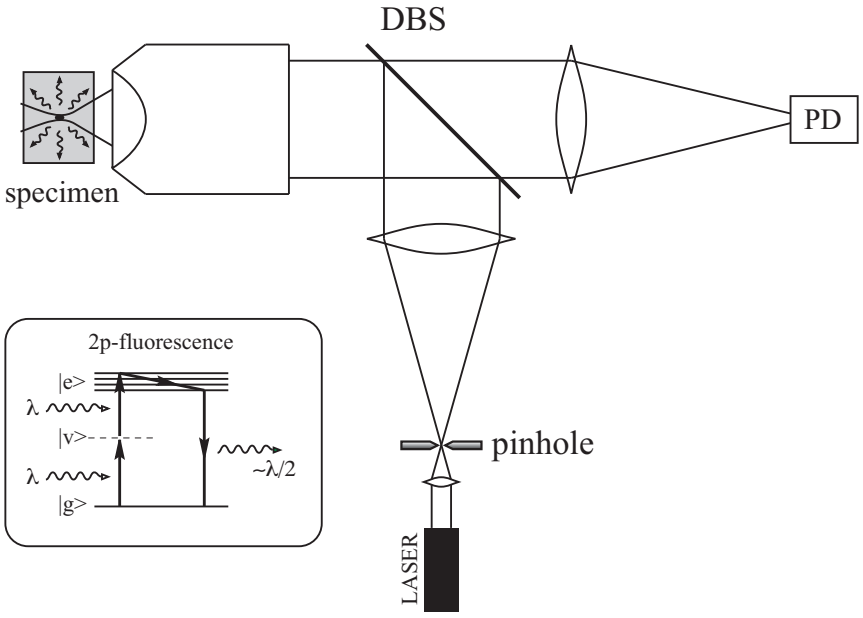

Figure 1.6: *A two photon excitation fluorescence microscope. (Inset: the energy level diagram of the fluorescent molecules.)*

Fig. 1.6 shows the basic setup for this microscope, which is similar to the confocal setup of the previous section. The inset shows how two photons can be used to promote a fluorescent molecule to an excited state via a virtual energy level whereupon it decays by emitting a single photon with approximately half the wavelength of the original photons. Quantum mechanical calculations show that the rate of this excitation process is proportional to the the square of the illumination intensity and so this effect becomes progressively more pronounced at higher intensities. As a result, only fluorophores in the most intense parts of the focal spot in the specimen are excited by this process. The emissions that result from this single point in the specimen are separated out with a dichroic beamsplitter and detected with a photodetector. Images are obtained, in the same way as for the confocal microscope, by scanning the focal spot laterally in the specimen and recording fluorescence intensities at different points in a two dimensional array. As fluorescence emission is not generated in the rest of the illumination cone, the detection pinhole is no longer needed in front of the photodetector to obtain optical sectioning.

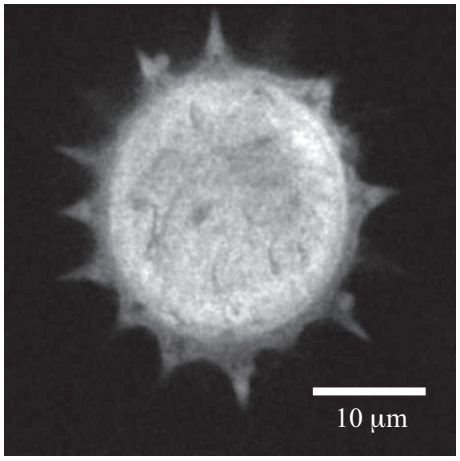

Figure 1.7: *A two photon fluorescence image of a pollen grain.*

An example image taken with a two photon microscope is shown in Fig. 1.7. A similar pollen grain specimen has been used and once again it can be seen that a good quality image of a single specimen plane has been obtained.

1.4 Three dimensional imaging

As has been seen in the previous section, optical sectioning eliminates out-of-focus blur and gives rise to a clean in-focus image of the specimen in the focal plane of the microscope. The real advantage of such techniques, however, lies in the fact that they can be used to gather *three dimensional* information about specimen structure by simply refocusing the microscope and recording a series of images from different specimen planes. Computer algorithms can then be used to display the resulting data set in a number of different formats.

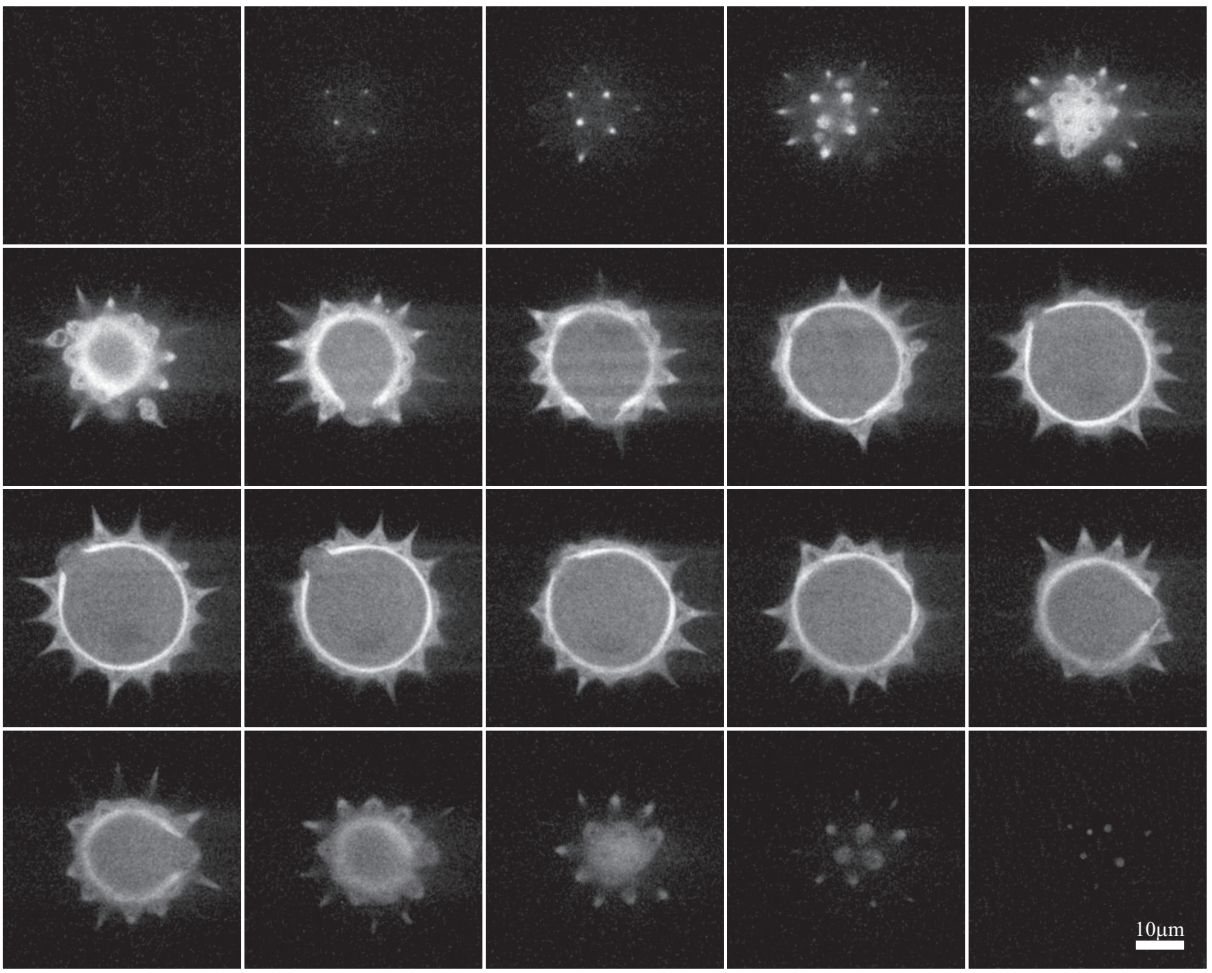

Figure 1.8: *A confocal fluorescence image stack of a single pollen grain. Courtesy of Dr. R. Juškaitis*

A subset of images from a typical confocal image stack is shown in Fig. 1.8,

where successive images have been acquired from planes separated by $0.7\mu m$ in the specimen. These were obtained and generously donated by Dr. R. Juškaitis. A particularly simple procedure that can be used to display this data is to sum the corresponding pixel values of each image together in order to obtain an *extended depth of field image*. This is equivalent to projecting the image data along the optic axis of the microscope onto a single lateral plane. The result of applying this procedure to the first half of the image stack here is shown in Fig. 1.9, which I did myself using the *ImageJ* software from the National Institue of Health website in the USA. As can be seen, information from a whole range of specimen depths is displayed simultaneously in a single image and appears to be viewed along the optic axis, which is along the direction that the data was projected.

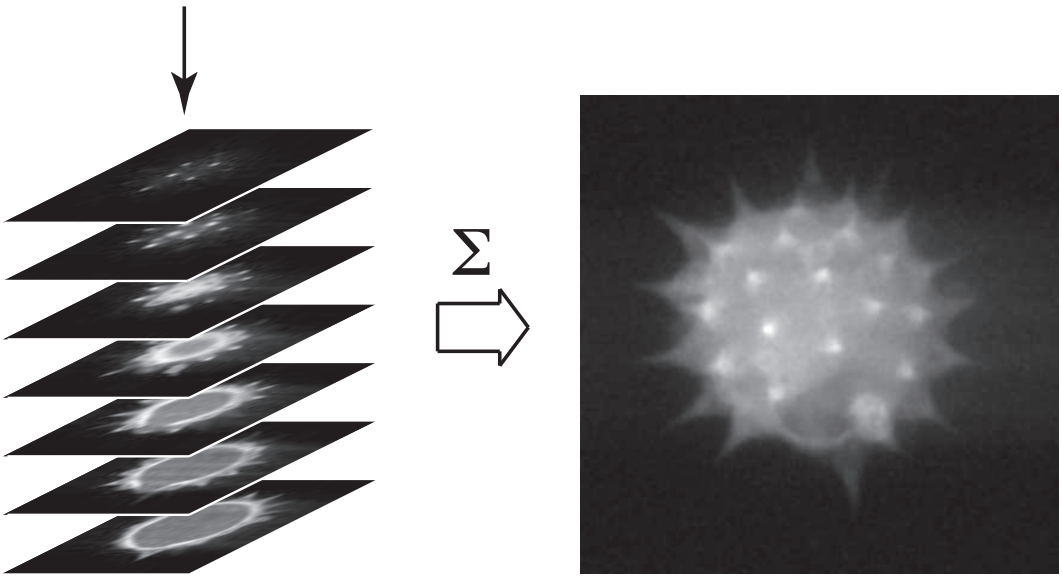

Figure 1.9: *Constructing an extended depth of field image.*

It is also possible to project the image stack along different directions to obtain extended depth of field images from different perspectives. Two such projections along axes separated by 12°, can be taken to obtain a *stereo pair* of images. This is shown in Fig. 1.10 and can be used to gain an impression of the specimen as if it were a macroscopic, three dimensional object. In nature, observers gain an

impression of the three dimensional structure of objects as a result of the lateral separation between their eyes. Each eye views the same object from a slightly different perspective and the brain can process this information to calculate the relative distance of different points in the image, leading to a perception of depth. By arranging for each eye to view a different image in the stereo pair, the observer can be given a sense of the three dimensional structure of the specimen. In this case the stereo effect can be viewed directly by focusing each eye onto a different image. There are, however, more comfortable ways to present such images, for example using a stereo monitor which overlays the constituent images on the same screen and separates them in angle so that each eye can only see the image relevant to itself.

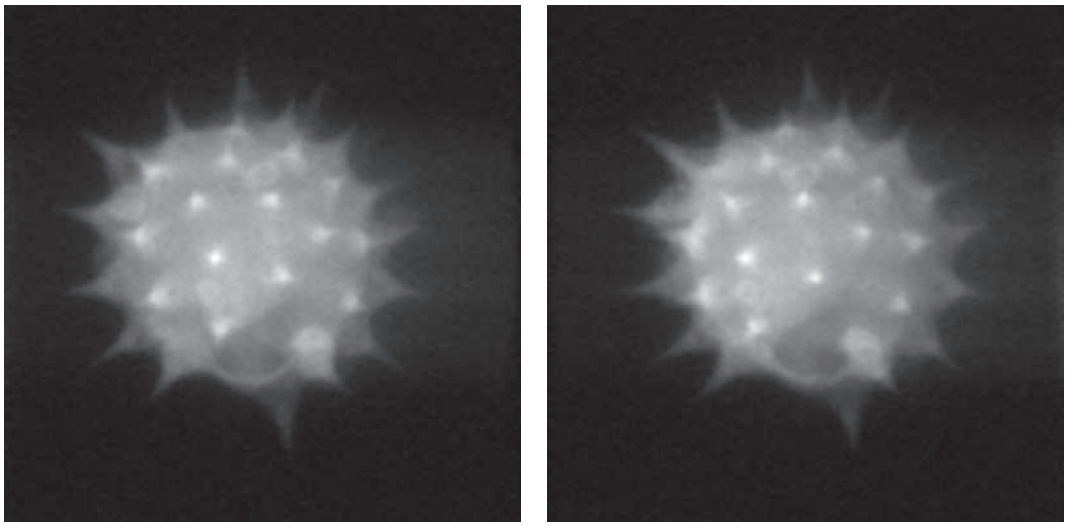

Figure 1.10: *A stereo pair of images*

More sophisticated computer rendering algorithms have also been developed to display the three dimensional information acquired in sectioning microscopy. A striking example of an image that has been generated using such an algorithm is shown in Fig. 1.11. In this reconstruction, performed by the software package *LSM 5 Image Examiner* (Zeiss, Germany), voxels with a given signal value have been linked to obtain an opaque surface so as to better display the object structure.

Shadowing effects have also been introduced to produce an aesthetically pleasing result. This process can also be repeated for a number of different perspectives and movies constructed that give the impression that the user is panning around the specimen as if observing a macroscopic object.

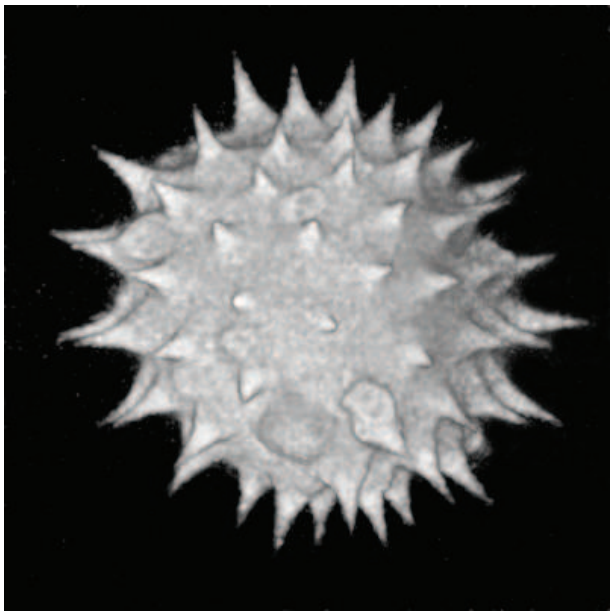

Figure 1.11: *Three dimensional rendering of a typical image stack.*

The ability to gather and process three dimensional information about specimen structure has made the techniques of sectioning microscopy an indispensable tool in many fields of the biological sciences as well as for optical metrology. The possibility to extract data from these three dimensional images stacks is of course not limited to the cases that have been shown here and further algorithms have also been developed for specific situations.

1.5 Scanning techniques

Initially, systems built to acquire three dimensional image stacks of biological specimens were used on fixed samples which remained stationary during imaging. In time, it became of interest to apply these techniques to acquire *in vivo* data from

live specimens in their natural environment. As a result, it was necessary to develop systems with high temporal resolution so that multiple image stacks could be acquired to monitor the dynamical behaviour of these specimens in three dimensions.

As has been seen, both the confocal and two photon microscopes analyse a single point in the specimen at any one time. Acquisition of a three dimensional image stack then follows by scanning this point of interrogation to measure the response of the specimen at different points in a three dimensional array. The temporal resolution of these systems is therefore intimately related to the speed at which this scanning can be carried out.

In the following sections a synopsis is given of the various scanning methods that are commonly used in sectioning microscopy and it is shown why, with the current microscope architecture, the real bottleneck in high speed three dimensional imaging is in fact imposed by the process of refocusing these systems to image different specimen planes.

1.5.1 Object scanning in X, Y & Z

Conceptually, the most straight-forward method for acquiring a three dimensional image stack using a confocal or two photon microscope is to physically translate the specimen so that different points in a three dimensional array are imaged in turn. Specifically, this can be done by translating the specimen laterally, in the XY plane using a raster scan, and then repeating this procedure at different axial positions along Z.

This is simple enough to do using piezo-electric actuators but the speed at which the specimen can be moved is severely limited by its mass. Indeed, for some situations this method may require that the specimen be excised from its host in order that it may be imaged, which could affect its behaviour considerably. Even so, the maximum achievable acquisition speeds of a single specimen plane is still limited to

about thirty seconds for an image with 512×512 pixels.

Another problem with this approach is that the process of moving the specimen may introduce agitation, which may also affect the way in which it behaves while being imaged.

1.5.2 Beam scanning in X & Y, object scanning in Z

As a result of the severe limitations imposed on image acquisition speed by moving the specimen physically, commercial microscope systems often use a more sophisticated *beam scanning* approach to scan in the X and Y directions. In practice, this can be done by using the system shown schematically in Fig. 1.12, which is a slight variant on the confocal microscope shown previously. In this case, the same pinhole is used for illumination and detection. The DBS is placed behind the pinhole and the photodetector measures the signal in the same way as before from a single point in the specimen. Beam scanning can be performed in a number of ways and a popular choice, often adopted in commercial systems, is to use a pair of galvanometer mirrors, mounted at right angles to each other to tip or tilt the incoming and outgoing wavefronts. As can be seen, a further 4f system of lenses maps the plane in which the galvanometers lie into the pupil plane of the objective lens so that by tilting the mirrors the point of interrogation can be scanned laterally in the specimen. It is noted that this simple procedure is optically equivalent to displacing the pinhole laterally, along with all the elements behind it. Using galvanometer mirrors enables scanning to be carried out at far superior speeds compared with the method of object scanning.

With currently available technology, it is possible to perform a raster scan to image a single plane of the specimen at several frames per second. Such methodology can also be used to scan the focal spot in a two photon microscope.

To acquire a three dimensional image stack, however, it is still necessary to

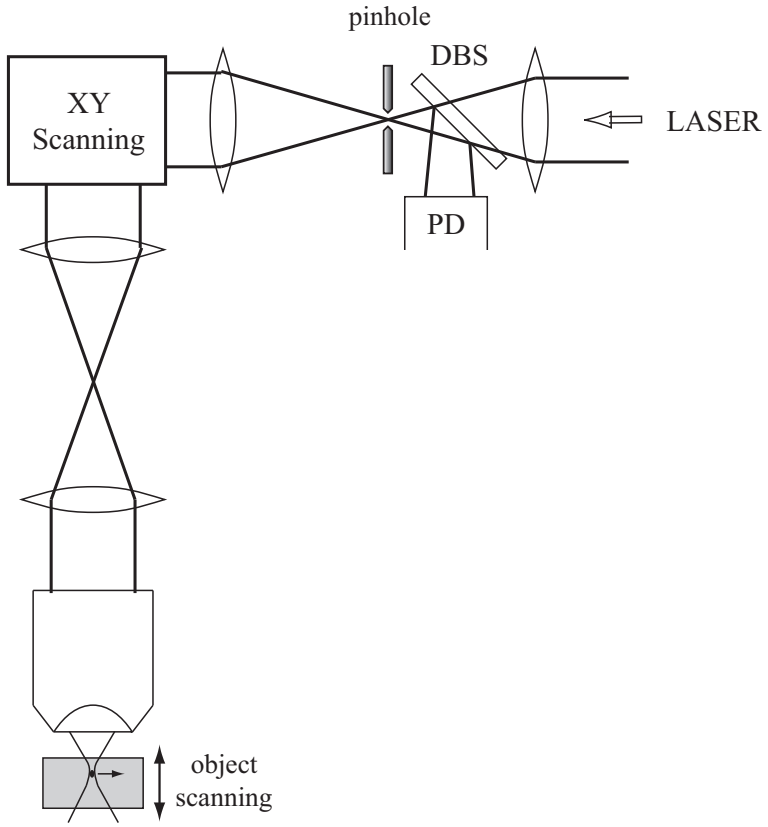

Figure 1.12: *Beam scanning using galvanometer mirrors.*

physically change the distance between the specimen and objective lens in order to image deeper planes of the specimen. As a result, refocusing speeds are still limited by the actuators used and specimen agitation along the axial direction may still be an issue in certain situations.

1.5.3 Parallel acquisition of data points

One of the main limitations in three dimensional image acquisition is the serial nature by which the data is acquired. This is because the systems presented so far only measure information from a single point in the specimen at any one time and so the three dimensional image stack must be constructed serially by measuring each point in turn. Various methods have been suggested, however, to improve acquisition speeds by essentially imaging multiple points in the specimen in parallel. Two

systems that have adopted this principle are the Nipkow disc confocal microscope and the slit scanning microscope, which are described in the following sections.

The Nipkow disc

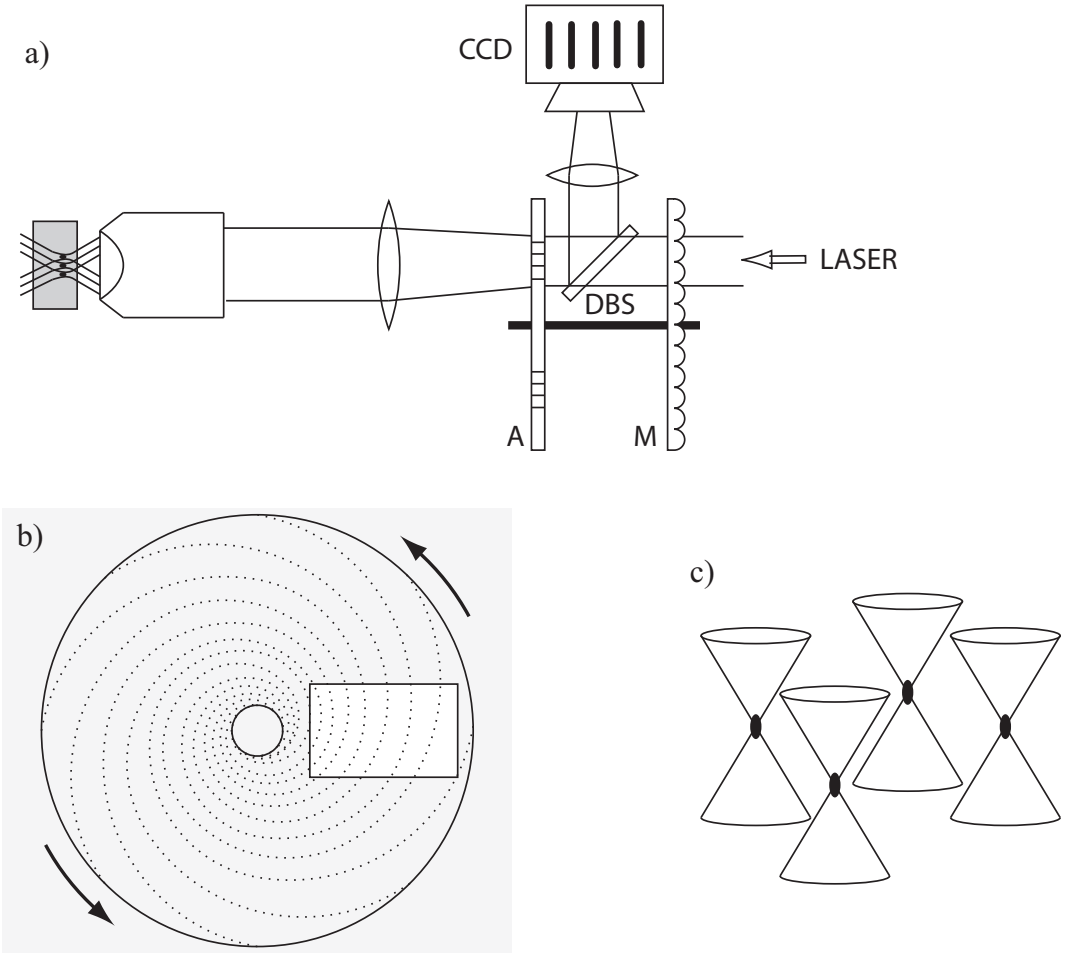

Figure 1.13: a) A Nipkow disc based scanning confocal microscope, b) the spiral array of pinholes on a Nipkow disc and c) the illumination pattern set up by four pinholes.

The Nipkow disc confocal microscope was originally proposed and demonstrated by Petran et al. [6]. Recently, various commercial systems have become available that are based on the Nipkow disc principle. An example of such a system is the CSU10 (Yokogawa, Japan), which is designed to plug into the camera port of a conventional microscope and produce confocal images directly on a CCD camera.

A schematic of this is shown in Fig. 1.13a. It is similar to the standard confocal microscope except that a pinhole array (A), etched onto a Nipkow disc, now replaces the single pinhole used previously. The Nipkow disc itself is shown in profile in Fig. 1.13b and it can be seen from this that the pinholes are arranged in a spiral fashion, circulating outwards from the centre. The rectangular area denotes the field of view. A carefully aligned array of microlenses (M) is also included in the CSU10 to focus laser light through each pinhole in the field of view so as to make most efficient use of the illumination power. The illumination light passing through the Nipkow disc is then focused into the specimen with the objective lens. Each pinhole sets up an independent focal spot at the apex of an illumination cone. The pattern produced by four such pinholes is shown in Fig. 1.13c. Fluorescence emission, which is initiated throughout the illuminated regions of the specimen, is then collected by the objective lens and focused back onto the Nipkow disc. In the same way as for the confocal microscope, each pinhole obscures fluorescence light emitted by fluorophores lying outside the focal plane and only admits light emanating from its conjugated focal spot.

The fluorescence signal passed by the different pinholes in the field of view is then re-imaged onto a CCD camera. In this way, different pixels measure the fluorescent response from different points in the specimen in parallel. It is worth mentioning that at any instant in time the majority of CCD pixels will not measure anything due to the sparsity of the pinhole arrangement. Scanning follows by spinning/rotating the Nipkow disc and array of microlenses on axis, which causes the pinholes to sweep across the field of view so that at one time or another all the parts of the specimen in the focal plane are imaged onto the CCD camera. Integrating the response on the camera gives rise to a confocal image of a single specimen plane. Acquisition of a three dimensional image stack then follows by physically moving the specimen, or equivalently the objective lens, along the axis in order to image different specimen planes.

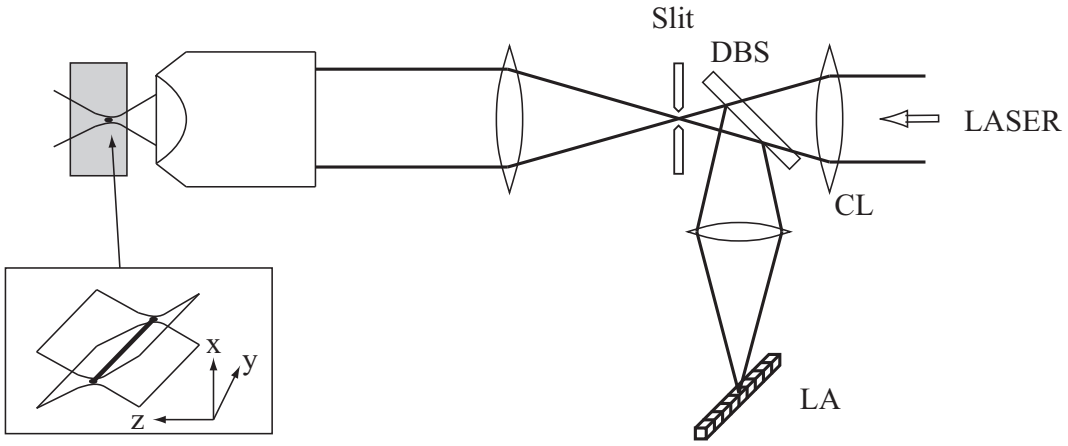

Figure 1.14: The slit scanning microscope

The slit scanning microscope

A further technique for acquiring image data from a number of different specimen points in parallel is that of *slit scanning microscopy*. This was first proposed and developed by Burns et al. [10] and Brakenhoff et al. [11]. The main difference between this technique and the standard confocal microscope is that a slit aperture is used in place of the pinhole. A schematic diagram of this system is shown in Fig. 1.14. Here, light from a laser is focused with a cylindrical lens (CL) onto the slit and the light that passes through is re-imaged into the specimen with an objective lens. As represented in the figure inset, the illumination pattern set up in this case is a highly focused line of laser light along the y-direction. Fluorescent emission, initiated throughout the illumination pattern, is then collected by the same objective lens and focused back onto the slit. The slit obscures fluorescent light emitted by fluorophores lying outside the focal plane and only admits light emanating from the in-focus line. The light passing through the slit is then separated out with a DBS and re-imaged onto a linear array of photodetectors (LA). In this way, the fluorescence intensity can be measured along a whole line of points in the specimen in parallel.

A two dimensional confocal image of the regions of the specimen lying in the focal

plane can then be constructed by placing a single galvanometer mirror in the pupil plane of the objective lens and scanning the illumination line along the x-direction and measuring the response of the linear array at different positions along the scan.

In summary, this technique of parallel data acquisition removes the requirement to scan along one of the lateral directions. As such, the speed of image acquisition from a single specimen plane can be improved dramatically and current commercial systems, such as the *LSM 5 LIVE* from Zeiss, are capable of achieving frame rates of 120 Hz. It is noted that there is a slight reduction in the axial resolution compared with the standard confocal microscope. Three dimensional image stacks can once again be acquired by physically changing the distance between the specimen and objective lens in order to image different planes in the specimen. This sets the bottleneck when acquiring three dimensional data stacks as the refocusing speed cannot compete with image acquisition in each lateral plane.

1.5.4 Beam scanning in Z

So far, we have seen that using the technique of object scanning to acquire three dimensional image stacks is a slow process due to the speed limitations imposed by the transducers used. It was then shown that a dramatic improvement in image acquisition speed can be obtained for a single specimen plane either by using a remote beam scanning approach or by measuring multiple data points in parallel.

In the case of beam scanning, improvements in lateral scan speed were achieved by using galvanometer mirrors to displace the lateral position of the focal spot in the specimen. It was noted that this procedure is optically equivalent to displacing the confocal pinhole laterally so as to interrogate these different points in the specimen. It might therefore be considered that improvements in the axial scan speed could also be achieved by introducing optical elements that displace the effective position of the pinhole along the axis instead so as to refocus the focal spot to different

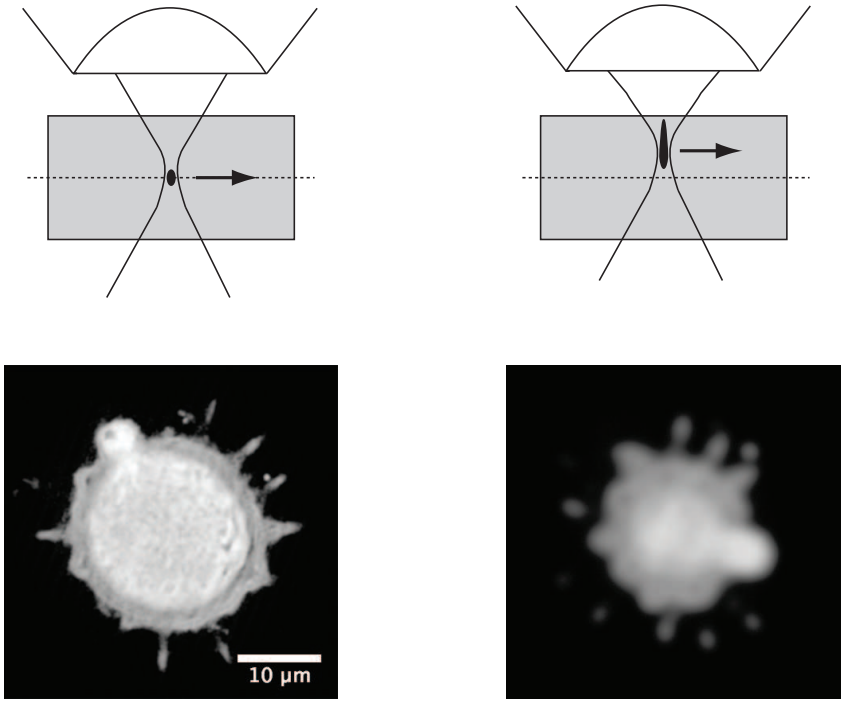

Figure 1.15: *a) A typical confocal image using beam scanning and b) The effect of displacing the confocal pinhole axially.*

depths in the specimen remotely. Unfortunately, there are fundamental reasons why this method of refocusing cannot be implemented successfully using this microscope architecture. An illustration of the problems that arise in such cases is shown in 1.15.

For the purposes of comparison, the first case in this figure shows the image obtained with a standard confocal microscope using beam scanning to acquire data from laterally displaced points in the focal place of the objective lens. The second case shows the image obtained if the confocal pinhole (not shown) is displaced along the optical axis of the system to refocus the focal spot to higher regions of the specimen. Here, beam scanning has also been used to displace the focal spot laterally in order to acquire the image. As can be seen, the process of displacing the pinhole along the axial direction has indeed refocused the focal spot to a higher region of the specimen but unfortunately this has been accompanied by a deformation

in its shape. This deformation, which can be attributed to systematic spherical aberrations introduced when refocusing this way, causes elongation along the axial direction as well as broadening in the lateral direction. The resulting image therefore contains data from a range of depths in the specimen as well as being slightly blurred in the lateral plane. The overall image intensity is also reduced due to the reduction in confinement of laser energy in the focal spot. We shall return to this point later on in this thesis.

A fundamental theorem put forward by Maxwell [12] shows that it is not possible to design a microscope system with magnification that allows the focal spot to be scanned in all three dimensions without introducing distortion along at least one of the axes. Commercial lenses are designed to permit lateral scanning and therefore introduce distortions for axial scanning. Consequently, the only way to scan along this direction, using the current microscope architecture is to either move the specimen or the objective lens.

1.6 Conclusions and overview of thesis

In this introduction we have seen how conventional fluorescence images of three dimensional specimens are intrinsically blurred out by fluorescence emitted by regions of the specimen that do not lie in the focal plane of the microscope. This problem can be circumvented, however, by using an optical sectioning technique, such as confocal fluorescence microscopy or two photon fluorescence microscopy, to remove the out-of-focus contributions and reveal a clean in-focus image of a single specimen plane. Although optical sectioning was the initial motivation behind the development of these systems later on, advances were driven by the need to increase their temporal resolution so that they could be used in time lapse studies to monitor the dynamic behaviour of specimens in three dimensions. Various methods have been developed in order to improve image acquisition speed and in most practical imple-

mentations, a single in-focus image can be acquired very quickly. However, the real bottleneck in three-dimensional imaging is the process of refocusing the microscope to successive image planes. This thesis concerns the acquisition of data from a range of specimen depths without requiring the specimen to be moved.

In Chapter 2, a modification is proposed and demonstrated for two photon microscopy that enables data from a whole range of specimen depths to be acquired simultaneously. A single two dimensional scan can then be used to acquire an extended depth of field image. This circumvents the need to acquire a full three dimensional image stack from which such an image must be calculated and hence dramatically reduces the time needed to acquire such images.

In the remainder of this thesis, a new microscope architecture is presented that overcomes the problems of spherical aberration while scanning along the axial direction remotely. As a result, this extremely general approach prescribes a method for designing a microscope system, based on *any* imaging technique, that can obtain aberration free images from different specimen depths remotely. Furthermore, this approach permits a vast improvement in axial scan speeds that can be acquired by up to two orders of magnitude. In Chapter 3, this new architecture is described and a theoretical analysis is carried out. In Chapter 4, experimental point spread function measurements are presented which demonstrate the range of axial depths that can be accessed using this technique. Finally, in Chapter 5, a number of different imaging systems are constructed based on the new architecture to demonstrate the applicability of this technique to a range of sectioning methods.

Chapter 2

Extended depth of field microscopy using annular illumination

As we have seen in the introduction chapter, extended depth of field images (Pg. 11) yield useful information about the structure of biological specimens. Using a two photon microscope, the only way to obtain such an image, up until now, would have been to acquire a full three dimensional image stack of the specimen and to process this computationally. We have already noted that the process of acquiring a three dimensional image stack requires a series of two dimensional images to be obtained from different planes in the specimen and that the process of refocusing fundamentally limits the speed at which extended depth of field images can be acquired. In this chapter we describe a novel method of acquiring extended depth of field images for two photon microscopy in a single image scan. This obviates the need to refocus the microscope and a considerable improvement in acquisition speed can be achieved. A description of this novel approach is given and a theoretical analysis is carried out. Experimental point spread function measurements are shown as well as some example images from this system. The combination of two extended depth

of field images, obtained at different parallaxes, is also shown. This allowed the generation of high resolution two photon stereo image pairs.

2.1 Introduction

One of the most important factors in determining the imaging properties of an optical microscope is the form of the focused spot of light that probes the specimen (see Appendices A and B). For instance, we have already seen in the introduction chapter how spherical aberration deforms the spot detrimentally and degrades image quality.

Mathematically, the amplitude of the focal spot is described by a three dimensional distribution commonly referred to as the *point spread function* (PSF). The ability to tune the form of this PSF by the careful control of the optical field incident on the objective lens pupil has lead to the field of point spread function engineering which has resulted in systems being constructed with a wide range of different imaging properties. Specific applications involve attempts at super-resolution [13, 14, 15], adaptive optics [16], the control of polarization of the focal spot [17, 18, 19], and the whole field of Meso-Optics (see e.g.[20]).

A particularly simple and intriguing application is to produce an axially extended PSF without sacrificing lateral resolution. It has long been known that by illuminating the back aperture of an objective lens with a ring of light, a PSF of considerable axial extension would result [21, 22, 23]. This effect is shown in Fig. 2.1, where for the purposes of comparison, the PSF produced with plane wave illumination is also shown. Scanning the elongated PSF in the lateral direction to acquire a two dimensional image results in data being recorded from a whole range of specimen depths simultaneously and leads to the direct acquisition of an extended depth of field image.

There are a number of ways to produce annular illumination. The simplest is

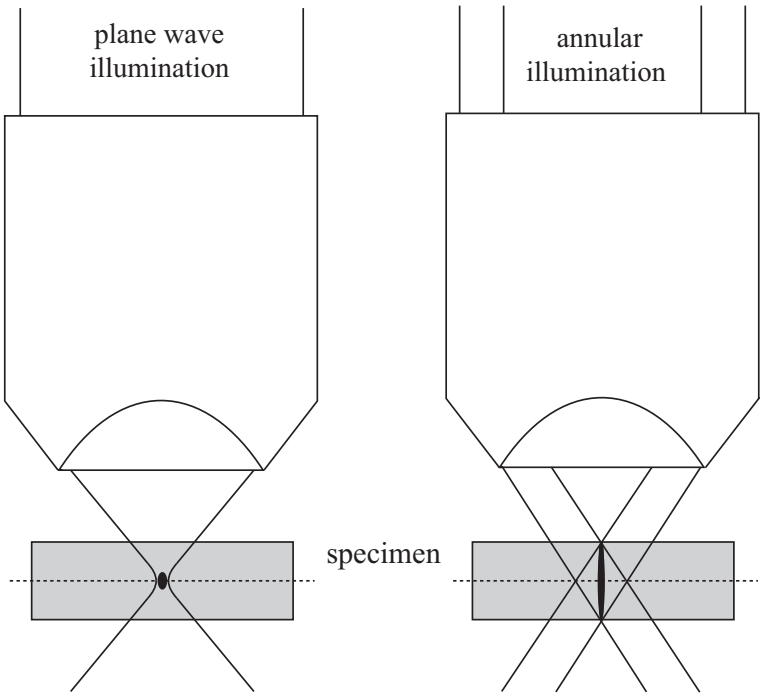

Figure 2.1: *The focal spot for a) plane wave illumination and b) annular illumination.*

to insert a physical annular mask into the pupil plane of the objective lens so as to permit only a ring of light to be transmitted. This may be thought undesirable since most of the incident energy is blocked leading to a very poor use of the available light. An alternative approach uses a conical lens or axicon [20, 24]. Although this is a light efficient method to produce ring illumination it does, as we shall see later, have some drawbacks for microscopy applications. In the following, therefore, we shall discuss the design of a circularly symmetric binary phase-only grating and show that this may be used to produce ring illumination with high light efficiency in a manner suitable for use in microscopy.

As an application we shall concentrate on scanning two photon fluorescence microscopy [9]. We choose this imaging mode since it possesses an inherent optical sectioning effect due to the non-linear fashion in which the fluorescence is generated. This in turn implies that it is not possible to image a whole volume specimen without stitching together a whole through-focus series of images, unless a point spread

function of considerable axial extent is used. Further the non-linear nature of the excitation process requires that the available light be used in the most efficient way. We shall demonstrate that the light efficiency of our binary phase grating is such that we can generate two-photon extended depth of focus images with ease. We note that this would not be practical if a physical annular stop was used to produce the ring illumination. As we will see, our system design is such that we lose less than 25% of the overall laser power and are able to tune the shape of the PSF to be essentially flat over more than a 10μm range. A further advantage of our approach is that by carefully tuning the directions along which our extended depth of focus images are obtained it is possible to obtain high-resolution two-photon fluorescence stereo image pairs.

2.2 Theory and system design

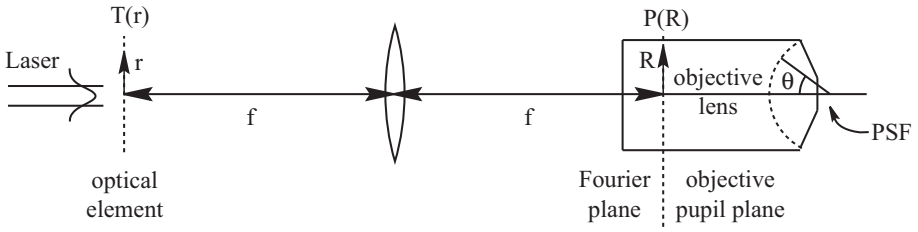

Figure 2.2: *Schematic diagram of the optical system.*

A schematic of the system that we will use is shown in Fig. 2.2. A Gaussian laser beam ($E \propto \exp(-r^2/w^2)$, where r is the radial coordinate and w is the width of the beam), illuminates an optical element with amplitude transmission function $T(r)$ placed in the back focal plane of a lens with focal length f. The Fourier transform of the amplitude which is transmitted, $T(r)exp(-r^2/w^2)$, appears in the Fourier plane of the lens. This field, $P(R)$, may be written, due to circular symmetry of our problem [25] as

$$P(R) = \int_0^\infty T(r) \exp\left(-r^2/w^2\right) J_0\left(\frac{2\pi r R}{\lambda f}\right) 2\pi r \mathrm{d}r, \tag{2.1}$$

where R represents the radial coordinate in the Fourier plane of the lens, J_0 is the zeroth order Bessel function of the first kind and λ is the wavelength. We position an objective lens such that its pupil plane is coincident with the Fourier plane of the first lens so that $P(R)$, Eq. 2.1, becomes the effective pupil function of the objective lens. In the low numerical aperture (NA) case the field in the focal region of the objective lens is given by the Fourier transform of the pupil function $P(R)$ however the situation is slightly more complicated for high NA objectives because substantial portions of the wavefront are refracted through large angles and the vectorial nature of light becomes important. Formal expressions for the field produced by a high NA objective lens have already been evaluated [26] and are derived in Appendix D. For the case where the illumination is uniform and linearly polarized in the x-direction, the field is given by

$$\mathbf{E}(r, \phi, z) = \frac{\pi i}{\lambda} \begin{pmatrix} I_0 + I_2 \cos 2\phi \\ I_2 \sin 2\phi \\ -2iI_1 \cos\phi \end{pmatrix}, \tag{2.2}$$

where the integrals I_0, I_1 and I_2 are defined in our case as

$$I_0 = \int_0^\alpha P(\theta) \cos^{1/2}\theta \, \sin\theta \, (1 + \cos\theta) \, J_0(kr \sin\theta) e^{-ikz\cos\theta} \mathrm{d}\theta, \tag{2.3}$$

$$I_1 = \int_0^\alpha P(\theta) \cos^{1/2}\theta \, \sin^2\theta \, J_1(kr \sin\theta) e^{-ikz\cos\theta} \mathrm{d}\theta, \tag{2.4}$$

$$I_2 = \int_0^\alpha P(\theta) \cos^{1/2}\theta \, \sin\theta \, (1 - \cos\theta) \, J_2(kr \sin\theta) e^{-ikz\cos\theta} \mathrm{d}\theta. \tag{2.5}$$

$J_1(.)$ and $J_2(.)$ represent first and second order Bessel functions of the first kind respectively, ϕ is the azimuthal angle and θ the zenith angle in the focal region. α is the maximum angle of convergence of the objective lens. $P(\theta)$ is the pupil function evaluated in Eq. 2.1 with the sine condition transformation $R = f_0 \sin\theta$ where f_0 is

the effective focal length of the objective lens.

We note that for the case where the pupil is apodized such that the pupil function may be described by an infinitely narrow annulus, $P(\theta) = \delta(\theta - \alpha)$, the field becomes a Bessel beam and the focal intensity is given by:

$$\begin{aligned} |E|^2 \propto [1+\cos\alpha]^2 J_0^2(kr\sin\alpha) + [1-\cos\alpha]^2 J_2^2(kr\sin\alpha) \\ +[2\sin^2\alpha J_0(kr\sin\alpha)J_2(kr\sin\alpha)\cos 2\phi] \\ +4J_1^2(kr\sin\alpha)\cos^2\phi, \end{aligned} \tag{2.6}$$

which does not vary with axial position z. Indeed in the low aperture limit we note that this expression results in the familiar $|E|^2 \propto J_0^2(kr\sin\alpha)$ Bessel beam. Although this situation cannot be realized practically, this example demonstrates that PSF elongation can be achieved as a direct result of annular illumination. We will now explore various methods for producing annular illumination in a light efficient manner. It will be shown that by far the most satisfactory of these methods is to use a binary phase grating. We began by considering an axicon which is a conical lens which introduces a phase variation that is a linear function of radial position. There are two varieties of axicon whose profiles are shown in Fig. 2.3, namely positive and negative ones. These elements can be described by the following transmission functions:

$$T_{pos}(r) = e^{i2\pi tr}, \tag{2.7}$$

$$T_{neg}(r) = e^{-i2\pi tr}, \tag{2.8}$$

where t is the parameter describing the slope of the axicon.

If we use such axicons as the optical elements in the system of Fig. 2.2 then the effective pupil function $P(R)$ is annular in form and the resulting intensity along the optical axis ($r = 0$) in the focal region of the objective is given by $|E|^2 \propto |I_0|^2$. Plots of these results are shown graphically in Fig. 2.3. We note that both the positive

and negative axicons produce essentially ring illumination which gives rise to the desired axial elongation. However, since the effective pupil functions are complex - the phase varies roughly linearly over the region where the intensity is significant – the distribution is asymmetric about the focal plane.

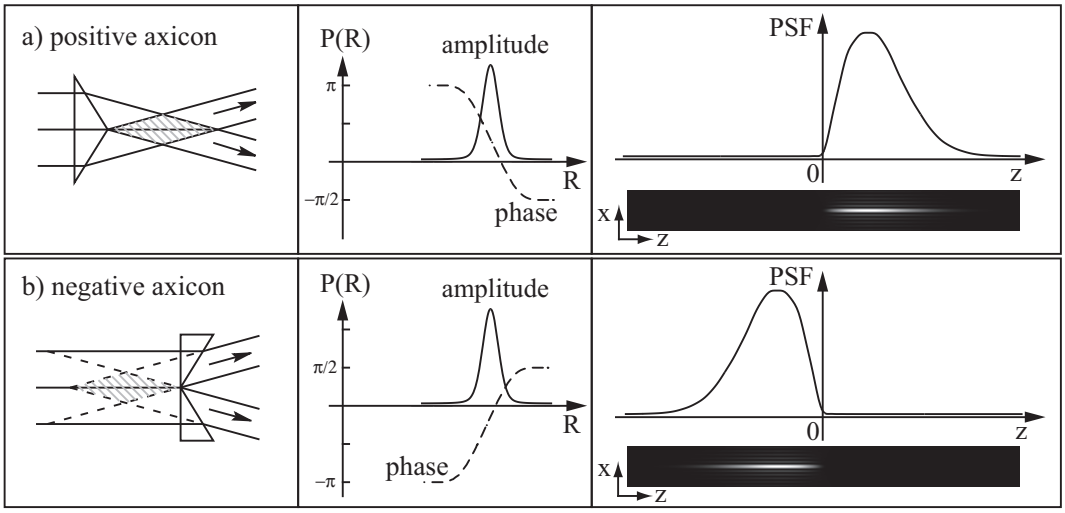

Figure 2.3: *The pupil function and corresponding intensity profile of the PSF generated by a) a positive axicon and b) a negative axicon. Parameters - $w = 0.5mm$, $t = 25mm^{-1}$, $\lambda = 750nm$, $f = 106.66mm$, $NA = 1.4$ oil immersion.*

The asymmetry, with respect to the focal plane ($z = 0$), of both these PSFs suggests that we might be able to produce an even larger axial extension if we use an optical element possessing a phase variation equivalent to the superposition of both a positive and a negative axicon. However, since the pupil function phase produced by each individual axicon is equal and opposite in magnitude, it is important to be able to control the relative phase between these elements so that their PSFs combine constructively in the focal plane of the objective lens. One method by which the transmission functions of Eqs. 2.7 and 2.8 can be combined and the relative phase between their contributions controlled is to use a binary, phase only, mask whose transmission function is shown in Fig. 2.4. Mathematically this can be expressed

using a Fourier series:

$$\begin{aligned} T(r) &= \frac{4}{\pi}\sum_{N=0}^{\infty}\frac{(-1)^N}{2N+1}cos[(2N+1)(2\pi tr-\beta)] \\ &= \frac{4}{\pi}\left\{cos[2\pi tr-\beta]-\frac{1}{3}cos[3(2\pi tr-\beta)]+\frac{1}{5}cos[5(2\pi tr-\beta)]...\right\} \quad (2.9) \end{aligned}$$

where β is an arbitrary phase offset. The important point to notice is that the average of this function $T(r)$ is zero and hence there is no zero spatial frequency term in the Fourier expansion. Physically this means that no light is directed to the zeroth diffraction order and it is this which accounts for the high throughput efficiency of our approach.

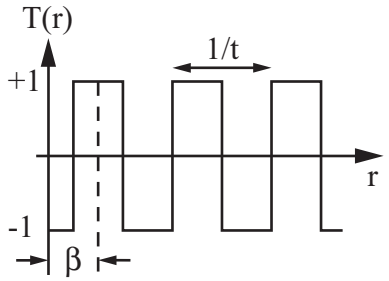

Figure 2.4: *The phase grating transmission function given in Eq. 2.9*

It is apparent that by setting $\beta = 0$ the first term in Eq. 2.9 becomes $\cos[2\pi tr] = \frac{1}{2}[e^{i2\pi tr} + e^{-i2\pi tr}]$ which is equivalent to the superposition of a positive and negative axicon. This leads to an annular ring whose amplitude is purely real and hence the resulting PSF, which is the superposition of the individual axicon PSFs, becomes symmetric about the focal plane. Higher diffraction orders do not contribute due to the limited aperture of the objective lens. Fortunately these contain far less energy than the first order as they are represented by less dominant terms in the series. The overall throughput efficiency of light into the first order is calculated numerically to be 81.0%.

The effect of choosing a non-zero value of β superposes the two axicons with

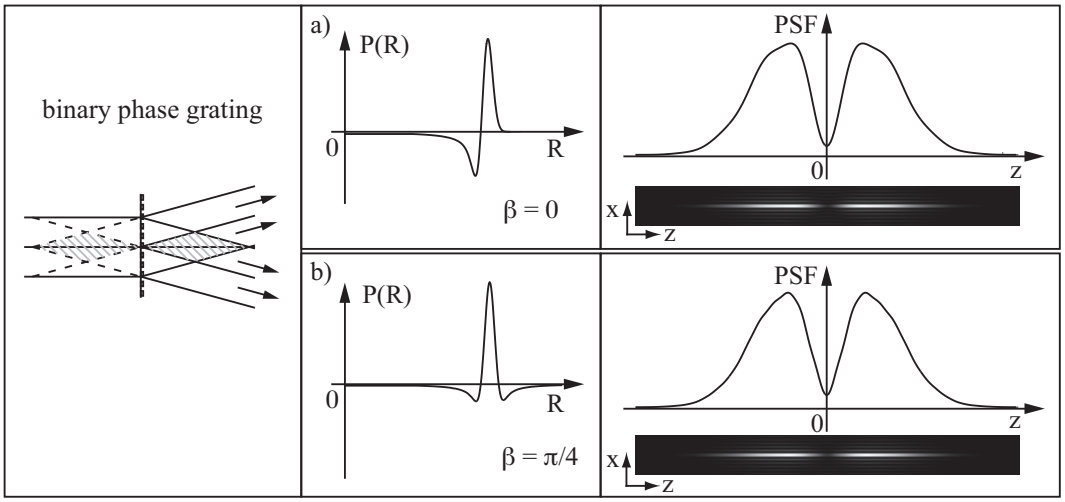

Figure 2.5: *The pupil function and corresponding intensity profile of the PSF generated by the binary phase grating defined in Eq. 2.9 with a) $\beta = 0$ and b) $\beta = \pi/4$. (Note that the phase variations from each axicon cancel out in the pupil plane to produce a pupil function that is entirely real.)*

relative phase shift 2β. This is illustrated in Fig. 2.5 for the cases where $\beta = 0$ and $\beta = \pi/4$. In both cases we observe an undesired dip in PSF intensity at the focal plane. The origin of this dip may be understood from the detailed form of the annular illumination presented to the pupil of the objective lens. This effective pupil function is shown in Fig. 2.5 where it is seen that over a significant region the pupil function is negative. The effect of choosing $\beta = \pi/4$, for instance, is to produce the desired sharp ring illumination together with two, (undesired) negative lobes on each side. These negative lobes are in fact the cause of the undesired dip in intensity in the focal plane and may be removed by introduction of an apodization mask. Fig. 2.6 shows the pupil plane field for the case of $\beta = \pi/4$ and the effect of inserting an apodization mask of width $2d$ on the axial intensity profile as a function of d. This plot was calculated numerically by inserting the phase grating transmission function of Eq. 2.9 into Eqs. 2.1 - 2.5. To account for the effect of the apodization mask, integrals Eq. 2.3 -2.5 where taken between angular limits corresponding to the edges of the mask. From this plot we can see that reducing the value of d reduces the central dip in the distribution at the cost of overall PSF

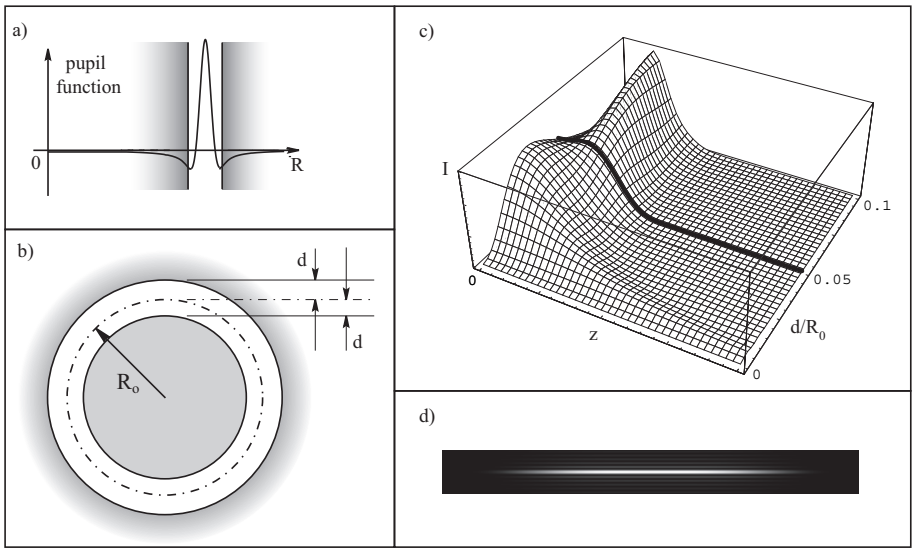

Figure 2.6: *a) An illustration of how the apodization mask truncates the field in the pupil plane when $\beta = \pi/4$. b) A further 2D illustration of the same apodization mask and definition of the parameters d and R_0 c) The axial intensity profile of the PSF generated as a function of d/R_0 with the optimally flat PSF marked, d) the XZ intensity profile of the PSF for this optimal case. (N.B. $R_0 = t\lambda f$ gives the approximate position of the peak of the ring.)*

length. The specific case where the ripple is reduced to zero ($\mathrm{d}^2I/\mathrm{d}z^2(0) = 0$) is highlighted on the graph. A further plot of the PSF in the xz plane is shown in Fig. 2.6d for this optimum case. In practice a larger value than the optimum was selected for d as it was considered to be of more practical interest to extend the PSF than to reduce the ripple completely.

Finally we mention the fact that apodizing the pupil function unavoidably blocks some of the incident light energy and therefore reduces throughput efficiency. A new calculation however reveals that 77.3% still enters the final PSF from the incident laser beam. This high efficiency is extremely important when operating in the two photon fluorescence regime.

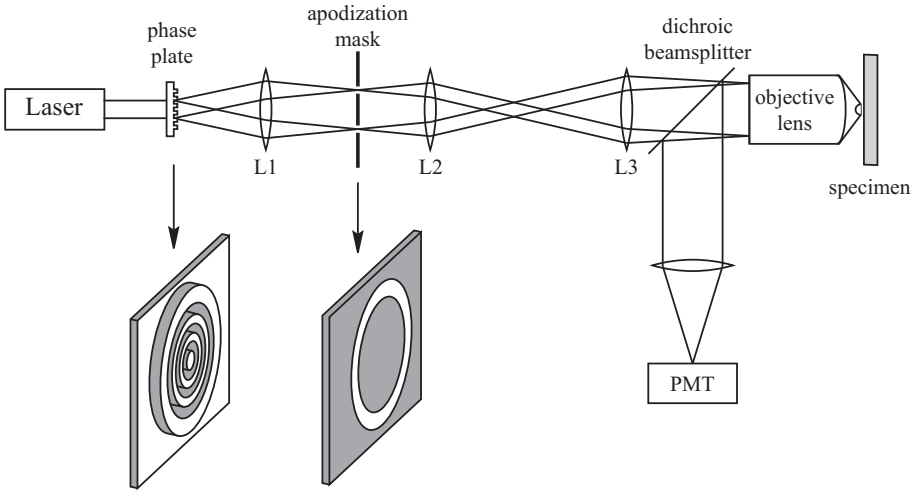

Figure 2.7: *Schematic diagram of the experimental arrangement*

2.3 Point spread function measurements

Fig. 2.7 shows a schematic of the system used. In all experiments we employed a Ti:Sapphire laser (*Tsunami*, Spectra Physics) with a maximum available power of 630mW, tuned to wavelength 750nm. For two photon imaging, the laser was operated in a mode-locked regime, which produced pulses of length $\sim$ 100fs at a repetition rate of 80MHz. The power could be adjusted externally with a neutral density filter set. A telescope arrangement (not shown) was also used to adjust the beam width illuminating the phase grating. This was necessary in order to match the diffraction pattern produced by the grating to the (fixed) width of the apodization mask.

The binary phase plate was produced by a two step process. First a chromium-on-glass photolithographic mask consisting of a set of concentric rings having equal mark-to-space ratio with spatial frequency of $t = 25mm^{-1}$ was made using commercially available mask fabrication techniques (JD Phototools, Manchester, UK). This mask was then used to expose a glass substrate spin-coated with a layer of photoresist. After this the photoresist from unexposed areas was removed leaving a clear glass surface. The thickness of the film was chosen to ensure that light

travelling through areas where the film had been deposited became exactly out of phase with light travelling through film-free areas for $\lambda = 750$nm (equivalent to the transmission function in Fig. 2.4). The apodization mask was also made using the same technology but in this case the chromium-on-glass master was used directly.

The elements of the optical train were linked by achromatic doublet lenses. It is important to note that compared to Fig. 2.2 our experimental setup in Fig. 2.7 included an extra $4f$ imaging stage. This was for two reasons: first, the pupil plane of high NA objective lenses is positioned inside the lens body and hence it would be impossible to physically place the apodization mask in this position. Second, having an extra imaging stage allowed us certain flexibility in matching objective lenses with different pupil sizes to the fixed diameter of our annular ring.

The specimens were mounted on a high precision scanning stage (P-611.3S NanoCube, PI Instruments, Karlsruhe) which provided a scanning range of 100μm in all three dimensions and could be easily reconfigured between X-Y and X-Z scans. Signal detection was provided by a large area photomultiplier, which was coupled to the objective lens via a dichroic beamsplitter.

In order to characterize the imaging properties of our system we began by measuring its illumination PSF. This can be done in a variety of ways but the most direct is to use a sub-resolution scatterer. This method has the added advantage of producing data with a very good signal-to-noise ratio and hence is capable of revealing fine details in the shape and orientation of the PSF which helps with aligning the illumination optics.

We chose to use colloidal gold particles (British BioCell International) of nominal diameter 100nm, which have been shown previously to be a good approximation to dipole scatterers [27]. The assumption of dipole scattering permits us to write an expression for the image formed in our system (essentially a conventional microscope)

as [27]:

$$I(r,\phi,z) = (|I_0|^2 + (I_0 I_2^* + I_0^* I_2)\cos 2\phi + |I_2|^2)(f_0 + f_2) + 16|I_1|^2 f_1 \cos^2\phi, \quad (2.10)$$

where I_0, I_1 and I_2, are once again given in Eqs. 2.3-2.5. This expression again assumes that the input illumination is linearly polarized in the pupil plane along the x-direction. The constants f_0, f_1 and f_2 are related to the detection efficiency for the scattered light assuming that light is collected over the the full extent of the objective aperture. Expressions for these are given by [27]:

$$f_0 = \int_0^\alpha (1+\cos\theta)^2 \sin\theta \cos^{1/2}\theta \, \mathrm{d}\theta, \quad (2.11)$$

$$f_1 = \int_0^\alpha \sin^2\theta \cos^{1/2}\theta \, \mathrm{d}\theta, \quad (2.12)$$

$$f_2 = \int_0^\alpha (1-\cos\theta)^2 \sin\theta \cos^{1/2}\theta \, \mathrm{d}\theta, \quad (2.13)$$

where α is the maximum angle of convergence of the objective lens used. Fig. 2.8 shows numerical simulations of the images generated by scanning a gold bead in the XY and XZ planes using a 1.4NA 63X Zeiss oil immersion objective lens with the following (experimental) parameters - $w = 0.8mm$, $t = 25mm^{-1}$, $\lambda = 750nm$, $R_0 = 3.33mm$ (as measured in the objective pupil plane), $d/R_0 = 0.05$.

The sample for this experiment was made by diluting a suspension of gold beads, drying a drop of this solution onto a coverslip and then mounting it with immersion oil onto a microscope slide. The image of one such gold bead taken with our system is also shown in Fig. 2.8 and exhibits a pleasing match with the theoretical simulations shown on the same figure.

We then proceeded to measure the two-photon fluorescence PSF directly by using fluorescent polymer beads rather than gold beads. Since the overall PSF is the square of the illumination PSF we can see from Fig. 2.8, which is effectively the illumination PSF, that the relatively small dip in the middle of the figure will be

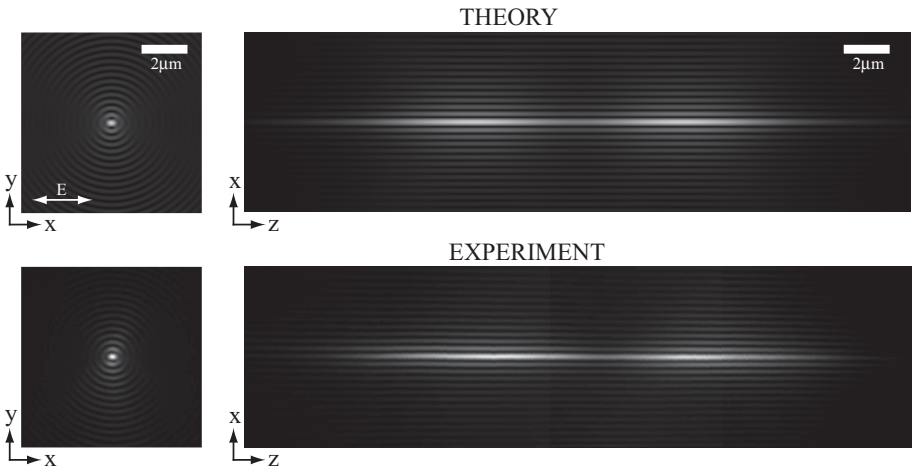

Figure 2.8: *Numerical simulations (top) and the corresponding experimental images (bottom) generated by scanning a sub-resolution gold bead in the XY and XZ planes in reflection mode using annular illumination. See text for parameters used.*

further emphasized when squared. We were therefore compelled to chose a different set of illumination parameters corresponding to less aggressive depth extension in order to flatten the resulting PSF.

If we assume that the sub-resolution fluorescent object emits fluorescence radiation isotropically at a rate proportional to the square of the illumination intensity then we may write the image intensity as:

$$I(r,\phi,z) \propto \left\{ |I_0 + I_2 \cos 2\phi|^2 + |I_2 \sin 2\phi|^2 + |2I_1 \cos \phi|^2 \right\}^2, \tag{2.14}$$

where I_0, I_1 and I_2, are once again given by Eqs. 2.3-2.5. Using the set of parameters $w = 0.5mm$, $t = 25mm^{-1}$, $\lambda = 750nm$, $R_0 = 3.33mm$, $d/R_0 = 0.05$, $NA = 1.4$ oil immersion we arrived at the numerical simulation shown in Fig. 2.9.

Our sample for this experiment was a fluorescent polymer bead (Molecular Probes Fluosphere 505/515 $dia \approx 200nm$). When imaging this sample a dichroic beam-splitter and band pass filter were used in the detection path to separate out the two photon fluorescence signal from miscellaneous reflections of the laser beam. An example image of one such polymer bead is shown in Fig. 2.9, again in corre-

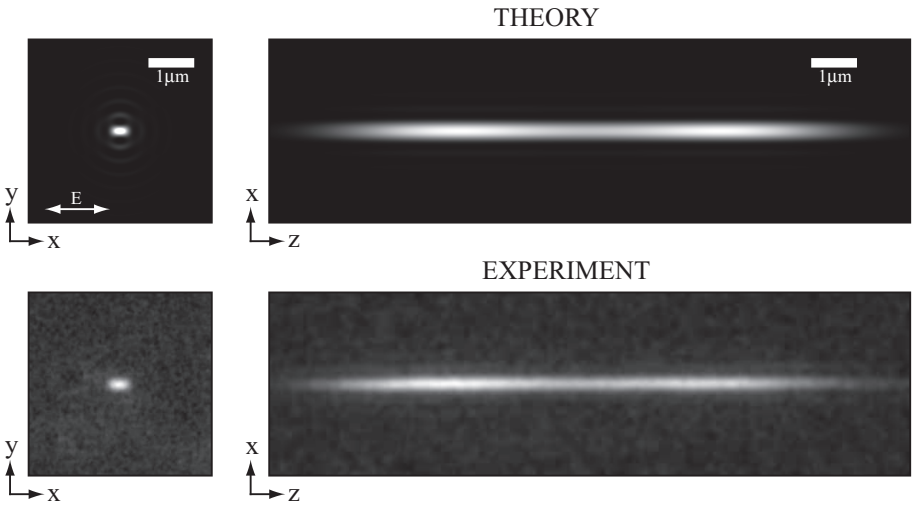

Figure 2.9: *Numerical simulations (top) and the corresponding experimental images (bottom) generated by scanning a sub-resolution fluorescent polymer bead in the XY and XZ planes in two-photon fluorescence mode using annular illumination. See text for parameters used.*

spondence with the theoretical plot.

It is worth noting that despite the fact that the bead size has increased by a factor of two (and thus the number of available fluorescent molecules by a factor of eight) as compared to the $100nm$ beads we used before, the signal-to-noise ratio in Fig. 2.9 is still significantly worse than that in Fig. 2.8. This signal-to-noise was further compromised by the fact that the imaging of the beads was accompanied by severe photobleaching and hence no averaging was possible. This in our opinion makes the scatter method far more reliable and accurate for probing imaging properties of the two-photon microscope.

2.4 Imaging

We now show examples of images taken using the extended depth of focus PSF generated with the binary phase grating and apodization mask. Our test specimen was the pollen grain shown in the introduction from the Asteraceae family that is found in a commercial sample (Carolina w.m. 30- 4264 (B690)). This specimen, with

a diameter of $\approx 20\mu m$, was of particular interest to us because of its micro-spikes. These are useful for demonstrating the lateral resolution of our system.

For comparison purposes, we modified our system to enable us to acquire standard, non extended depth, two-photon fluorescence images. This was done by removing all the masks from the path and expanding the beam to fill the back aperture of the objective lens. An image of our test specimen taken with a single XY scan is shown in Fig. 2.10a and this clearly demonstrates the sectioning capability of two photon systems due to the restricted axial extent of the PSF.

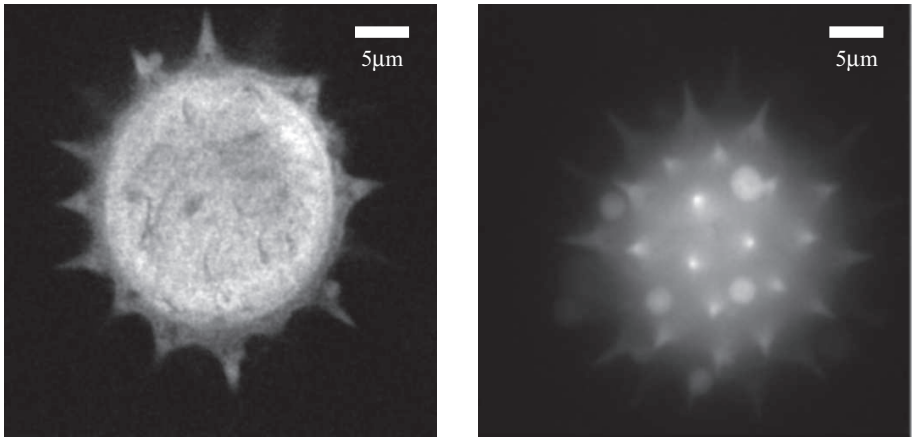

Figure 2.10: *a) A typical two photon fluorescence image of a pollen grain exhibiting sectioning. b) A typical extended depth of focus two photon fluorescence image of a pollen grain taken in a single scan. Line averaging was used to improve the SNR whereby each line in the image was measured four times and averaged to produce the final result.*

Returning to the setup in Fig. 2.7, an image of a similar pollen grain was acquired with a single frame scan in about 45 seconds. This image, which is shown in Fig. 2.10b, clearly demonstrates the effect of our extended depth of focus PSF. In this case it is clear that information from a whole range of depths is presented simultaneously. This is equivalent to constructing an image using the procedure shown in Fig. 1.9, on Pg. 11, where a number of scans from the normal two photon microscope and superimposed on top of each other. Furthermore, it can be seen that the lateral resolution has in no way been compromised in this image.

2.5 Stereo Imaging

Finally, we demonstrate a further application of our extended depth of focus PSF to high resolution two photon stereoscopic microscopy. In a conventional stereo microscope each eye views the object through a slightly different angle [28]. As mentioned in the introduction, this results in a lateral separation of the left- and right-hand images of each object point, the magnitude of which depends on the axial distance from the focal plane. In this way the observer gains a sense of depth perception in an image.

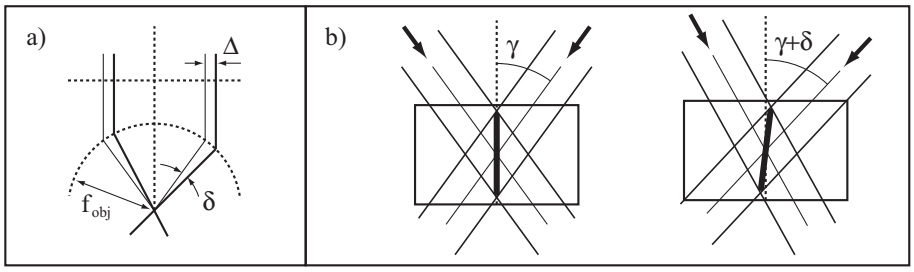

Figure 2.11: *Laterally shifting the annular pupil function results in a change of parallax angle for the extended PSF. This is shown geometrically in a) and a closeup of the focal region is shown in b)*

It is clear from Fig. 2.10b that images taken with our system appear to be viewed along one particular direction. This direction is in fact defined by the orientation of the PSF and by changing this orientation we can change the effective viewpoint. Fig. 2.11 shows how we can change the PSF orientation by introducing a lateral shift to the annular illumination. An example is shown in Fig. 2.12 where two images were taken with the PSF oriented at $\pm 6^\circ$ to produce a high resolution stereoscopic image pair. The lateral shift, Δ, of the annulus may be written in terms of the parallax angle, δ, from geometric considerations as

$$\Delta = \delta f_0 \cos\gamma \tag{2.15}$$

where γ is the angle of convergence to the focal point when the ring illumination is

centred on the objective lens pupil.

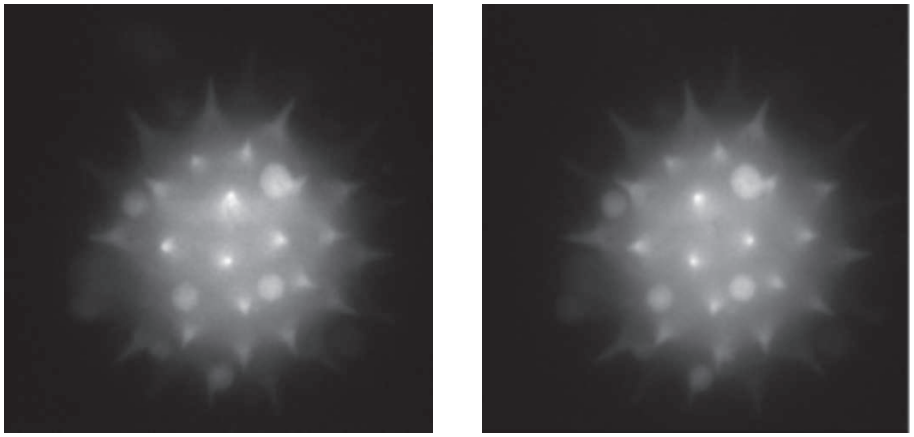

Figure 2.12: *A stereoscopic image pair taken with an extended depth of focus PSF in two photon fluorescence mode. Line averaging was used to improve the SNR in each.*

We would like to emphasize that the extended depth of focus imaging and the ability to produce high resolution stereo images are intrinsically linked to each other. Stereo imaging relies on the parallax effect, i.e. apparent lateral shift of the parts of the object that are outside the focal plane when the point of view is changed. Unless one has access to extended depth of focus imaging those out of focus features would be either blurred (as in conventional microscopy) or not visible at all (in the case of confocal or two photon microscopy). Extended depth of focus is therefore a necessary prerequisite for high-resolution parallax based stereo microscopy.

2.6 Conclusion

In this chapter we have described the use of a binary phase-only grating to produce a ring-shaped distribution of light as an intermediate step in the production of high NA Bessel beams for scanning microscopy. We have shown theoretically that this simple and relatively inexpensive diffractive element was able to produce the required beam with efficiency exceeding 75%. This enabled us for the first time to obtain two photon fluorescence images with a depth of field extended by more than an order of

magnitude. Moreover, we introduced a further step of spatial filtering in the Fourier plane of the mask which enabled us to fine tune the axial profile of the illumination PSF and thus achieve a near constant image intensity throughout the depth of field. It has to be emphasized that all these enhancements in depth of field were achieved without compromising the lateral resolution of the microscope. The potential scope of application of this method was further broadened by demonstrating a stereo imaging capability. This was achieved by obtaining a pair of extended depth of field images from different viewing parallaxes by employing tilted PSFs.

Although the images presented in this chapter were acquired by physically scanning the object in the lateral plane, it would also have been possible to achieve the same results with a beam scanning approach using galvanometer mirrors, as described in the introduction on Pg. 15. In this way, acquiring an extended depth of field image of the specimen could be carried out at the same speed as recording an image from a single specimen plane with a standard two photon microscope. As such, this technique could find application in situations where it is of interest to survey large volume structures quickly using extended depth of field imaging.

Chapter 3

Remote focusing in microscopy

In this chapter, a fundamentally new method of optical refocusing is described that can be generally applied to any microscope imaging system. This method in principle overcomes the spherical aberration that is common to other optical refocusing techniques and is therefore particularly relevant for confocal and multiphoton microscopy systems. As refocusing is implemented remotely from the specimen, this method enables high axial scan speeds without mechanical interference between the objective lens and the specimen. A full theoretical analysis is carried out and predictions for the range of operation are made.

3.1 Introduction

As we have already said, a common requirement in high-resolution optical microscopy is to obtain a three-dimensional representation of the object under investigation. This is typically achieved via an intermediate step using an optical sectioning technique, such as confocal microscopy [3], to obtain a clean in-focus image of a single plane within the sample. This process is repeated a number of times at different focal settings and gradually a full three dimensional data set containing information about the whole object is gathered. In most practical implementations

a single in-focus image can be acquired very quickly. However, the real bottleneck in three dimensional data acquisition is the process of refocusing the microscope to successive image planes. High-resolution microscope objective lenses are designed to provide aberration free images from a unique focal plane. There are fundamental optical reasons, which we will discuss, why it is not possible to achieve decent imaging at different image conjugates in high-aperture microscopy as opposed to, say, photographic cameras where such imaging is routine. Therefore the only viable solution in microscopy, up until now, has been to keep the imaging plane fixed and to change the distance between the object and imaging lens mechanically. Attempts have been made to improve the speed at which this can be done by using piezoelectric elements [29, 30] however this speed is still limited by the fact that the imaging lenses and/or the specimen are relatively heavy. These methods can also suffer from additional disadvantages, such as specimen agitation, which make imaging of delicate samples, such as live cell cultures, very difficult.

An alternative focusing method that does not involve mechanical movements near the specimen is clearly preferable. Attempts have also been made to do the refocusing remotely using vari-focus lenses [31], micro electromechanical mirrors [32] and acousto-optics modulators [33] but all suffer from aberrations introduced by the focusing elements. It has also been suggested that deformable mirrors could be used to correct the aberrations in conjunction with one of these focusing methods, but this introduces an extra unnecessary level of complexity to the system.

In this chapter we will review, from a theoretical standpoint, the problems associated with refocusing in high numerical aperture (NA) microscopy. We will then investigate an optical method [34], that circumvents many of these problems and enables refocusing to be carried out remotely without the introduction of systematic aberration, and analyze the range of operation.

3.2 Imaging in three dimensions

In what follows we shall confine ourselves to the class of optical systems that are rotationally symmetric about the optic axis and so it is possible to restrict our analysis to the meridional plane without loss of generality. A concept that is useful when considering optical instruments is that of a *perfect imaging system*. Such a system is one that can form a stigmatic image of any point from a three dimensional domain or equivalently forces all rays emanating from a single point in object space to re-converge at a single point in image space.

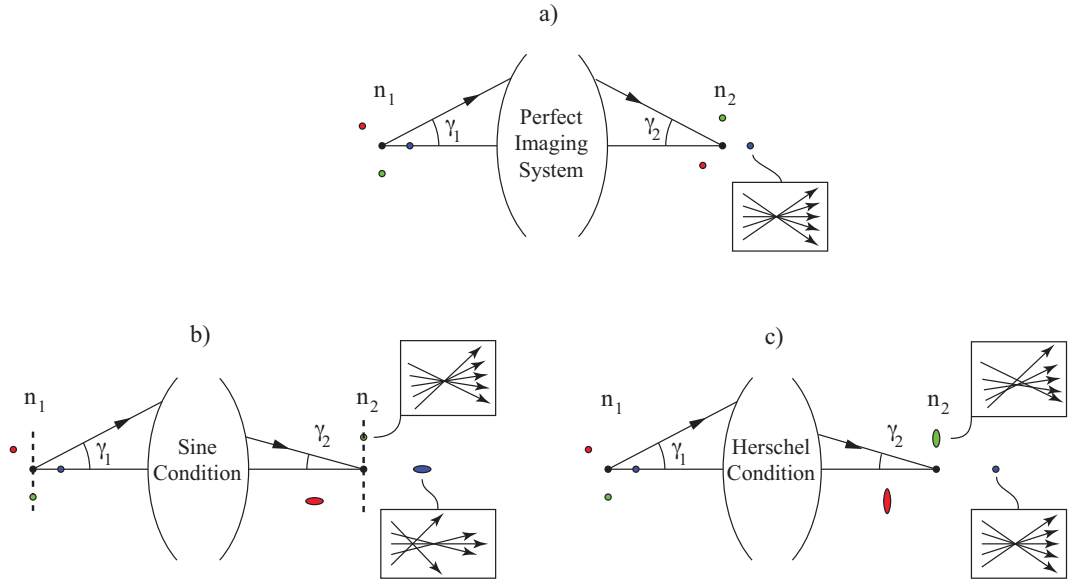

Figure 3.1: *Imaging four point sources in the meridional plane using a) a perfect imaging system, b) a system obeying the sine condition and c) a system obeying the Herschel condition.*

Such a system is shown in Fig. 3.1a where the object and image spaces are immersed in media of refractive indices n_1 and n_2 respectively. A single ray is shown emanating from the origin of object space with angle γ_1 together with the conjugate ray that it is mapped onto, which travels through the origin of image space with angle γ_2. We show how four point sources placed at different locations in the meridional plane are imaged by this system and further show explicitly how

the rays converge for one of the off-axis points. The angular spectrum of rays that emerges in the region beyond the image space is identical to that produced by the original object within the angular passband of the system.

The requirement of perfect three dimensional imaging imposes quite a constraint on the design parameters of such a system and it has already been shown by Maxwell in 1858 [12] that the magnification M must necessarily be the same along all directions and have a magnitude of

$$|M| = \frac{n_1}{n_2}, \tag{3.1}$$

which for many situations is close to unity as n_1 and n_2 often have similar values. It can be shown [23] that this requirement also implies that all conjugate rays must propagate with the same angle with respect to the optic axis, i.e.:

$$\gamma_2 = \pm\gamma_1. \tag{3.2}$$

An important corollary of this is that any system introducing a magnification different from Eq. 3.1 cannot produce a perfect image. Such is the case in microscopy, for instance, where systems are designed to grossly magnify the object under investigation and consequently there is a breakdown of perfect three dimensional imaging. For cases where the object is of small linear dimensions, however, it is still possible to maintain perfect imaging for a subset of points in object space and there are two well known design conditions. These are the sine condition, which enables points in a plane, perpendicular to the optic axis, to be imaged perfectly, and the Herschel condition which allows points along the axis to be imaged perfectly [23]. It is often necessary to chose between these two conditions according to the application.

Most microscopes are designed according to the sine condition, and in Fig. 3.1b we show how such a system behaves when imaging the same array of point sources. Here we see that points lying in a unique plane, shown as a dashed line in object

space, are imaged stigmatically in image space with a lateral magnification of M_l whereas points displaced axially form non-stigmatic images. The paraxial rays still converge, however, with an axial magnification of $M_l^2 n_1/n_2$, whereas the rays traveling at higher angles tend to focus to points closer to the focal plane. This effect is commonly referred to as spherical aberration and gets progressively worse for larger axial displacements. The sine condition also imposes a different transformation between the conjugate rays, as shown, which is described by the following equation [23]:

$$\sin\gamma_2 = \frac{n_1}{n_2}\frac{\sin\gamma_1}{M_l}. \tag{3.3}$$

From these considerations it is possible to see why commercial microscopes, operating under the sine condition refocus by changing the distance between the specimen and objective, as any attempt to detect images away from the optimal image plane will lead to a degradation of image quality by spherical aberration.

In Fig. 3.1c we show how a system obeying the Herschel condition behaves when imaging the array of point sources. In direct contrast with the sine condition, points lying along the optical axis are now imaged perfectly in the image space with an axial magnification of M_a whereas laterally displaced points are not. The transformation between conjugate rays in this case is given by [23]:

$$\sin^2(\gamma_2/2) = \frac{n_1}{n_2}\frac{\sin^2(\gamma_1/2)}{M_a}. \tag{3.4}$$

For the specific case where a system is designed to obey the sine condition with a lateral magnification of $M_l = n_1/n_2$ Eq. 3.3 reduces to Eq. 3.2 and perfect imaging then follows for the whole three dimensional domain. In the same way, a system designed to obey the Herschel condition with an axial magnification of $M_a = n_1/n_2$ also permits perfect imaging with Eq. 3.4 once more reducing to Eq. 3.2.

3.3 The general pupil funcion

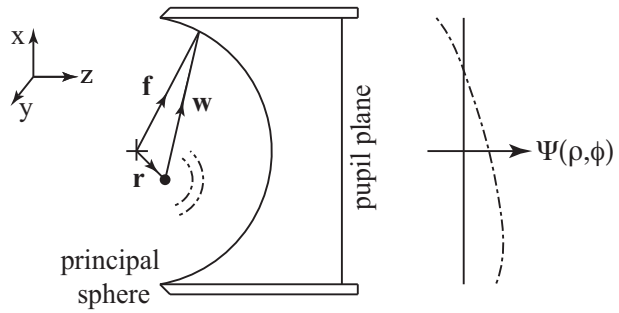

Figure 3.2: *A mathematical model used for high NA objective lenses.*

We now take a closer look at the specific geometry of a high NA microscope objective which can be modelled as a pair of principal surfaces that are spherical and planar in shape as shown in Fig. 3.2 [23, 35]. A point source, placed at the origin of object space, emits a spherical wave which, upon crossing the principal sphere, is transformed into a plane wave in the pupil. In a microscope, such a lens if used in conjunction with a low NA tube lens (not shown) which then focuses this plane wave stigmatically to a point in image space.

A point placed at some different location, $\mathbf{r} = (x, y, z)$, also emits a spherical wave but in this case different parts of the wavefront cross the principal sphere at different times producing a more complex phase profile in the pupil plane. We denote a general point on the principal sphere with vector $\mathbf{f}$, which has a magnitude of f, and draw a second vector $\mathbf{w}$ from the point source to this same point. The relative path length difference between these rays is given by:

$$PD = |\mathbf{w}| - f = |\mathbf{f} - \mathbf{r}| - f = \left\{f^2 - 2\mathbf{f} \cdot \mathbf{r} + r^2\right\}^{1/2} - f, \tag{3.5}$$

where r is the magnitude of the source displacement. We can develop this further by

writing each component of $\mathbf{f}$ in spherical polar form, $\mathbf{f} = f(\sin\theta\cos\phi, \sin\theta\sin\phi, \cos\theta)$:

$$PD = f\left\{1 - \frac{2}{f}\left(x\sin\theta\cos\phi + y\sin\theta\sin\phi + z\cos\theta\right) + \frac{r^2}{f^2}\right\}^{1/2} - f. \tag{3.6}$$

Expanding this to first order, assuming $r \ll f$, gives:

$$PD \approx -\frac{\mathbf{f}\cdot\mathbf{r}}{f} = -\left(x\sin\theta\cos\phi + y\sin\theta\sin\phi + z\cos\theta\right), \tag{3.7}$$

which, interestingly, does not depend on f. The phase profile in the pupil plane can be found by invoking the sine condition which maps rays between the principal surfaces whilst preserving their distance from the optic axis:

$$\sin\theta = \rho\sin\alpha. \tag{3.8}$$

In this expression α is the semi-aperture acceptance angle of the lens and ρ is the normalized pupil radius. Applying this transformation and multiplying the result by the vacuum wavenumber k leads to an expression for the phase profile in the pupil plane as function of the point source position:

$$\Psi(\rho, \phi; \mathbf{r}) \approx nk\sin\alpha\left\{x\rho\cos\phi + y\rho\sin\phi + z\sqrt{cosec^2\alpha - \rho^2}\right\}, \tag{3.9}$$

where a refractive index of n has been included to account for the case where the focal region is surrounded by an immersion medium and ϕ, which was previously the azimuthal angle in object space becomes the azimuthal angle in the pupil plane.

There are a number of conclusions that can be drawn from the form of this pupil function. First, it can be seen that lateral displacements of the point source produce plane waves in the pupil with an amount of tip ($\rho\cos\phi$) or tilt ($\rho\sin\phi$). These flat waveforms, which are a direct result of the sine condition, are then focused stigmatically by the tube lens to laterally displaced points in image space. Second,

we see that axial displacement leads to a curved phase profile which can be expanded in powers of ρ to give:

$$znk\sqrt{1-\rho^2\sin^2\alpha} = znk\left\{1-\frac{\rho^2\sin^2\alpha}{2}+\frac{\rho^4\sin^4\alpha}{8}+...\right\}, \tag{3.10}$$

which may be thought of as the phase profile for high NA defocus. Focusing using the tube lens is accurately described by the quadratic term, as it operates in the paraxial regime. Unfortunately the higher order terms which represent spherical aberrations cannot be focused by the tube lens and consequently there is a breakdown of stigmatic imaging for these points.

If, on the other hand, the objective had been designed to satisfy the Herschel condition, to give perfect axial imaging, the mapping of Eq. 3.8 would be replaced by:

$$\sin(\theta/2) = \rho\sin(\alpha/2), \tag{3.11}$$

and the corresponding phase function becomes:

$$\Psi(\rho,\phi;\mathbf{r}) \approx 2nk\sin^2(\alpha/2)\left\{(x\rho\cos\phi+y\rho\sin\phi)\sqrt{cosec^2(\alpha/2)-\rho^2}+z\left(\frac{cosec^2(\alpha/2)}{2}-\rho^2\right)\right\}, \tag{3.12}$$

where we notice that the defocus term is accurately described by a quadratic and so results in a perfect axial focus. Lateral displacements, however, result in a curved phase profile which cannot be focused stigmatically.

A particularly interesting property of the pupil functions derived here is the odd parity that they possess which can be formally stated as:

$$\Psi(\rho,\phi;-\mathbf{r}) = -\Psi(\rho,\phi;\mathbf{r}). \tag{3.13}$$

This is simply the statement that a point source placed at $\mathbf{r}$ produces an equal and

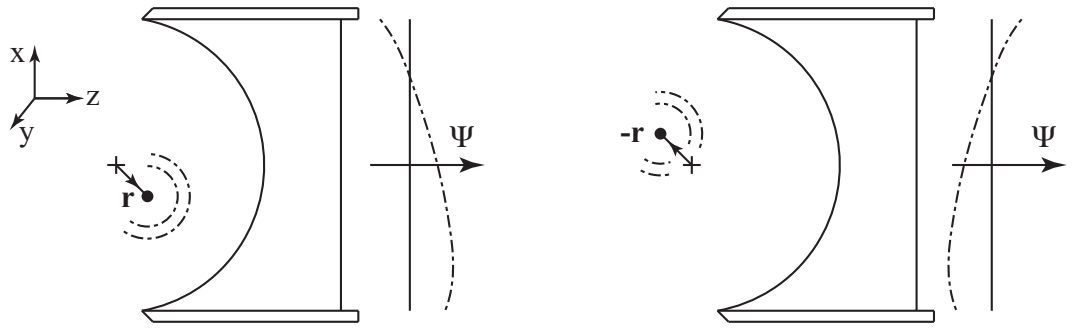

Figure 3.3: *Demonstration of odd parity pupil functions*

opposite phase distribution to a source placed at $-\mathbf{r}$ as can be seen in Fig. 3.3. This odd parity condition is the direct result of the form of Eq. 3.7 and is therefore applicable to the sine condition, Herschel condition and other transformations such as the uniform projection condition and Helmholtz condition.

Due to the reciprocal nature of ray optics we also note that if a wavefront could be generated at the pupil plane with the same form as that in Eq. 3.9 but travelling into the lens then there would be stigmatic convergence of all rays to a single point. Such wavefronts could be manufactured with a deformable mirror. However, a simpler method can be inferred by considering the situation in Fig. 3.3. If the orientation of the second lens were reversed and the pupil function from the first lens was imaged into the pupil plane of the second lens then the wavefront would be of exactly the right form to cause convergence to a single point. This applies for all positions of the initial point source in three dimensions as long as $r \ll f$ and is the direct consequence of the odd parity condition.

3.4 A technique for remote focusing

We now suggest a strategy that allows refocusing to be carried out without moving the object under examination. In essence, this strategy involves constructing a perfect imaging system which replicates the three dimensional distribution of object

space in the focal region of a second high NA objective lens with a magnification of n_1/n_2, as just described, and then uses a further microscope to image this replica. Refocusing is then carried out by moving the microscope with respect to the replica, which can be done without introducing any movements near the object itself.

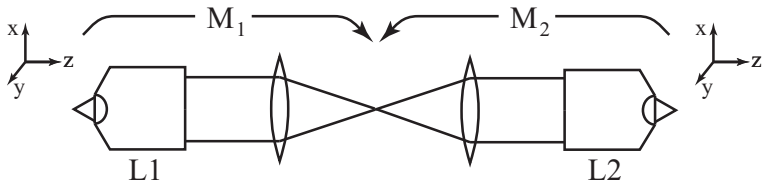

Figure 3.4: *Perfect imaging system.*

The first stage is shown in Fig. 3.4 and comprises two objective lenses back-to-back with a 4f imaging stage mapping the pupil planes together. In general the objective lenses L1 and L2 need not be identical and may operate with different immersion media - n_1 and n_2 respectively. For the practical case of objectives obeying the sine condition, we can write down the phase profile generated in the pupil plane of this system for a point source located at the position (x, y, z) in the focal region of L1:

$$\Psi_1(\rho_1, \phi) = kn_1 \sin\alpha_1 \left(x\rho_1 \cos\phi + y\rho_1 \sin\phi + z\sqrt{cosec^2\alpha_1 - \rho_1^2} \right). \tag{3.14}$$

It is also possible to write down the phase profile required to focus all the rays stigmatically to a point located at $(n_1/n_2) \times (x, y, z)$ in the focal region of $L2$:

$$\Psi_2(\rho_2, \phi) = kn_2 \sin\alpha_2 \frac{n_1}{n_2} \left(x\rho_2 \cos\phi + y\rho_2 \sin\phi + z\sqrt{cosec^2\alpha_2 - \rho_2^2} \right), \tag{3.15}$$

where the coordinate system is defined in the diagram. If the 4f system mapping the pupil planes together has magnification:

$$M = \frac{\rho_2}{\rho_1} = \frac{\sin\alpha_1}{\sin\alpha_2} \tag{3.16}$$

then it can be seen that the two phase profiles become identical and the point source is stigmatically imaged in the focal region of L2. As a result, the system images a three dimensional region of object space with an isotropic magnification factor of n_1/n_2, consistent with the requirements of a perfect imaging system (Eq. 3.1 on Pg. 46).

The design of the perfect imaging system can also be understood by considering the system as two separate microscope systems back-to-back such that the first magnifies the object by a factor M_1 and the second demagnifies by M_2. In this situation both the lateral and axial magnifications of microscope combination yield the same value of n_1/n_2, as required for perfect imaging of the three dimensional domain. In effect the spherical aberration introduced by the first system is directly compensated by that introduced by the second. Care must be taken, however, when constructing the system in this way to ensure that the tube lenses form a 4f imaging system linking the pupil planes.

We also note that rays from the object space are mapped onto conjugate rays with the same angle in image space, in accordance with Eq. 3.2 (Pg. 46). As such it is possible to see that the limiting angular aperture in the system γ_{max} will essentially limit the overall resolution of the instrument. The numerical aperture of the whole system can therefore be evaluated by projecting this angle back into the object space to find $NA = n_1 \sin \gamma_{max}$. This implies that as long as the second objective has a higher *angular aperture* than the first it will not restrict the resolution, a situation that is easily realized when using say, a 1.4NA oil immersion lens and a 0.95NA dry lens as L1 and L2 respectively.

Having produced a three dimensional replica of the object we could now magnify and image planes of this replica using a third microscope system, which might also comprise a high NA objective lens (L3) and tube lens, as shown in Fig. 3.5a. Refocusing is carried out by moving L3 axially so that different planes of the intermediate image space are imaged without spherical aberration. As a result, we have

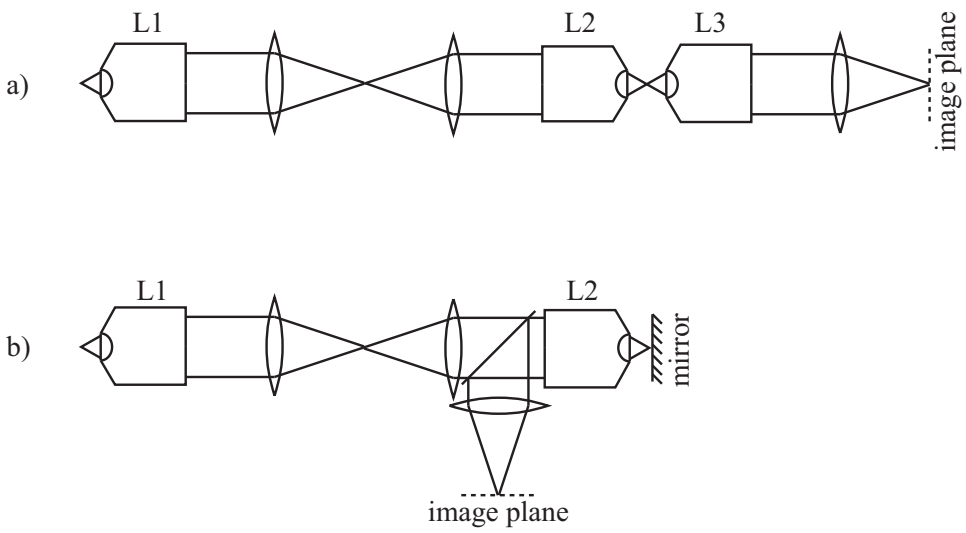

Figure 3.5: *Two systems comprising a perfect imaging system and a further microscope for magnification.*

constructed a system where refocusing can be carried out remotely, without moving the specimen or objective and without introducing spherical aberration.

We also present a second system that enables superior axial scan speeds while refocusing. This is shown in Fig. 3.5b and is optically identical to the system already discussed. In this arrangement a plane mirror reflects the rays from the intermediate image space back into L2 and a beam splitter is further used to direct these towards the final tube lens and image plane. L2 is therefore used twice: once, as part of the perfect imaging system, to cancel the aberrations introduced by L1 and once as part of the third microscope. By moving the mirror, it is possible to change which plane of the object is imaged perfectly at the image plane without spherical aberration. As the distribution in the intermediate image space has roughly the same dimensions as the object itself the mirror can be very small and can therefore be scanned quickly, providing faster refocusing speeds than were possible by moving L3 in the previous arrangement.

3.5 Range of operation

In constructing the perfect imaging system shown in Fig. 3.4, we have assumed that both objective lenses conform strictly to the sine condition. It has been shown that a point source placed at some arbitrary position in the focal region of L1 will form a stigmatic image in the focal region of L2 if the phase profile generated in the pupil plane of the system is described by Eq. 3.9. It is important to note, however, that this phase profile is only the lowest order contribution arising from the expansion of the more general expression in Eq. 3.6, on Pg. 49. As such, it is a good approximation when considering small displacements from focus however a full description must incorporate the higher order terms of the expansion too. These higher order terms lead to a degradation of stigmatic convergence and hence to a breakdown of the perfect imaging. In this section we therefore establish the axial range over which perfect imaging occurs.

For the purposes of simplicity, we consider the case where both objective lenses are identical and their pupil planes are mapped together with a 4f imaging system with unit magnification. In the first approximation we found that a point source located at a distance z along the axis from the focus of L1 forms a conjugate image point a distance z along the axis from the focus of L2. A general ray travelling between these two points crosses the pupil plane at position (ρ, ϕ) and carries a phase due to its relative path length during propagation. It is possible to find the relative phase of each ray travelling between these conjugate points by summing the individual contributions introduced by each objective, as defined in Eq. 3.6:

$$\Delta\Psi = nkf\left[2 - \left\{1 - \frac{2z}{f}(1-\rho^2\sin^2\alpha)^{1/2} + \frac{z^2}{f^2}\right\}^{1/2} - \left\{1 + \frac{2z}{f}(1-\rho^2\sin^2\alpha)^{1/2} + \frac{z^2}{f^2}\right\}^{1/2}\right] \tag{3.17}$$

If the path length difference between the point source and conjugate image point is the same for all rays then stigmatic imaging follows, which equivalently requires

this expression to be constant across the pupil plane. This is the case for small displacements, as the first order terms in the binomial expansion of each contribution cancel, forcing $\Delta\Psi$ to be zero across the pupil. For larger displacements, though, higher order terms in the expansion will have a contributory effect. Expanding Eq. 3.17 to find the term in z^2 yields:

$$\Delta\Psi = -\frac{nk\rho^2 \sin^2 \alpha}{f} z^2. \tag{3.18}$$

In effect, this residual phase profile describes the deviation of the wavefront in the pupil plane from the one required to produce perfect imaging of a point source at position z in the focal region of L1. This deviation causes non-stigmatic convergence of the rays in the focal region of L2.

A useful way of characterizing the degradation of stigmatic imaging is to calculate the Strehl ratio, which is defined as the ratio of the peak intensity of the focal spot produced when the point source is at position z compared with that produced when it is in focus. This can be calculated from the knowledge of the residual aberration in Eq. 3.18, but first it is necessary to identify the components of this function that are responsible for the reduction in the peak intensity. To do this, we expand the function in terms of a linear set of orthonormal basis modes, Ψ_n:

$$\Delta\Psi = \sum_n a_n \Psi_n, \tag{3.19}$$

where each mode corresponds to a different fundamental aberration with a magnitude that is characterized by coefficient a_n. It is important to choose a suitable set of basis modes that is appropriate for use with high NA lenses and methods for deriving these have been described by Sheppard [36]. In general, each mode in this expansion can potentially degrade the peak intensity of the focal spot formed except for the modes describing *piston* and *defocus* which are given by the following

equations:

$$\begin{aligned} \Psi_p &= 1, \\ \Psi_d &= nk(1-\rho^2\sin^2\alpha)^{1/2} - \frac{2nk}{3\sin^2\alpha}(1-\cos^3\alpha). \end{aligned} \tag{3.20}$$

As can be seen, piston (Ψ_p) is associated with a constant phase offset across the pupil whereas defocus (Ψ_d) has a more complicated form which can be inferred from Eq. 3.10 on Pg. 50 as $[nk(1-\rho^2\sin^2\alpha)^{1/2}]$. A constant offset has been added to the latter to ensure that its average value over the pupil is zero. As a result, these modes are orthogonal and the coefficient of piston, which we denote as a, adds a constant phase to all rays whereas the coefficient of defocus, which we denote as δz, can be interpreted as an additional axial shift of the final image point in the focal region of L2. We note that these modes are not normalized. The coefficients a and δz can therefore be evaluated for the residual phase profile in Eq. 3.18 using standard techniques:

$$\begin{aligned} a &= \frac{\int \Delta\Psi\Psi_p\rho d\rho}{\int(\Psi_p)^2\rho d\rho} = -\frac{nkz^2\sin^2\alpha}{2f}, \\ \delta z &= \frac{\int \Delta\Psi\Psi_d\rho d\rho}{\int(\Psi_d)^2\rho d\rho} = \frac{12z^2\cos^2(\frac{\alpha}{2})(3+6\cos\alpha+\cos 2\alpha)}{5f(3+8\cos\alpha+\cos 2\alpha)} \end{aligned} \tag{3.21}$$

From these results it is possible to remove the contributions of piston and defocus from the residual phase profile so as to isolate the components of the function responsible for the reduction in peak intensity of the focal spot formed:

$$\Delta\Psi' = \Delta\Psi - a\Psi_p - \delta z\Psi_d, \tag{3.22}$$

We can now use this to evaluate the Strehl ratio of the system for different locations of the point source along the axis. The Strehl ratio is given by the following

mathematical expression [37]:

$$S = \left| \frac{1}{\pi} \int \int \exp\left(j\Delta\Psi'\right) \rho d\rho d\phi \right|^2 \approx 1 - \frac{1}{\pi} \int \int (\Delta\Psi')^2 \rho d\rho d\phi, \tag{3.23}$$

where integration is over pupil plane and the approximation is valid for Strehl ratios down to a value of 0.8. Inserting $\Delta\Psi'$ from Eq. 3.22 into this expression and performing the integration then yields an analytic result for the Strehl ratio:

$$S = 1 - \frac{4n^2k^2z^4(3 + 16\cos\alpha + \cos 2\alpha)\sin^8\left(\frac{\alpha}{2}\right)}{75f^2(3 + 8\cos\alpha + \cos 2\alpha)} \tag{3.24}$$

This function is plotted in Fig. 3.6a for the case of a 60X 1.4NA oil immersion objective, which has a value of $f = 4.55$mm, and for a wavelength of $633nm$. We see from this that the Strehl ratio is greater than 0.8 for up to $\pm 70\mu m$ of point source displacement. Also plotted in Fig. 3.6b is the coefficient of defocus, δz,

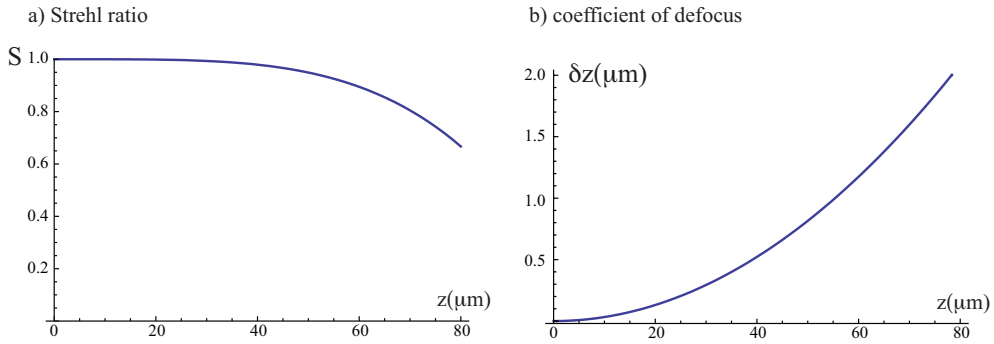

Figure 3.6: *a) The Strehl ratio and b) the coefficient of defocus as a function of point source position for the system shown in Fig. 3.4.*

for different point source positions. This plot shows us that the image point will be slightly displaced along the axis compared with the prediction of the first order theory. Both these functions are even in z and are therefore symmetric about the origin.

As a final comment we point out that further extension of the range over which the system will operate can be realized if these residual aberrations where further

corrected for by a deformable mirror although this would increase the complexity of the system.

3.6 Conclusions

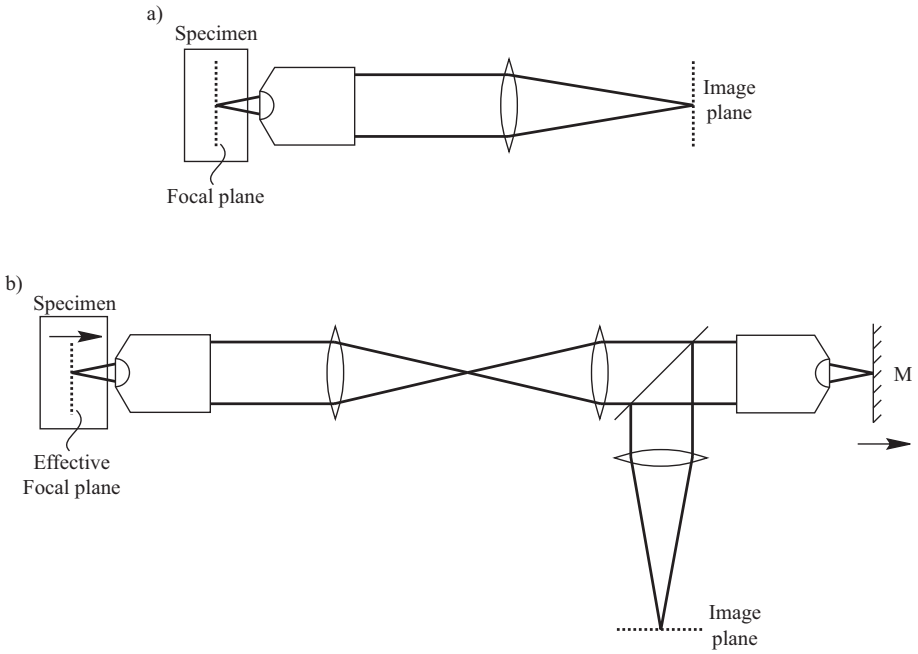

Figure 3.7: a) The standard microscope architecture and b) the new microscope architecture proposed in this chapter.

In this chapter, we have shown that the standard microscope architecture, as shown in Fig. 3.7a, only provides aberration-free images of a unique focal plane in the specimen. As a result, this system cannot be refocused to image other planes of the specimen by simply displacing the image plane along the axis as this process introduces spherical aberration, which degrades image quality. Furthermore, we have shown that this spherical aberration cannot be avoided due to fundamental limitations imposed on lens design. As a result, the only way to gather aberration-free images from different specimen depths, up until now, has been to keep the imaging plane fixed and to change the physical distance between the specimen and imaging lens mechanically.

An alternative microscope architecture, however, can be used to circumvent the problems of spherical aberration and permit refocusing to be carried out remotely. This fundamentally new approach is shown in Fig. 3.7b. The key difference here is that aberration-free images appear on the image plane from an effective focal plane in the specimen that can be changed by moving a small mirror M. In essence, this technique uses a second high NA objective lens to cancel the spherical aberrations introduced by the imaging objective and hence restores diffraction limited performance for different planes of the specimen. A theoretical analysis revealed that this technique permits refocusing to be carried out over a large range of specimen depths if the objective lenses conform strictly to the sine condition.

This approach, of course, is extremely general and can form the basis of any imaging system that was previously based on the standard microscope architecture. As a result, this method applies to a wide range of sectioning techniques such as confocal, two-photon, second- and third-harmonic generation and structured illumination microscopies as well as non sectioning systems.

Arguably, one of the most important advantages of this approach lies in the fact that refocusing is carried out by displacing a small mirror along the axis. Consequently, the speed at which this can be done is no longer limited by the mass of the specimen or imaging objective. Currently available technology permits axial scanning to be carried out over the full range of operation of the 1.4NA 60X objective lens at speeds of up to 1 kHz. This represents a remarkable improvement compared with previously achievable scan speeds which were limited to a few tens of Hz.

Another important advantage that results from this all-optical method of remote focusing is the fact that no mechanical movements are introduced near the specimen during the acquisition of three dimensional image stacks. This circumvents all problems associated with specimen agitation and permits imaging of specimens such as live cell cultures to be carried out more easily.

In the following chapters, experimental PSF measurements will be presented that

demonstrate the imaging performance of this new system and a range of imaging systems based on this new architecture will be shown.

Chapter 4

Point spread function measurements

In order to characterize the imaging properties of the new microscope architecture described in the previous chapter we measured the detection point spread function (PSF) of the system for a number of different focal settings. For the purposes of comparison, we also measured the detection PSF of a standard microscope architecture.

4.1 Measuring the PSF

In this section, we describe a suitable method that can be used to measure the detection PSFs for the two microscope architectures. Fig. 4.1a shows a standard microscope configuration comprising a high NA objective lens and tube lens. A pinhole is placed in the image plane and is associated with a PSF, $h(x, y, z)$, which can be interpreted in two different ways. First, for the case where laser light is introduced into this system via the pinhole, $h(x, y, z)$ is the amplitude distribution setup in the focal region of the objective lens and is commonly referred to as the illumination PSF. Second, for the case where the pinhole is used to filter light

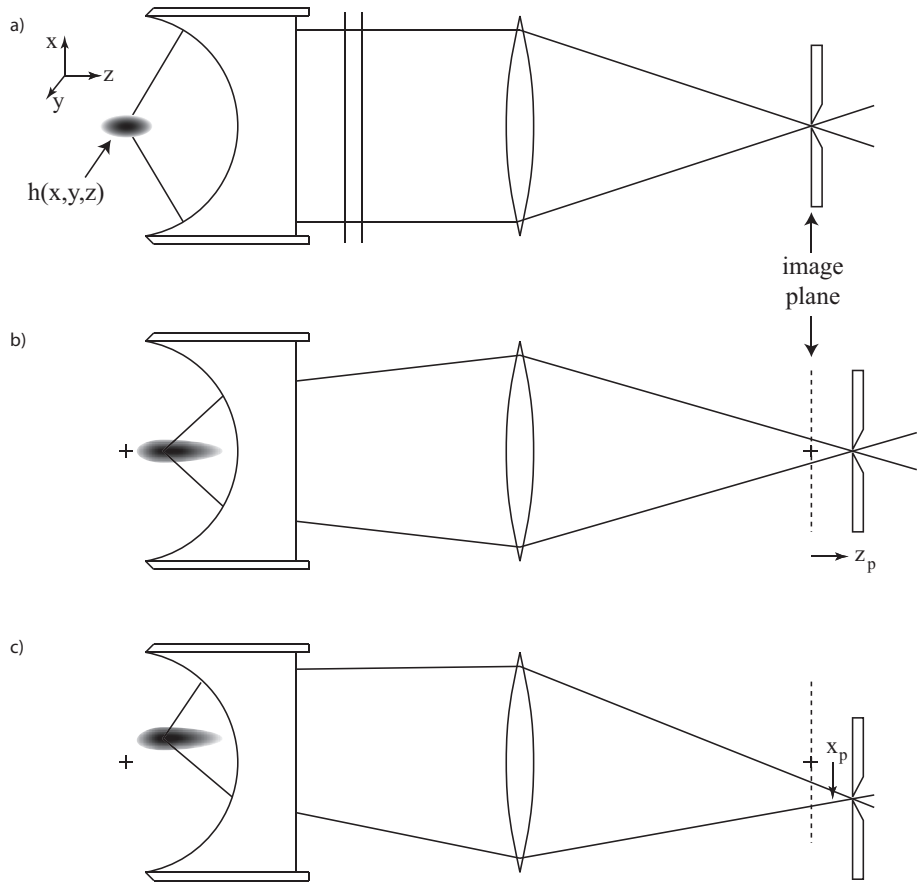

Figure 4.1: The PSF for a microscope system obeying the sine condition.

originating from the focal region of the objective lens, $h(x, y, z)$ is used to describe the sensitivity of the pinhole detector to light emanating from different points in object space and is therefore referred to as the detection PSF. It is worth noting that in the regime of geometric optics, this function is essentially a delta function, located at the origin of object space. In reality though, the effects of wave optics cannot be ignored and the limiting aperture of the optical system causes this function to broaden out and take on significant values over a finite region of spatial extent.

We now make some general remarks about the detection PSF for microscope systems designed to obey the sine condition. Fig. 4.1b shows the same system as before with the pinhole displaced along the axis and demonstrates two important features. First, the PSF is shifted along the axial direction in object space and,

second, its shape is deformed by the introduction of spherical aberration. Fig. 4.1c shows how a further lateral displacement of the pinhole affects the system. In this case the PSF is shifted laterally in the focal region of the objective however its distorted shape remains unaffected by this process. Bearing these properties in mind, it is possible to characterize the PSF shape with a single parameter, z_p, which we now include as one of the co-ordinates in the distribution, $h(x, y, z; z_p)$. It is one of the aims of the current chapter to measure the PSF shape for different values of z_p. The most direct method of doing so would be to scan a point source to different positions in object space, (x', y', z'), and to measure the intensity transmitted by the pinhole at each position. Mathematically, the point source is equivalent to a delta function and so the intensity measured at each position would be:

$$I(x', y', z'; z_p) = \left| \int \delta(x - x', y - y', z - z') h(x, y, z; z_p) \mathrm{d}^3\mathbf{r} \right|^2 = \left| h(x', y', z') \right|^2 , \quad (4.1)$$

which is simply the convolution of the delta function and the PSF, $|\delta \otimes h|^2$. In this way, the delta function picks out the value of the PSF at each particular location. The full detection PSF can therefore be measured by scanning the point source to different locations in three dimensions and measuring the values at each position.

Although it is possible to simulate a point source using various methods [38, 39, 40] these can be hard to implement experimentally. The same results can be obtained more simply however by using a diffraction limited focal spot of laser light instead of a point source. This leads to a considerable simplification of the experimental procedure. The equivalence of the focal spot and point source will be shown shortly.

A schematic diagram of the system used to measure the detection PSF is shown in Fig. 4.2. Here, a plane wave from a laser beam is coupled into the objective pupil using a beam splitter. The lens focuses the light down onto a plane mirror, placed a distance z_m from focus, and forms a diffraction limited focal spot centred at a position $z = 2z_m$. The wavefront that then emerges from the objective lens

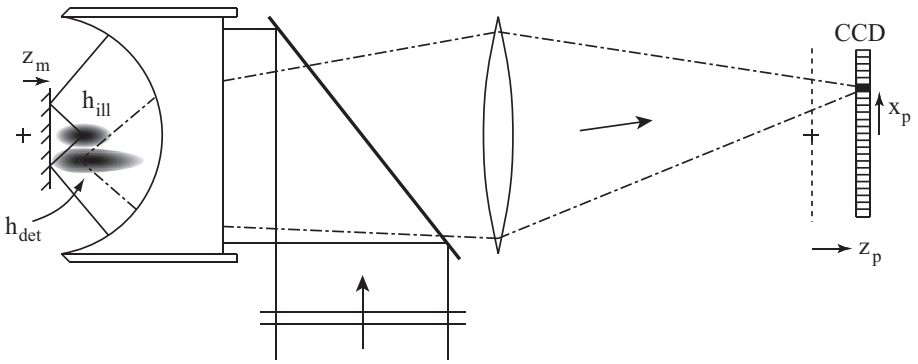

Figure 4.2: Measuring the detection PSF for a microscope system.

is identical to the one that would have been produced by a point source located at position $z = 2z_m$. This will be shown mathematically later on. Using a focal spot to probe the detection PSF therefore yields identical results to a point source, even though it has significant values over a finite region of object space.

In order to measure the detection PSF, the focal spot must still be scanned in three dimensions as before and measurements taken from an array of points. Axial scanning is trivial and can be performed by simply displacing the mirror along the axis. Lateral scanning, on the other hand, is carried out indirectly by replacing the detection pinhole with a CCD camera and recording whole frames of data. The pixels of the CCD effectively act as a two dimensional array of pinholes, each one being associated with its own detection PSF that has the same shape and is displaced laterally in object space. This, of course, is only the case if the dimensions of the pixels are small enough so as to adequately sample the intensity distribution. We will return to this point later on. The detection PSF for a single off-axis pinhole is shown in the Figure. As a result, laterally displaced pixels measure the same response as the original pinhole would have if the focal spot was scanned laterally. The CCD camera therefore measures the intensity distribution of an entire plane of the detection PSF simultaneously with a magnification factor defined by the microscope system. A full three dimensional measurement of the detection PSF can

be obtained by acquiring images from many closely spaced planes while scanning the mirror along the axis.

We now analyze this situation mathematically and show that the diffraction limited spot does indeed produce the same results as for a point source. The intensity measured by a pixel located at (x_p, y_p, z_p) is given by:

$$I(x_p, y_p, z_m; z_p) = \left| \iint h_{ill}(x, y, 2z_m - z) h_{det}(x + x_p/M, y + y_p/M, z; z_p) dxdy \right|^2, \tag{4.2}$$

which is the overlap integral of the illumination PSF, $h_{ill}(.)$, set up by the laser, and the detection PSF, $h_{det}(.)$, associated with the pixel. M is the lateral magnification of the system and can be used in this way as a result of the lateral invariance of the PSF shape described earlier. Integration is carried out over a single plane, $z =$ const, and for the purposes of simplicity we choose to carry out the integration over the plane $z = 2z_m$. Using the Fourier transform relations derived in Appendix C, these PSFs can be re-expressed in terms of their equivalent pupil plane profiles:

$$h_{ill}(x, y, z) = \iint_{-\infty}^{\infty} P(m_1, n_1, z; 0) e^{-ik \sin\alpha (m_1 x + n_1 y)} \mathrm{d}m_1 \mathrm{d}n_1, \tag{4.3}$$

$$h_{det}(x, y, z; z_p) = \iint_{-\infty}^{\infty} P_2(m_2, n_2, z; z_p) e^{-ik \sin\alpha (m_2 x + n_2 y)} dm_2 dn_2, \tag{4.4}$$

where:

$$P(m, n, z; z_p) = \begin{cases} e^{i \frac{k z_p \sin^2\alpha}{2 M_a} \rho^2} e^{-ikz \sin\alpha \sqrt{cosec^2\alpha - \rho^2}}, & \rho \leq 1 \\ 0, & \rho > 1 \end{cases} \tag{4.5}$$

$m_{1,2}$ and $n_{1,2}$ are the normalized Cartesian co-ordinates in the pupil plane and integration is carried out over the unit circle. ρ is the radial co-ordinate in the pupil such that $\rho_{1,2} = \sqrt{m_{1,2}^2 + n_{1,2}^2}$ and M_a is the axial magnification of the system. $P_{1,2}(.)$

are pupil functions, containing the amplitude and phase information, which generate the PSFs in the focal region of the objective lens. Substituting these expressions into Eq. 4.2 and setting $z = 2z_m$ gives:

$$I(x_p, y_p, z_m; z_p) \propto \left| \iint \left\{ \iint P_1(m_1, n_1, 0; 0) e^{-ik \sin\alpha (m_1 x + n_1 y)} dm_1 dn_1 \right\} \times \left\{ \iint P_2(m_2, n_2, 2z_m; z_p) e^{-ik \sin\alpha [m_2(x + x_p/M) + n_2(y + y_p/M)]} dm_2 dn_2 \right\} dx dy \right|^2 , \tag{4.6}$$

which can be rearranged in the following way:

$$I(x_p, y_p, z_m; z_p) \propto \left| \iiiint \left\{ \iint e^{-ik \sin\alpha [x(m_1+m_2) + y(n_1+n_2)]} dx dy \right\} \times P_1(m_1, n_1, 0; 0) P_2(m_2, n_2, 2z_m; z_p) e^{-ik \sin\alpha [m_2(x_p/M) + n_2(y_p/M)]} dm_1 dn_1 dm_2 dn_2 \right|^2 . \tag{4.7}$$

The term in brackets can be recognized as being proportional to the product of two Dirac delta functions, $\delta(m_1 + m_2)\delta(n_1 + n_2)$, which enables us to perform the integrals in m_1, n_1:

$$I(x_p, y_p, z_m; z_p) \propto \left| \iint P_1(-m_2, -n_2, 0; 0) P_2(m_2, n_2, 2z_m; z_p) e^{-ik \sin\alpha [m_2(x_p/M) + n_2(y_p/M)]} dm_2 dn_2 \right|^2 . \tag{4.8}$$

For a perfect objective lens with no residual aberration $P_1(-m_2, -n_2, 0; 0) = 1$ at all points in the pupil plane and so does not affect this expression. Eq. 4.4 can then be used to show:

$$I(x_p, y_p, z_m; z_p) \propto \left| h_{det}(x_p/M, y_p/M, 2z_m; z_p) \right|^2 . \tag{4.9}$$

$h_{det}(.)$ is essentially the detection PSF for a pinhole located a distance z_p along the axis from the image plane. This expression shows that an image of $h_{det}(.)$ from the plane $z = 2z_m$ is projected directly onto the CCD camera with a magnification

of M. A full three dimensional measurement of $h_{det}(.)$ can therefore be made by recording a series of two dimensional images on the CCD camera at a number of closely spaced mirror positions z_m.

In this analysis, we have assumed that each pixel of the CCD camera can be treated as an independent pinhole. This is only the case, however, if the pixels are small enough or equivalently spaced closely enough to be able to sample at least twice the maximum spatial frequency component in the images. This is a result of the Whittaker-Shannon sampling theorem [25]. The highest spatial frequency component in the image, for this rotationally symmetric system, is $1/d = 1.22NA/\lambda M$ [35], where NA is the numerical aperture of the objective lens, λ is the illumination wavelength of the laser and M is the lateral magnification of the system. As a result, the inter-pixel spacing Δ must obey the following inequality:

$$\Delta \leq \frac{M\lambda}{2.44NA} \tag{4.10}$$

In the experiments we are about to report in the next section, $\lambda = 633nm$, $NA = 1.4$, $M = 53.3$ which requires the pixel spacing to be lower than $9.77\mu m$. The camera used had a value of $\Delta = 6.45\mu m$ so a full reconstruction of the data could be performed.

The experimental method described here to measure the detection PSF for the standard microscope architecture can equally be used to measure the detection PSF for the new architecture described in the previous chapter.

4.2 Experimental results

We began by measuring the detection PSF of the standard microscope architecture using the method described in the previous section. The diagram of the system used is reproduced in Fig. 4.3a. Specifically, an expanded beam from a helium neon laser

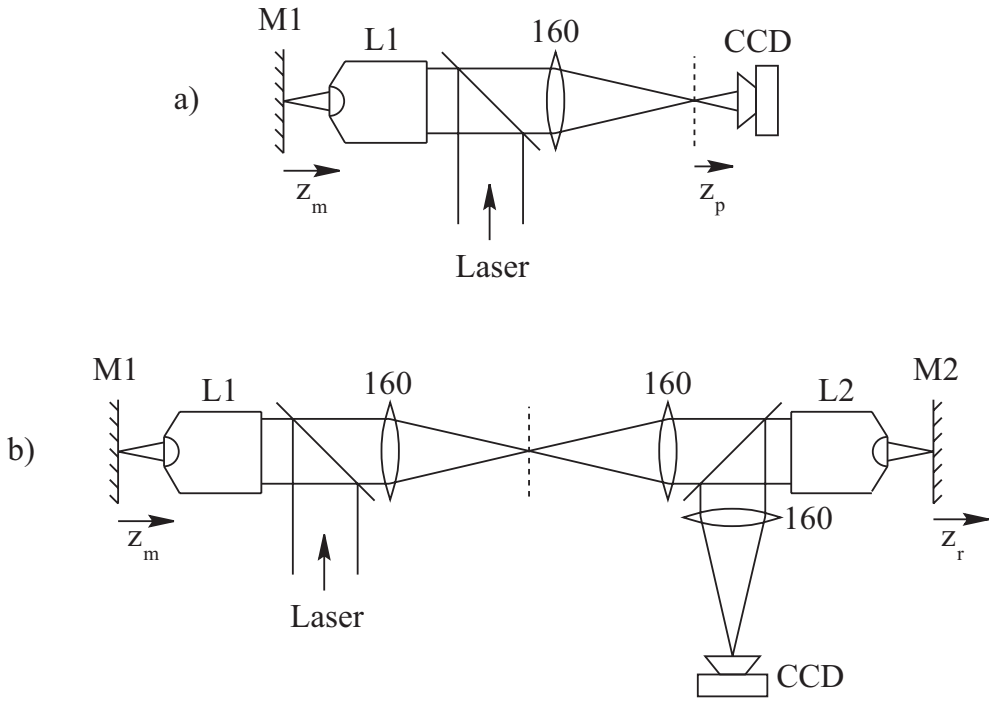

Figure 4.3: Systems used to measure detection PSFs. M1 and M2 are mirrors, L1 and L2 are a 1.4 NA 60x oil immersion objective and 0.95 NA 40x dry objective lens respectively. The numbers shown are the focal lengths of the lenses in mm.

(wavelength 633nm) was used for illumination, L1 was an Olympus 1.4 NA 60x oil immersion objective and the tube lens was an achromatic doublet with focal length 160mm. Images were acquired on a low noise, peltier cooled, CCD camera with 1344 x 1024 pixels (*ORCA-ER*, Hamamatsu, Japan) and its axial position, z_p, could be changed. For each position of the CCD camera, a sequence of images was acquired for a range of z_m values. PSFs for five different positions of the CCD camera were taken $[z_p(mm) = -20, -10, 0, 10, 20]$ and computer reconstructions of the intensity profile in the meridional plane are shown in Fig. 4.4a. All PSFs are presented on the same plot scaled back down to reflect their true size in object space. Three of the PSFs have been enlarged so that the distortions due to spherical aberration can be seen more clearly. There is an elongation of the PSF along the axial direction. The intensity for each PSF has been re-normalized to the maximum pixel value in order that the out-of-focus images can be seen clearly (the maximum pixel intensity

of the aberrated PSFs was approximately half that of the unaberrated case for the enlarged images).

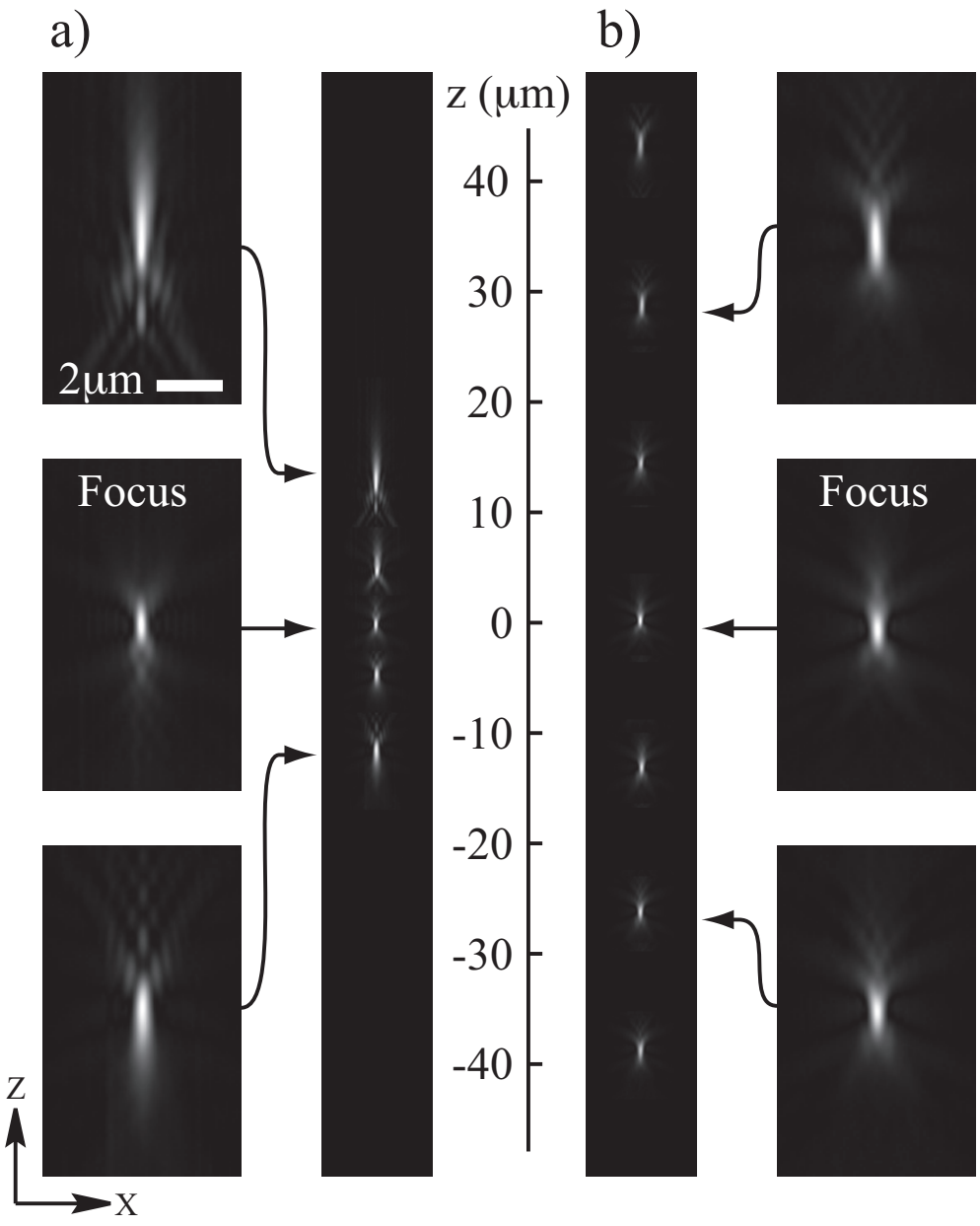

Figure 4.4: Detection PSFs measured with the systems in Fig.4.3.

The second set of measurements were made using the configuration of Fig. 4.3b. M1 was illuminated in the same way as before and the reflected light passed back

through L1 and the first tube lens before passing through a second identical tube lens. The light then entered objective L2, which was an Olympus 0.95 NA 40x dry objective. A dry lens was chosen to ensure that there was no mechanical interference between the reference mirror and the objective via an immersion medium. The light reflected off the reference mirror positioned at z_r, re-entered L2 and was reflected by the beam splitter. Another tube lens focused the light onto the CCD camera which was fixed in the nominal focal plane of the final microscope stage. For each position z_r of the reference mirror, a sequence of images was acquired for a range of object mirror positions z_m. Fig. 4.4b shows the measured PSFs for seven different positions of the reference mirror $[z_r(\mu m) = -30, -20, -10, 0, 10, 20, 30]$. It can be seen that the overall shape of the PSF was retained over a large range of depths in object space, indicating that no significant aberrations were introduced. This can be seen clearly in the three PSFs that have been enlarged. Note that no intensity renormalization was performed for these three images. We also measured the maximum intensity value present in each focal spot, which is proportional to the Strehl ratio, and this was found to be roughly constant over a range of $\pm 35\mu m$ in object space. In chapter 3, we have shown theoretically that we expect to achieve twice this value and we suggest that the reason for this is that the lens design has been optimized for a larger lateral field of view and therefore does not strictly conform to the sine condition. As a result the axial response is slightly compromised as seen here. It might therefore be possible to optimize the design of such lenses further to achieve even larger axial ranges to be achieved with this system.

4.3 Conclusions

In this chapter we have presented PSF measurements from two different microscope architectures where refocusing was carried out remotely. The first system was a standard microscope configuration which was refocused by moving the detection

pinhole along the axis from the image plane. The effects of spherical aberration were clearly seen in the the PSFs measured which demonstrated that this is a particularly poor way of refocusing. The equivalent set of PSFs were also measured for the new refocusing architecture proposed in chapter 3 and showed that a considerable improvement could be gained in comparison to the first system. In this case, the PSF can be scanned over a large range of specimen depths without visibly losing its form which demonstrates that this approach is particularly effective.

Although strictly speaking the distributions measured here were detection PSFs, it is also possible to interpret them as illumination PSFs due to the reciprocal nature of confocal systems (see Appendix B). The overall confocal system PSF, which is usually found by multiplying the illumination and detection PSFs together, can therefore be found by simply squaring the results shown in Fig. 4.4.

It is also worth mentioning that the results here demonstrate that the working distance of a high NA objective lens can be extended using this system. This could be particularly important for imaging of thick specimens where it is not possible to reach the depths required because the working distance of the objective lens is not large enough.

Chapter 5

Applications of remote focusing in sectioning microscopy

In this chapter, four novel imaging systems are presented that were built to demonstrate the ability of the microscope architecture described in chapter 3 of this thesis. This architecture enabled each system to be refocused remotely in order to image information from different depths in the specimen. The images acquired were free from systematic aberrations and the specimens were not disturbed mechanically during the imaging process.

5.1 Practical implementation of remote focusing

Before considering the specific details of each microscope system built, we first make some general comments about the fundamental building block that permits refocusing to be carried out remotely.

Fig. 5.1a shows the standard architecture of most commercial microscope systems. This consists of a high NA objective lens (L1), obeying the sine condition, and a low NA tube lens. It has already been shown in chapter 3 that a diffraction limited image of points lying in the focal plane appears in the image plane of L1.

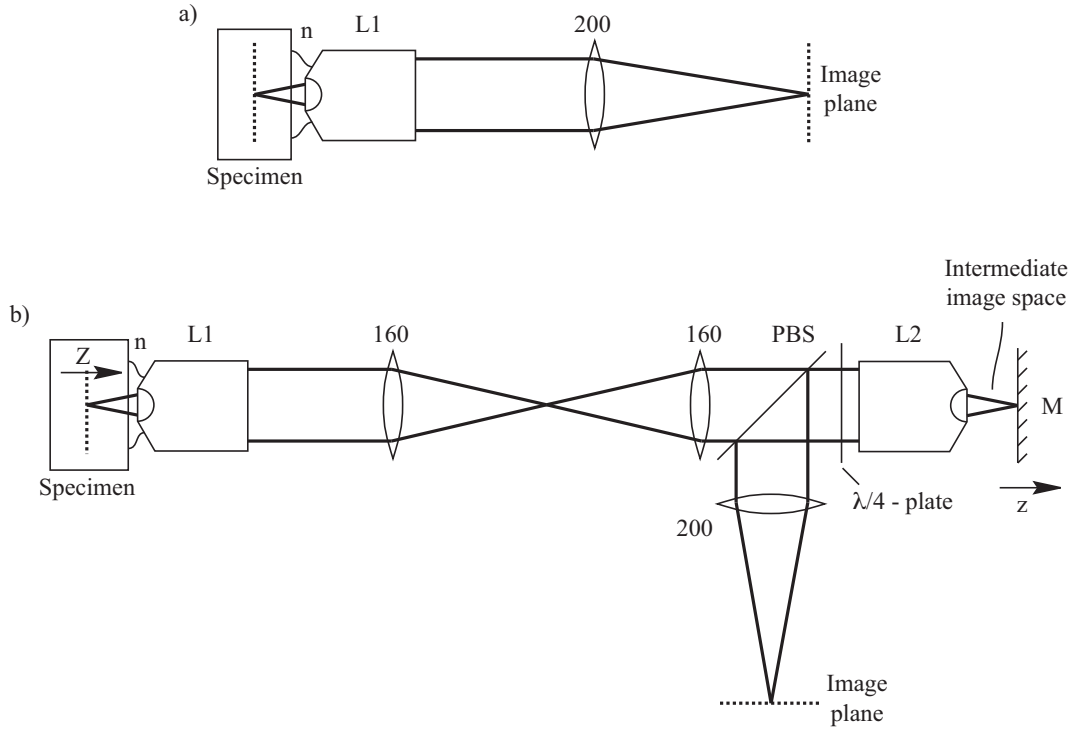

Figure 5.1: a) A standard microscope system and b) the replacement architecture used as a fundamental building block of all systems in this chapter.

Furthermore, it has also been shown that this pair of conjugate planes is unique in delivering aberration-free performance. For the specific case where L1 is an Olympus 1.4NA 60× oil immersion lens and the tube lens has focal length 200mm, this system produces a lateral magnification of $60 \times \frac{200}{180} = 66.7\times$ because Olympus objectives are generally designed to operate with a tube lens of focal length 180mm. The immersion oil for this lens has a refractive index $n = 1.52$. It is noted that some commercial objective lenses are designed to work in conjunction with a specific tube lens whereby correction of certain aberrations is carried out by the two lenses working as a pair. This is not an issue in the current situation, however, because Olympus objectives perform all corrections internally and therefore an achromatic doublet with any focal length can be used as the tube lens.

The microscope systems described in this chapter, however, were all based on the new architecture shown in Fig. 5.1b. This comprises two high NA objective lenses,

three achromatic doublet lenses, a mirror (M), a polarising beam splitter (PBS) and a quarter-wave plate ($\lambda/4$-plate). In all cases, L1 and L2 were an Olympus 1.4 NA 60X oil immersion lens and an Olympus 0.95 NA 40X dry lens respectively. Their pupil planes were mapped together with a 4f imaging system, consisting of two 160mm focal length lenses, which produced a magnification of unity. This magnification was chosen deliberately to allow perfect three dimensional imaging of the specimen in the intermediate image space in accordance with Eq. 3.16:

$$M = \frac{\sin\alpha_1}{\sin\alpha_2} = \frac{NA_1/n}{NA_2} = \frac{1.4/1.52}{0.95} \approx 1. \tag{5.1}$$

When the mirror is placed in the focal plane of L2, a diffraction limited image of points lying in the focal plane of L1 in the specimen appears at the image plane. The key difference in this system, however, is that points lying in other specimen planes, besides the focal plane, can also be mapped onto this image plane, without aberration, by shifting the mirror axially in the focal region of L2. Moving the mirror a distance z shifts the effective focal plane in the specimen axially by a distance $Z = 2z/n$, where n is the refractive index of the oil used as the immersion medium of L1. The lateral magnification is set by the combination of L1 and the 200mm doublet and hence retains its former value of 66.7×. A coverglass of thickness 170μm was mounted onto the mirror to compensate for coverglass corrections introduced by objective L2. A thin layer of oil was introduced between the mirror and coverglass to ensure good optical contact between these elements to minimize extraneous reflections that would otherwise result as the light passes between regions of different refractive index.

It is an interesting point to note that the resolution of this system is not restricted by L2 even though it has the lower NA of the two objective lenses used in this system. This can be understood in terms of geometric considerations. In Eq. 3.2 (Pg. 46), we saw that the rays from object space are mapped onto conjugate rays with the

same angle in the intermediate image space. As such, the limiting *angular aperture* in the system, γ_{max}, will essentially limit the overall resolution of the instrument. This implies that as long as the second objective has a higher *angular aperture* than the first it will not restrict the resolution. This situation is realized when using a 1.4NA oil immersion lens and a 0.95NA dry lens as L1 and L2 respectively. The numerical aperture of the instrument in this case therefore has a value of 1.4.

This result can also be understood from another simple argument. Consider two independent point sources placed in the focal plane of L1, separated by a distance such that they can just be resolved in the conventional image plane of this lens. Using the Abbe resolution criterion, defined in Eq. 1.1, this distance can be calculated as $d_1 = \lambda/2NA_1$, where λ is the emission wavelength of the sources. In the current arrangement, these sources are re-imaged in the focal plane of L2, separated by a distance $d' = n\lambda/2NA_1$, where a factor n has been included to account for the magnification introduced between the object space and intermediate image space, defined by Eq. 3.1. It turns out, for the lens parameters used here, that this separation is still large enough to be resolved by L2 whose minimum resolvable separation is $d_2 = \lambda/2NA_2$, i.e.:

$$d' > d_2 \tag{5.2}$$

$$\frac{n\lambda}{2NA_1} > \frac{\lambda}{2NA_2} \tag{5.3}$$

$$1.09\lambda > 1.05\lambda, \tag{5.4}$$

and hence L2 does not place a restriction on the resolving power of the system.

The role of the PBS and $\lambda/4$-plate can be understood with reference to Fig. 5.2. Here, unpolarized light originating from the specimen is split by the PBS into two orthogonally polarized beams with equal intensity, the horizontal component being reflected and the vertical component being transmitted. The vertical component then propagates through the $\lambda/4$-plate, with its fast axis oriented at 45° to the plane

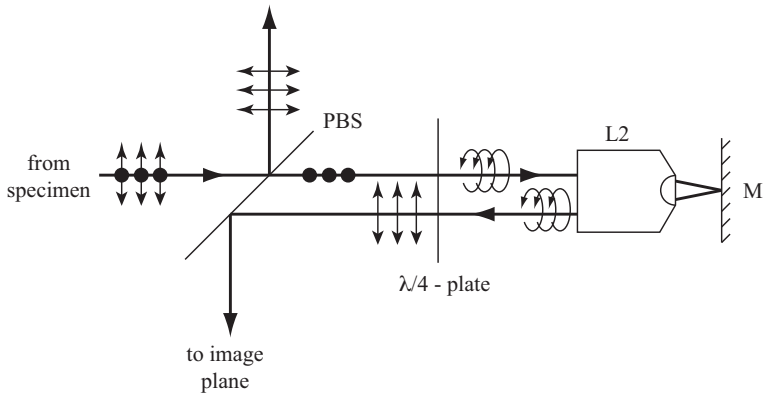

Figure 5.2: The role of the polarizing beam splitter (PBS) and $\lambda/4$-plate

of polarization, and is transformed into circularly polarized light before entering the objective lens. Reflection from the mirror surface reverses the sense of polarization so that when it propagates back through the objective and $\lambda/4$-plate it emerges with horizontal polarization. This is then completely reflected by the PBS towards the image plane. In this way, 50 % of the fluorescence light arrives at the image plane compared with the case of a standard beamsplitter where only 25 % arrives. It is also worth noting that, due to the reciprocal nature of this configuration, the full intensity of a polarized laser beam can be transmitted from the image plane towards the specimen, provided that its polarization is along the horizontal direction.

In all experiments the system in Fig. 5.1b constitutes the fundamental building block around which specialized illumination and detection optics are constructed to obtain optically sectioned images from the effective focal plane. The same lens parameters were used for this part of the system in each case.

5.2 Nipkow disc confocal microscope

As mentioned in the introduction chapter on Pg.17, a useful method of acquiring sectioned image data from a single specimen plane is to employ a Nipkow disc confocal microscope. Three dimensional image data can then be acquired by changing

the focal setting of the system a number of times and acquiring images from different specimen depths. In this section, we demonstrate the application of a Nipkow disc to the new microscope architecture experimentally and show that different specimen planes can be imaged without physically changing the distance between the specimen and objective lens. For the purposes of comparison, we also show how these results compare with two other methods of refocusing.

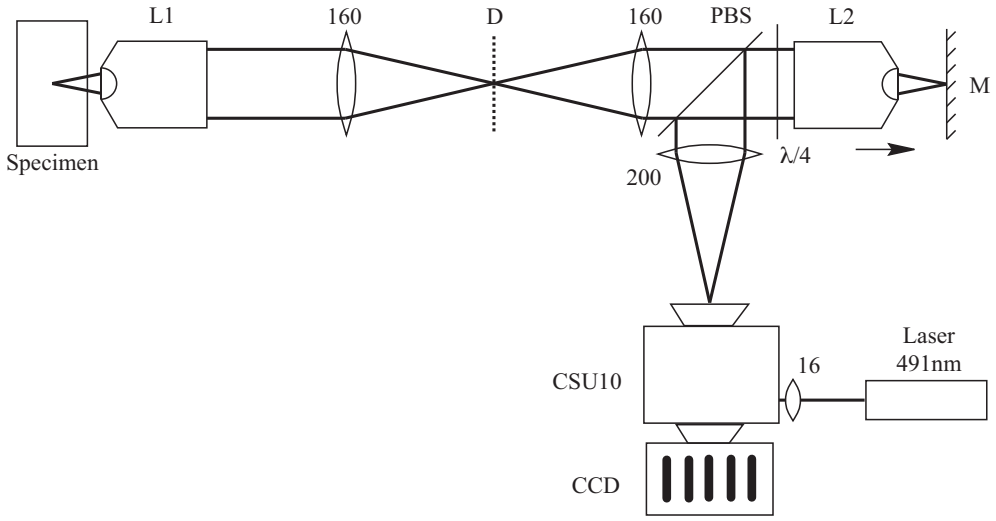

Figure 5.3: Fluorescence confocal imaging system using a Nipkow disc. Refocusing is performed by shifting the reference mirror $M1$ axially.

A schematic diagram of the system built for these experiments is shown in Fig. 5.3. A Nipkow disc scanning unit (CSU10, Yokogawa, Japan) was used to acquire widefield confocal fluorescence images directly on a CCD camera. The pinhole array was placed in the image plane of the microscope. Illumination was provided by a diode pumped solid state laser (*Calypso*, Colbolt, Sweden) with a maximum available power of 50mW and wavelength of 491nm. The power and polarization of this laser could be adjusted externally with a neutral density filter set and a $\lambda/2$-plate respectively. A short focal length lens, with $f = 16$mm, was used to focus the laser light at the entrance aperture of the scanning unit so that the whole field of view in the specimen was illuminated. A dichroic beamsplitter with a cutoff wavelength of

493 nm and emission filter with a bandpass of 500-550nm were already embedded in the CSU10 for fluorescence imaging. Images were acquired with a low noise, peltier cooled, CCD camera having 1344 x 1024 pixels (*ORCA-ER*, Hamamatsu, Japan). Each pixel of the camera was square in profile and measured 6.45μm in width. L2 was mounted on a high precision scanning stage (P-721.CLQ, PI Instruments, Karlsruhe) so that its position along the axis could be controlled over a range of 100μm at a resolution of 0.1μm. Previously, we have spoken about moving the mirror (M) in order to refocus the system to image different planes of the specimen, however, in this case L2 was moved instead which is completely to shifting the reference mirror along the axis. The specimen was also mounted on a high precision scanning stage (P-611.3S NanoCube, PI Instruments, Karlsruhe), which also provided a scanning range of 100μm along the axial direction.

Three stacks of images were recorded from the same region of a mouse kidney section (FluoCells prepared slide #3, stained with Alexa Fluor 488, from Molecular Probes, Invitrogen). For the first stack, the mirror was positioned in the focal plane of L2 and successive images were acquired by physically moving the specimen to different axial positions in steps of 0.5μm. As L2 played no role in the focusing process, this was optically equivalent to the standard focusing technique used in confocal microscopy, where the imaging plane is held fixed and the specimen is moved along the axis to image different planes. Two sectioned images from specimen planes separated axially by 15μm are presented in Fig. 5.4 (1a) and (1b), as well as the computer generated reconstruction of a single XZ plane through the stack (1c). The fine detail of the specimen structure at all depths in the XZ image is a clear indication that image resolution has been maintained at all specimen depths during image acquisition.

For the second stack, L2 was replaced by a low NA 100mm focal length achromatic doublet. The mirror M was placed in the focal position of this lens and scanned in steps of 0.2mm towards it, using a manual stage. This was optically

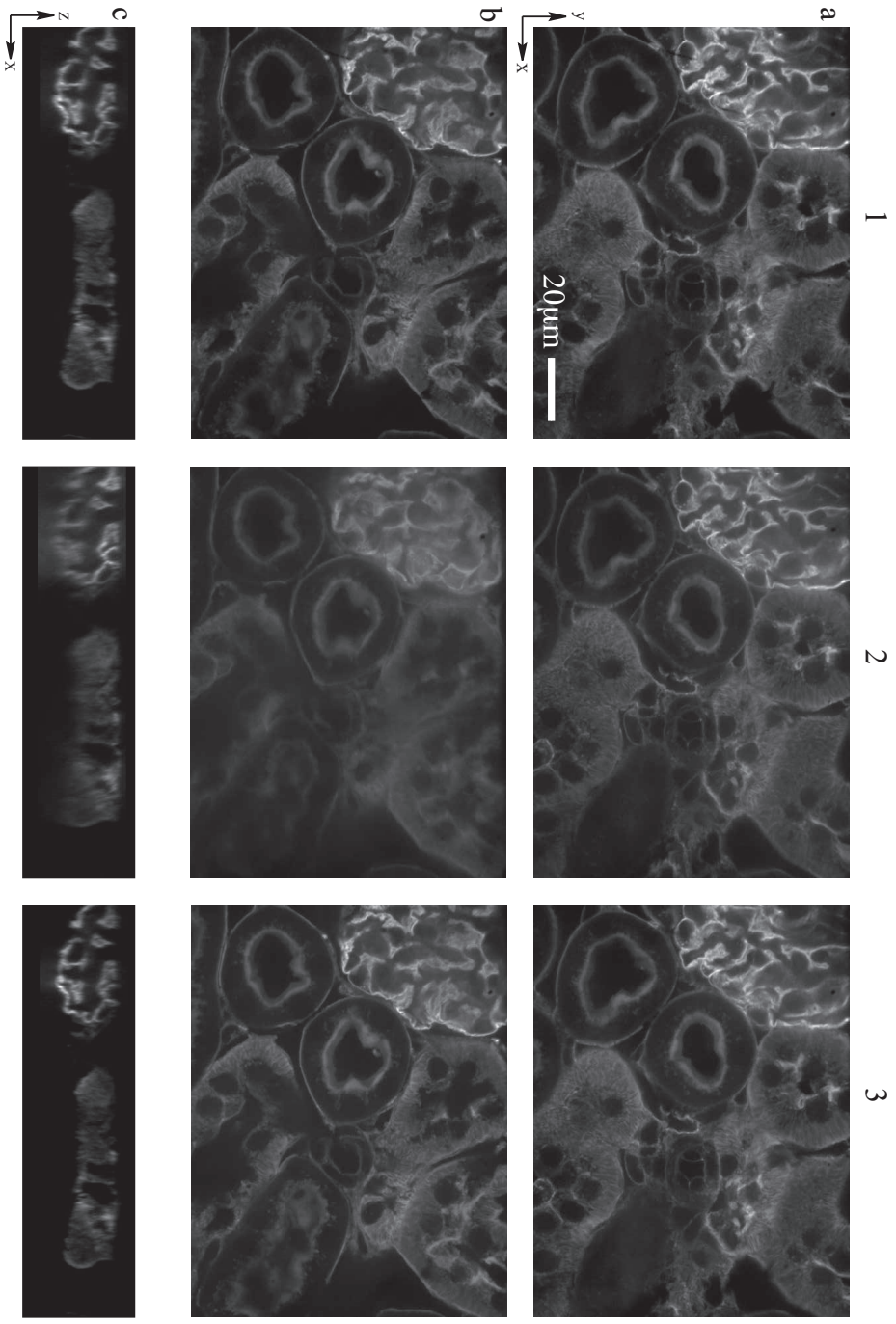

Figure 5.4: Fluorescence confocal sections of a mouse kidney specimen acquired with a widefield confocal imaging system. a) Refocusing was performed by shifting the specimen in the focus of L1. b) Refocusing was performed using the low NA system, equivalent to shifting the scanning unit. c) Refocusing was performed by shifting the reference mirror in the focus of L2.

equivalent to placing the CSU10 pinhole array at the detector plane D and moving it towards the tube lens to image deeper planes in the sample, separated by $0.5\mu m$. Fig. 5.4 (2) shows the same three image planes as before for this second set of data. Image (2a) corresponds to the case where the CSU10 images the focal plane and hence the result is comparable to image (1a). Image (2b) corresponds to the case where the CSU10 images the same deeper plane in the specimen and the significant blurring, compared with the result of image (1b), is a clear indication of the presence of spherical aberration. Finally the XZ image (2c) shows the progressive degradation of image resolution when focusing to deeper regions of the specimen where the fine details become washed out in comparison to image (1c).

The third stack was taken using the new focusing technique. The specimen was held stationary and the reference mirror was scanned in steps of 0.38μm along the optical axis towards L2, in order to select deeper planes in the sample, each separated by $0.5\mu m$. The results in Fig.5.4 (3), from the three example planes in the stack, demonstrate that the imaging resolution has been maintained at all sample depths and compare favourably to the results in (1). This, of course, is no surprise as we have already shown in the previous chapter that this system can be refocused over a far greater range than this without introducing significant aberration.

5.2.1 Extended depth of field microscopy

As we have seen in the introduction chapter on Pg.11, one possible way of displaying the three dimensional image data obtained with the remote focusing technique would be to sum the individual images acquired at different focal settings together computationally to produce an *extended depth of field* image. This process is equivalent to projecting all the data along the axial direction onto one plane so that the resulting image displays information from a whole range of specimen depths simultaneously. Such images could, however, be produced on the CCD camera directly by integrat-

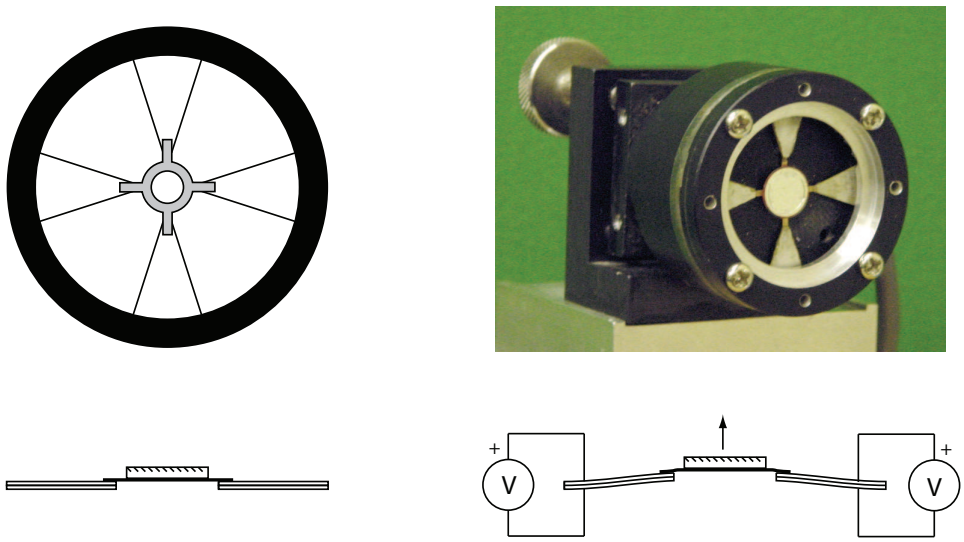

Figure 5.5: The piezo-ceramic bimorph mirror actuator used in these experiments.

ing the response while scanning the effective focal plane over a range of specimen depths. An extended depth of field image would then be captured in a single frame without needing to perform any post processing on a computer. Furthermore, a real-time extended depth of field movie could also be generated by acquiring a series of such images at closely spaced time intervals.

The setup of Fig. 5.3 was employed for this experiment however a new actuator device was used to scan the effective focal plane in the specimen at high speed. This is shown in Fig. 5.5 and was developed by Photometric Consultants Ltd. (Surrey, UK). This consisted of a small flat mirror, with diameter $9mm$, mounted between four independent cantilevers arranged in a cruciform shape. Each cantilever was manufactured from a piezo-ceramic bimorph material and could be made to flex by applying a voltage between the top and bottom surfaces. Driving the cantilevers together with the same voltage waveform caused them to flex in synchrony and hence displace the mirror along the optical axis of the system. This mode of operation exhibited a linear response for amplitudes of $\pm 125\mu$m up to frequencies of 1 kHz.

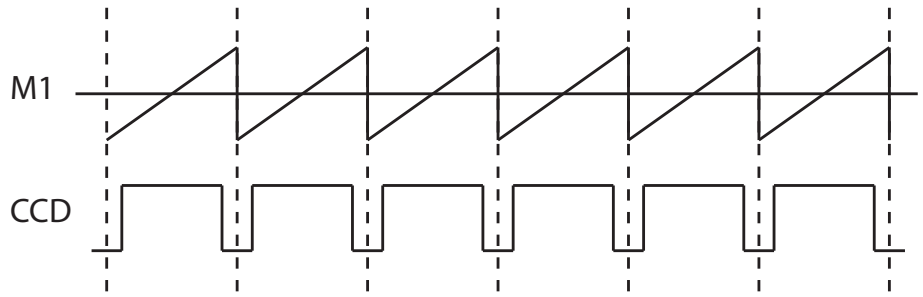

Figure 5.6: The voltage waveforms used to drive the axial movements of the mirror and CCD camera integration for extended depth of focus imaging.

Custom built *Labview* software was written to acquire image data from the CCD camera via the IEEE 1394 interface (a.k.a. the firewire interface). In addition to this, the software also generated the two voltage waveforms, shown in Fig. 5.6, to control the axial position of the mirror as well as the integration period of the CCD camera. These voltages were generated with a DaqBoard/2001 PCI card from IOtech (Cleveland, USA). The period of these waveforms was set to 12Hz as this was the maximum permissible transfer rate that the CCD camera would allow. Movies were recorded directly in **.avi* format. The mirror was swept so as to probe specimen depths over a range of 20μm and a number of movies were recorded of

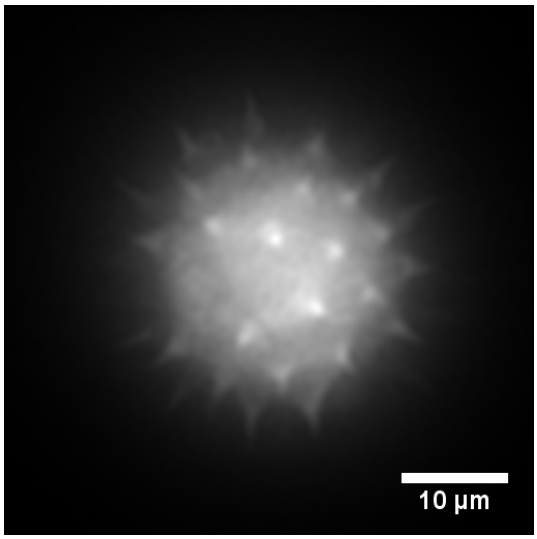

Figure 5.7: Extended depth of field image

various fluorescent specimens. An example frame from one of many movies taken of pollen grains is shown in Fig. 5.7 and compares with the result shown on Pg. 11.

The frame rate of this system was essentially limited by the CCD camera because it could only acquire images at 12 fps. Frame rates of 100Hz and possibly higher are achievable with a faster CCD camera as the mirror actuator could support these speeds.

5.2.2 Stereo imaging

Previously in this thesis, we have noted that two extended depth of field images acquired from different angles of perspective can be used to form a stereo pair. A simple modification to the experimental setup of the previous section was performed to enable the angle of perspective to be changed in the extended depth of field images so as to permit high resolution stereo pairs to be acquired in quick succession. The modified system is shown in Fig. 5.8. The only difference is that an extra piezo-driven steering mirror $M2$ (S-325, PI Instruments, Karlsruhe) was placed close to the pupil plane of L1. This was used to tilt the wavefronts entering and leaving L1.

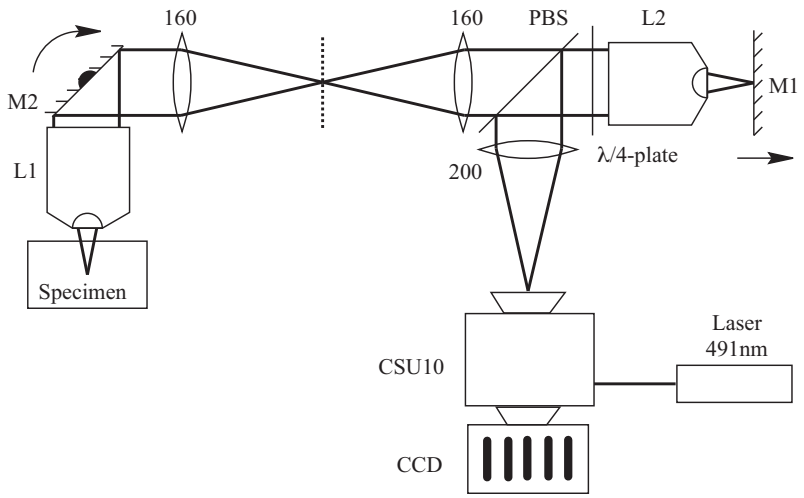

Figure 5.8: Stereo imaging

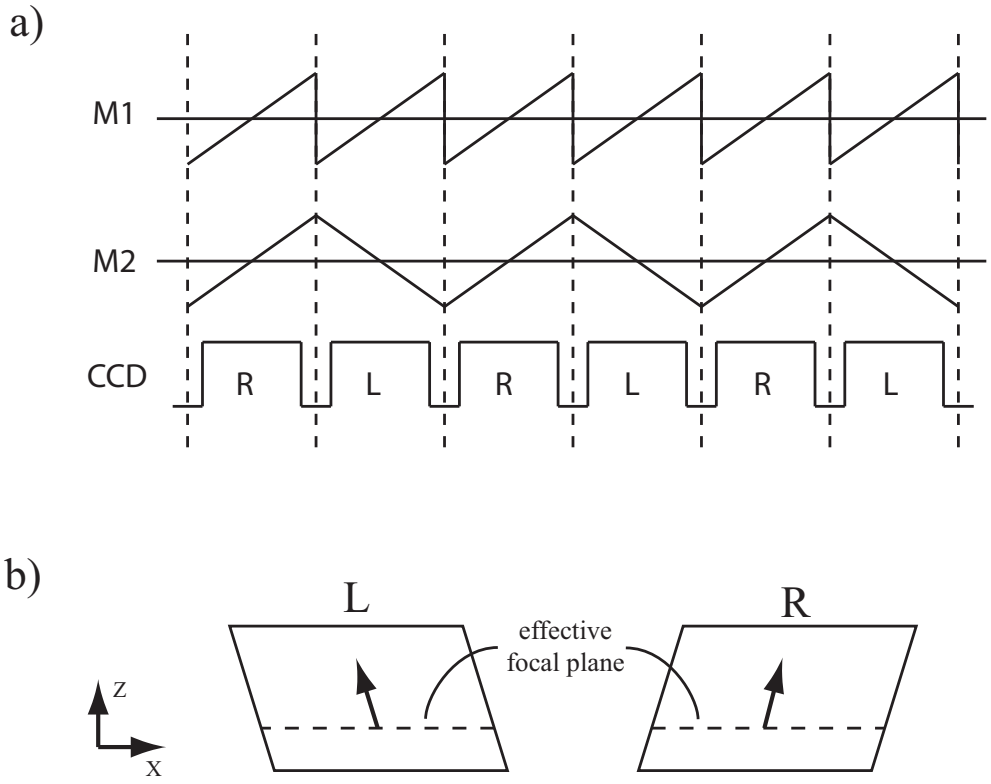

Figure 5.9: a) Voltage waveforms used to translate mirror M1 along the axis, rotate mirror M2 and control CCD integration for stereo imaging. b) The resulting trajectory of the field of view in the specimen during stereo imaging.

Fig. 5.9a shows the waveforms used to control the two mirrors and the CCD integration period. As before, M1 was scanned along the optical axis while integrating the response on the CCD camera to produce an extended depth of field image of the specimen. At each point during the scan, however, the CCD camera instantaneously records information from a uniquely defined area in the specimen. This field of view, which is located in the effective focal plane of the microscope, can be shifted laterally by tilting mirror M2. The waveform driving M2 therefore causes the field of view to follow one of the trajectories shown in Fig. 5.9b during an image scan. As a result, the CCD camera sums up the information along a skewed direction and the extended depth of field image appears to have a different perspective. In the following scan the complementary trajectory is used to produce a second image from a complementary viewing perspective. These two images then form a stereo

pair from a single time point. The separation between the angles of perspective in the two images can be adjusted by changing the amplitude of the waveform driving M2. An angle of about 12° was used in these experiments.

Pairs of images were then acquired in quick succession from the two different angles of perspective to produce high resolution stereo movies of fluorescent specimens in real-time. A number of movies were recorded using this system. As two images are required for each time point, the frame rate of these movies was limited to 6 fps because the CCD camera could only acquire images at a maximum rate of 12 fps. An example of a single stereo pair from one of the movies is shown in Fig. 5.10.

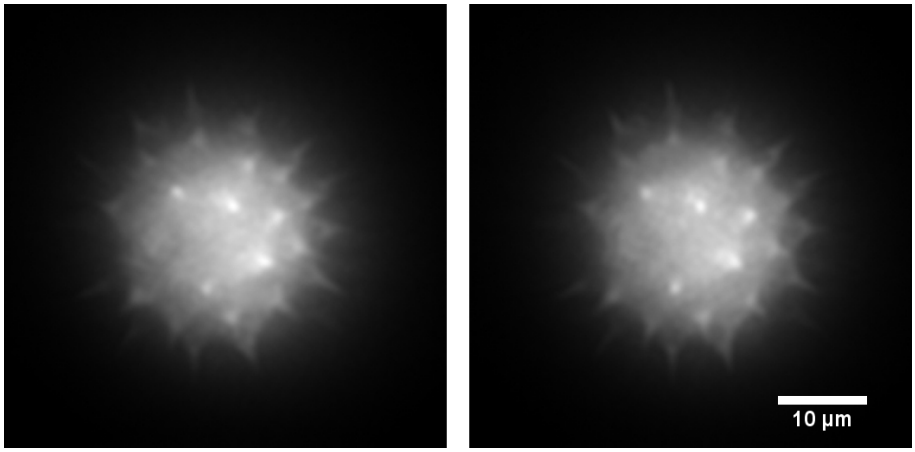

Figure 5.10: An example of a stereo pair of images.

A particularly elegant method for displaying these movies would be to use a stereo monitor, an example of which is the Mebius RD3D (Sharp Corporation, Japan). These monitors essentially overlay the different images of each stereo pair at the same location on the screen and introduce an angular separation between them so that the observer sees a different image with each eye. As a result, the stereo effect can be observed directly by the user without any extra visual aids. Movies can also be viewed on these monitors by displaying the stereo pair from different time points in series.

The experimental system described here could potentially be developed further

to enable stereo images to be displayed directly on such a stereo monitor. In this way, the user could observe a stereo image of the specimen live on the screen.

5.3 Slit scanning microscopy

The second imaging system built was based on a slit scanning confocal fluorescence microscope (see Pg. 1.14). This system permitted high resolution two-dimensional images of the meridional plane in the specimen to be acquired at high speed as opposed to the commonly imaged focal plane.

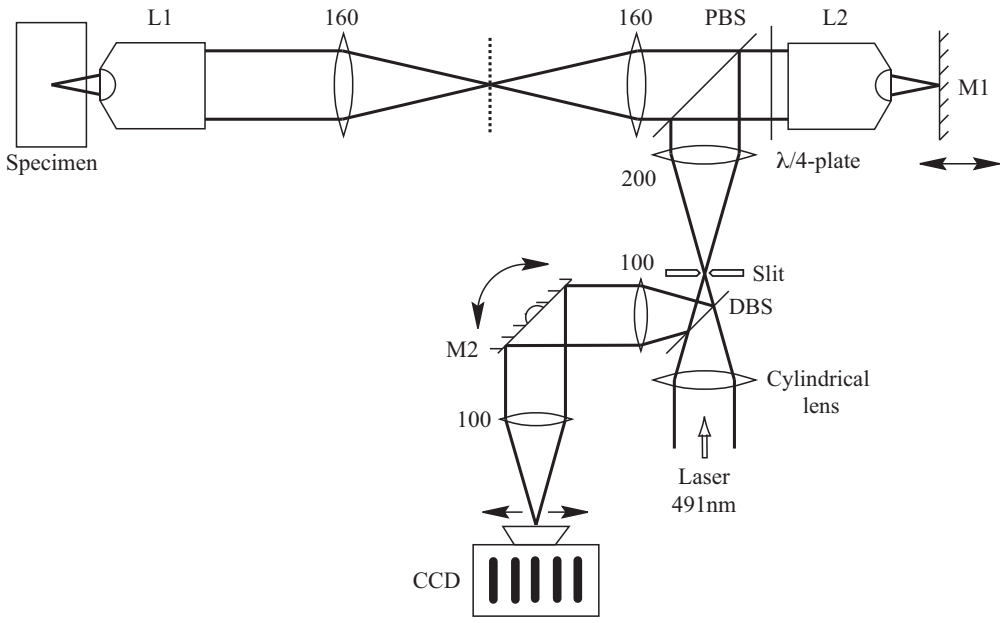

Figure 5.11: Slit scanning microscope

A schematic diagram of the system constructed is shown in Fig. 5.11. A slit, of width 10μm and length 10mm from Comar (UK), was placed in the image plane of the microscope. Once again, illumination was provided by a diode pumped solid state laser (*Calypso*, Colbolt, Sweden) with a maximum available power of 50mW and wavelength of 491nm. This was expanded with a telescope arrangement and focused onto the slit using a cylindrical lens of focal length 100 mm. The light

transmitted by the slit was imaged into the specimen to form a diffraction limited line of light. Fluorescent molecules in the illumination path were excited and the subsequent emissions propagated back through the system and were imaged back onto the slit. This selectively passed fluorescence light originating from the linear focal region of the illumination pattern in the specimen and rejected emissions from other regions. This was then re-imaged onto a narrow column of pixels on the CCD camera using a 4f imaging system with unit magnification. A dichroic beamsplitter with a cutoff wavelength of 493 nm and emission filter with a bandpass of 500-550nm were also used to remove extraneous illumination light in the system prior to imaging. In this way, an entire line of points in the effective focal plane of the microscope could be imaged simultaneously. Furthermore, this line could be refocused to different specimen depths by moving mirror $M1$ axially. The same piezo-ceramic bimorph mirror was used as in section 5.2.1.

A galvanometer mirror (VM1000, GSI Lumonics, USA), $M2$, was mounted in the intermediate plane of the 4f system and could be tilted to shift the image of the slit laterally on the CCD camera. As a result, it was possible to image line information from different specimen depths onto columns of pixels at different lateral positions on the CCD camera. Integrating the response on the CCD camera while scanning in depth therefore gave rise to an XZ image of the specimen directly. The same CCD camera was used as in the previous experiment with a frame rate of 12 fps.

Custom built *Labview* software was written to acquire image data from the CCD camera and to control the positions of the two mirrors. The waveforms used are shown in Fig. 5.12. A number of movies were acquired from some of the other pollen grains in the commercial sample (Carolina w.m. 30- 4264 (B690)) and these were saved in *.avi format. Two example frames from these movies are shown in Fig. 5.13. As can be seen from these the image resolution is clearly maintained over all depths in the specimen.

We note that the vertical line in the middle of these images is probably the

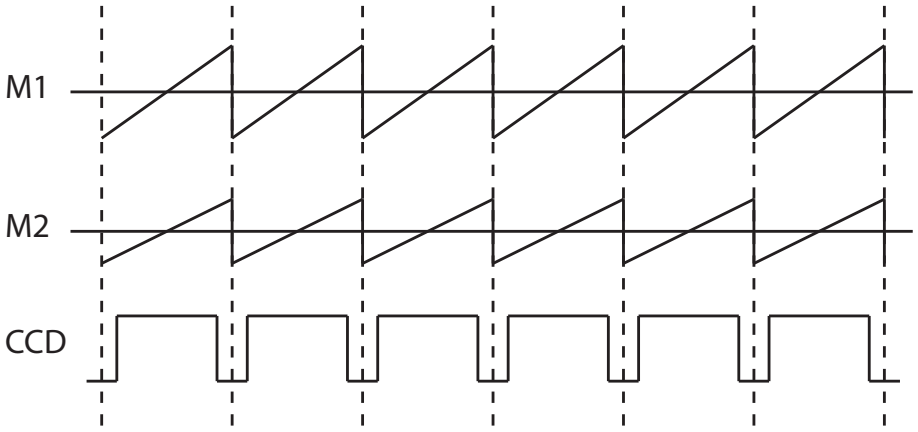

Figure 5.12: Voltage waveforms used to translate mirror M1 along the axis and rotate mirror M2 so as to image the slit onto different lateral columns of pixels on the CCD. The CCD integration control is also shown.

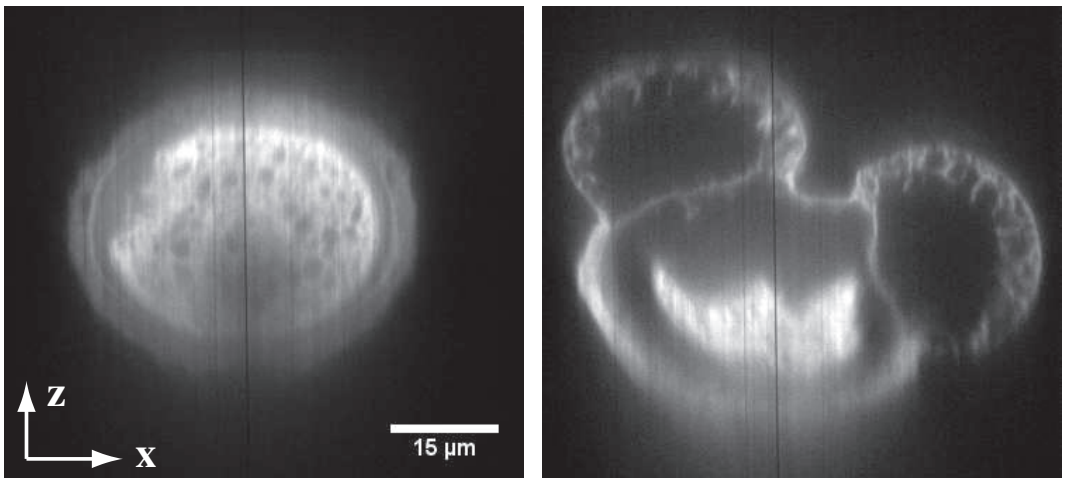

Figure 5.13: Two example images of fluorescent pollen grains obtained with the slit scanning microscope. The vertical line in the middle of the images is an artifact introduced by an imperfection in the slit which is bridged at this one point.

result of a piece of dust, which has blocked one particular point on the slit. During scanning, this point then produces a blank line in the middle of the image.

5.4 Structured illumination microscopy

The third experimental system built was based on a structured illumination microscope. This technique permits optically sectioned images of the specimen to be

acquired using conventional light sources [41, 42, 43].

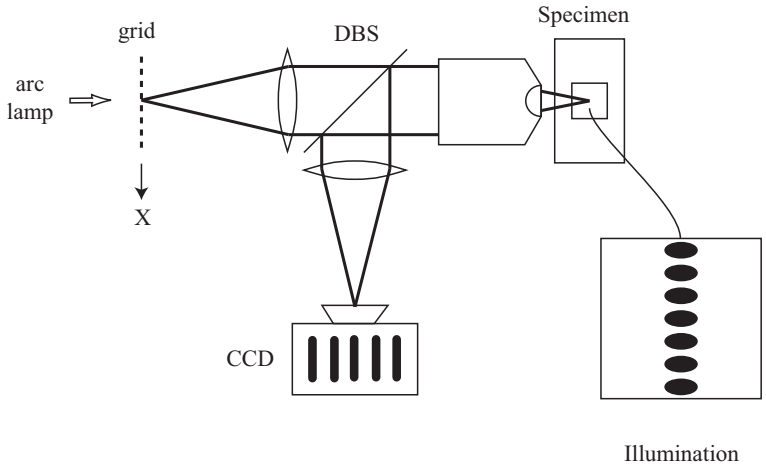

Figure 5.14: The principle of structured illumination

One particularly elegant approach is shown in Fig. 5.14 and involves placing a grid structure in the image plane of a conventional microscope and illuminating it with an arc lamp source. The intensity distribution then produced in the specimen has a spatial modulation in the lateral direction that peaks in the focal plane and falls off rapidly out-of-focus, as shown in the figure inset. Fluorescence light generated by the molecules in the specimen is then separated out with a dichroic beamsplitter (DBS) and recorded on a CCD camera. As in conventional microscopy, the result consists of a superposition of blurred contributions from out-of-focus and a contribution from the focal plane, which is inscribed with the modulation pattern. Recovery of the sectioned image follows by identifying the parts of the image affected by the modulation. A simple way to do this is to acquire three separate images of the specimen, I_1, I_2 and I_3, with the grid located in different positions along the X axis, offset by a third of a grid spacing. The following simple equations can then be used to recover both conventional and confocal images of the specimen [43]:

$$I_{conv} = I_1 + I_2 + I_3 \tag{5.5}$$

$$I_{conf} = \frac{\sqrt{2}}{3}\sqrt{(I_1 - I_2)^2 + (I_2 - I_3)^2 + (I_3 - I_1)^2}. \tag{5.6}$$

Three dimensional image stacks are acquired by repeating this procedure at a number of different focal settings.

Care must be taken when selecting the spatial frequency of the grid, however, to ensure that good quality sectioned images are obtained using this technique. For this, it is convenient to define a normalized grid frequency $\Lambda = \frac{\lambda}{d(NA)}$, where λ is the illumination wavelength, NA is the numerical aperture of the objective lens and d is the period of the grid pattern set up in the specimen [43, 44]. For thick fluorescent specimens, a grid frequency of $\Lambda = 1/3$ is often considered to give the optimum results and this value is used by commercial products such as Optigrid (Thales, UK) and Apotome (Zeiss, Germany).

In commercial structured illumination systems refocusing to image different specimen planes is often done by physically changing the distance between the objective lens and the specimen. The experiment built here therefore demonstrates that the technique of structured illumination can be applied to the new microscope architecture to obtain sectioned images from different specimen planes through remote focusing.

A schematic of the system constructed is shown in Fig. 5.15. Refocusing is carried out in the same way as in previous experiments by displacing the mirror M1 along the optical axis. The delivery fibre from a conventional arc lamp source (X-Cite 120, Exfo, USA) was imaged onto the grid with a 4f system of lenses. A magnification of 2.5x was introduced to ensure a large field of view would be illuminated in the specimen. infra-red and excitation filters were also placed in the intermediate plane of this 4f system to produce an illumination spectrum of 432-482 nm.

A commercial grid system (Optigrid, Thales, UK) was used in these experiments. This consisted of a transmission grid, with a line spacing of 25μm and equal mark-to-space ratio, mounted on a piezo translation stage driven by an electronic control unit. The position of the grid could therefore be controlled by applying an external

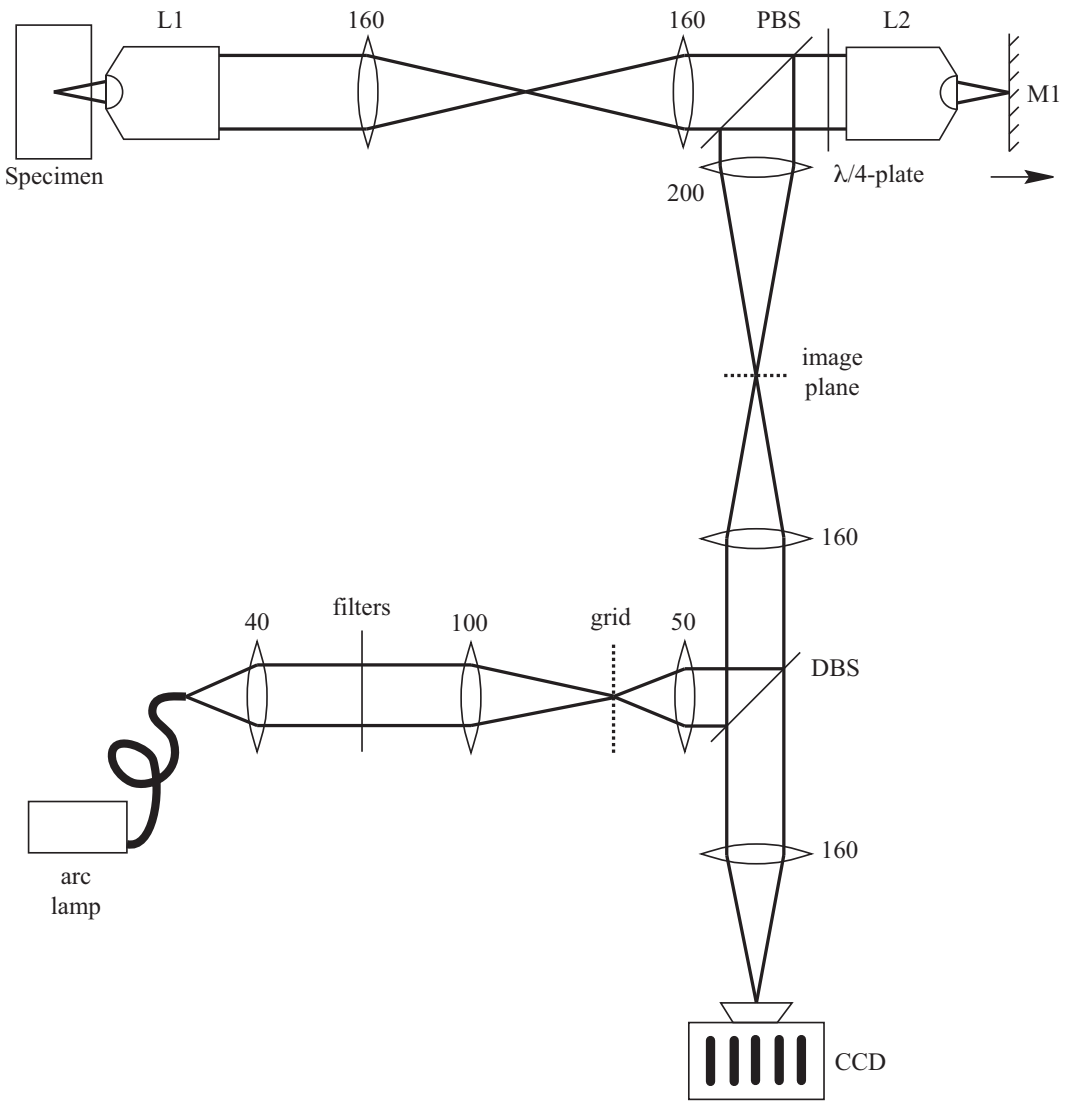

Figure 5.15: Structured illumination microscope

voltage to the control unit. The light transmitted by the grid was then re-imaged by a second 4f system, having a magnification of 3.2X, into the image plane of the microscope. This was done via a dichroic beamsplitter (DBS) with cutoff wavelength 493 nm.

Taking into account the further demagnification of 66.7X introduced by the microscope itself the resulting modulation period of the grid structure set up in the

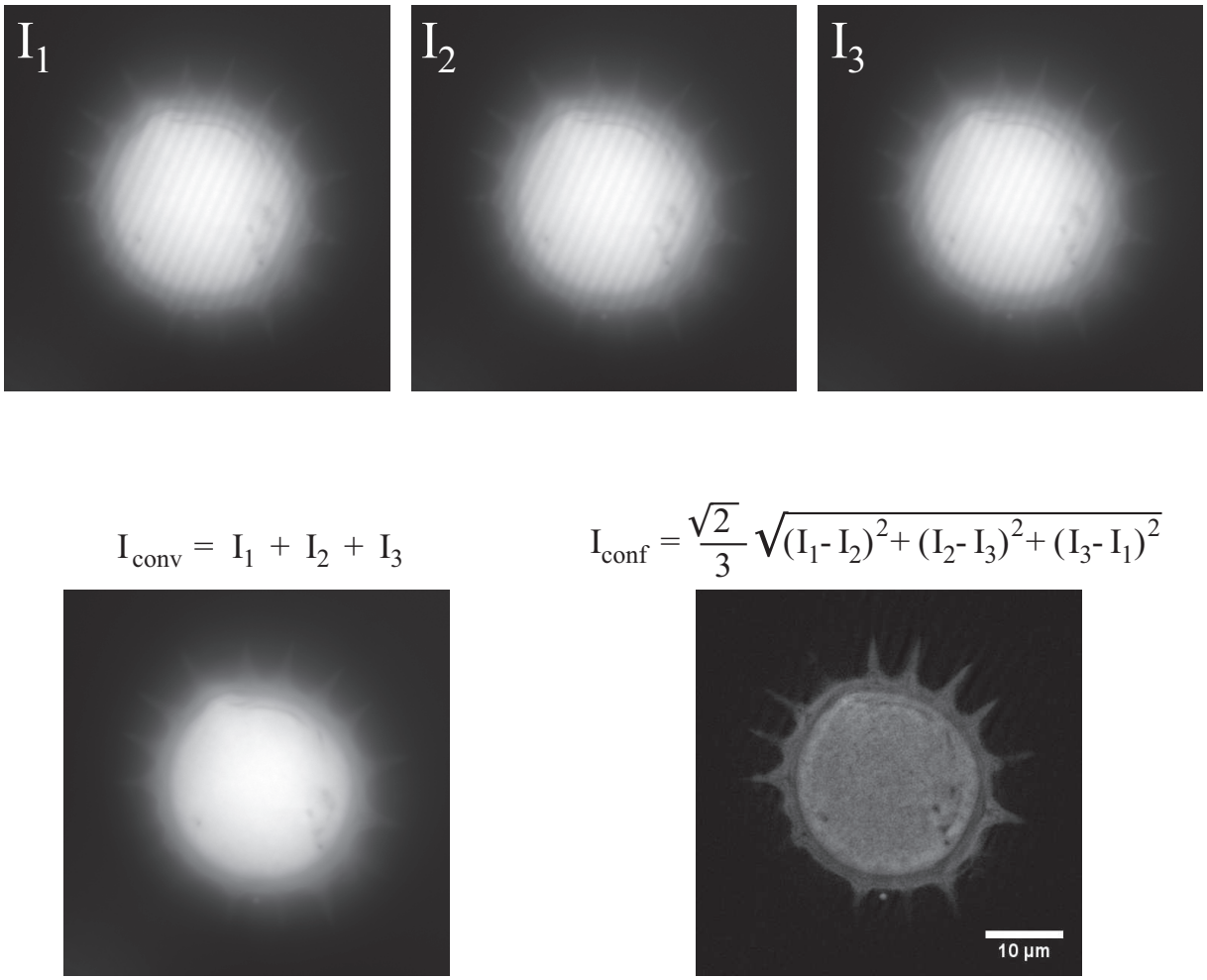

Figure 5.16: The three raw images acquired with a structured illumination microscope for a single focal setting as well as the computer generated conventional and confocal images of the specimen.

specimen was 1.2μm, which corresponded to a normalized spatial frequency of:

$$\Lambda = \frac{\lambda}{d(NA)} = \frac{457nm}{1.2\mu m \times 1.4} = 0.27. \tag{5.7}$$

This was chosen specifically so as to be close to the aforementioned value of 1/3 needed to image thick specimens.

A plane reference mirror M1 was mounted on a high precision scanning stage (P-611.3S NanoCube, PI Instruments, Karlsruhe) so that it could be shifted axially over a range of 100μm. As seen before, this mirror could be shifted axially by an

amount z to change the effective focal plane in the specimen by an amount $2z/n$, where n is the refractive index of the immersion medium of objective L1 (in this case oil with n = 1.52). Fluorescence generated in the specimen by the illumination pattern was projected back through the system and imaged onto the CCD camera. The dichroic beamsplitter and emission filter isolated fluorescence light in the range 500 - 550 nm for imaging. Custom built software was written in Labview to control CCD acquisition, the lateral position of the grid and the axial position of M1.

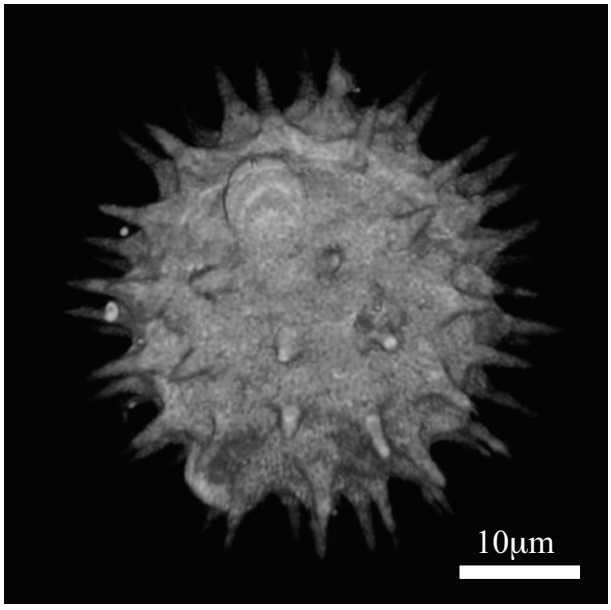

Figure 5.17: A computer generated rendering of the three dimensional image stack acquired with the structured illumination microscope.

Image stacks were then obtained for a variety of fluorescent specimens. This was done by recording three raw images, with the grid offset by a third of a period in each, at a number of different focal settings. The focal setting was changed by moving M1 in steps of 0.38 μm, which shifted the effective focal plane in the specimen by 0.5 μm. From each set of raw images the conventional and confocal images were calculated with Eqs. 5.5 and 5.6 respectively. An example of the results gained at one particular focal setting are shown in Fig. 5.16 for the same pollen grain used previously. The clear detail seen in the confocal image is a good demonstration of

the advantage obtained with this technique. Having calculated the confocal image at each focal setting, it was then possible to construct a three dimensional image stack of data and to process this information with a computer. A computational rendering generated by Volocity (Improvision, UK) for one image stack obtained in this experiment is shown in Fig. 5.17 and can be compared to the result shown on Pg. 13.

5.5 Two-photon microscopy

The final imaging system built was a spot scanning two photon fluorescence microscope. A schematic diagram of this system is shown in Fig. 5.18. This was based on the new architecture with an extra beam scanning unit added to scan the focal spot laterally in the specimen.

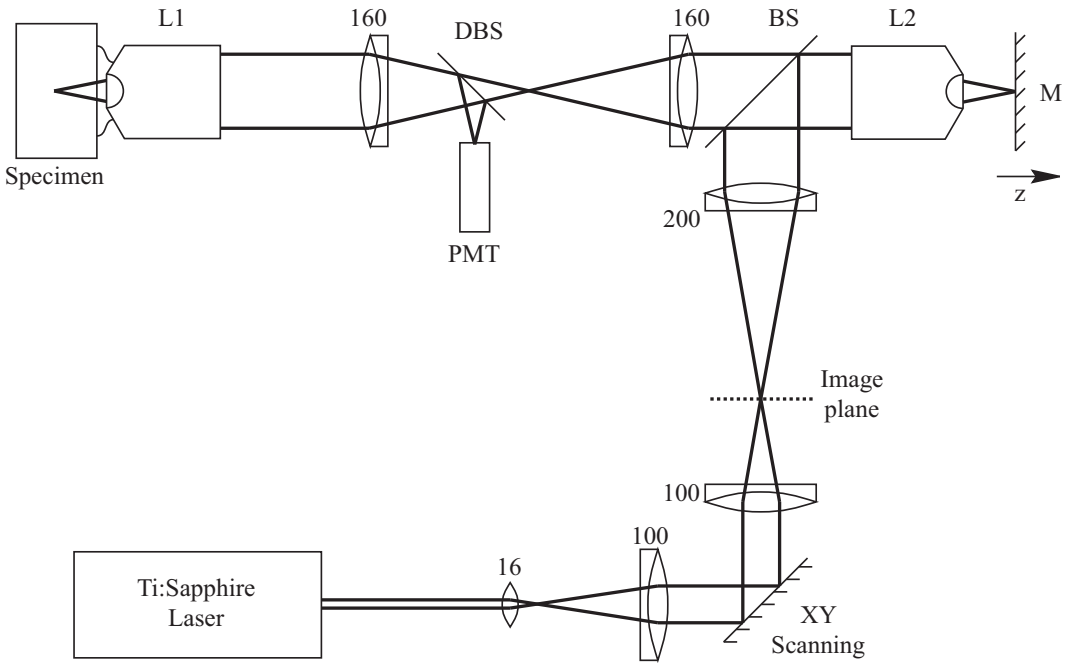

Figure 5.18: Two photon microscope with remote focusing

Illumination was provided by a Ti:Sapphire laser (*Tsunami*, Spectra Physics) with a maximum available power of 630mW, tuned to wavelength of 750nm. For

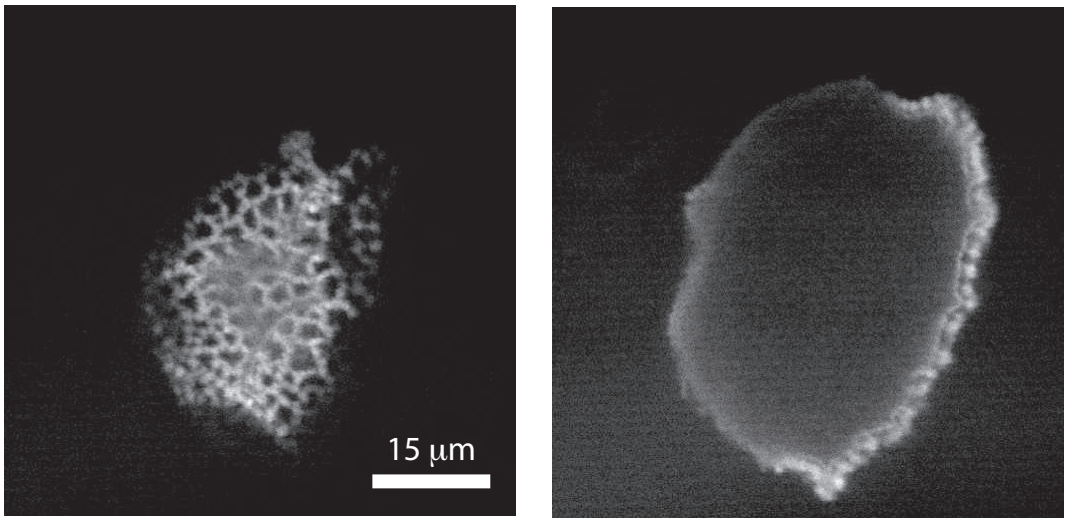

Figure 5.19: Example images from two lateral planes, separated by an axial distance of 20μm in a pollen grain specimen.

the purposes of two-photon imaging, the laser was operated in a modelocked regime, which produced pulses of length $\sim$ 100fs at a repetition rate of 80MHz. The power could be adjusted externally with a neutral density filter set. To begin with, the laser was focused to a diffraction limited spot with a lens of focal length 16mm. A 4f imaging system with unit magnification was then used to replicate this spot in the image plane of the microscope. Two galvanometer mirrors (VM1000, GSI Lumonics, UK), mounted on orthogonal axes, were included in the intermediate plane of the 4f system to provide tip and tilt to the wavefront so as to scan the lateral position of the spot in the image plane. From here, the spot was imaged into the specimen and the depth was controlled by the axial position of mirror M. A dichroic beamsplitter (DBS), reflecting light with wavelengths below 550nm, was placed behind L1 to direct photons generated by two photon fluorescence in the specimen at the location of the focal spot onto a PMT with a large sensitive area. An emission filter (not shown), with passband 500-550nm, was also included in front of the PMT to further discriminate against extraneous illumination photons that arrived at the PMT.

Custom built software, written in Labview, produced the necessary voltage wave-

forms to control the three dimensional position of the spot in the specimen, and record the intensity measured on the PMT at each point. Specifically, the beam steering unit was used to scan the spot in a raster fashion laterally in the specimen and this process was repeated at several axial positions of mirror M.

Two example images from two lateral planes, separated by an axial distance of $20\mu m$ in the specimen, are presented in Fig. 5.19. These results confirm that imaging resolution has been retained for the different focal settings. The specimen used was once again one of the pollen grains found in the commercial sample (Carolina w.m. 30- 4264 (B690)).

5.6 Conclusions and discussion

In this chapter we have built a number of imaging systems based on a novel microscope architecture described in chapter 3. Focusing to acquire data from different specimen depths was carried out using an all-optical remote focusing technique that does not require that the specimen be moved. Furthermore, the images gathered in this way did not show any signs of degradation from systematic spherical aberration.

One of the problems with the confocal imaging systems shown in sections 5.2 - 5.4 is that the polarizing beam splitter and $\lambda/4$-plate used only direct 50 % of the the fluorescence light back to the image plane. This is because the fluorescence light is essentially unpolarized. In some situations this may be an issue if the specimen emits low levels of fluorescence. One way of overcoming this problem would be to increase the illumination power incident on the specimen from the light source. Fluorescence emission would be initiated at a higher rate and lead to more photons being produced in the specimen but it must be noted that this may be accompanied by other detrimental effects, such as increased levels of photo-bleaching. Another way of circumventing this problem would be to use the transmission architecture shown in Fig. 3.5a on Pg. 54. In this case, a third objective lens is used and the

full fluorescence intensity from the specimen will be projected onto the image plane. The drawback of this approach, though, is that axial scan speed will once again be limited to the speed at which the third objective lens can be moved. Refocusing is still carried out remotely though so this approach may still have advantages for certain applications.

In the case of the two photon microscope, shown in Fig. 5.18, the problems of fluorescence loss are not an issue. This is because the detection optics simply collect and measure the intensity of fluorescence light emitted by the specimen without re-imaging it in any way. As a result, the full intensity of fluorescence light is measured without requiring it to return back through the system.

Other issues are important to take into account with the two photon microscope arrangement. Not least is the problem of the extreme light intensity that is incident on the refocusing mirror while it is in focus. If the intensity of the focal spot on the mirror is too high then heating effects can destroy the mirror integrity leading to system failure. A number of things can be done to overcome this problem. The first is to use only part of the focusing range of the system such that the mirror is never in the most intense parts of the focal spot. In fact, this is what was done here to acquire the example images in Fig. 5.19. In this case, the specimen was deliberately placed at the extremity of the focusing range so that the mirror was not illuminated with the full intensity of the focal spot. A second option would be to use a high threshold mirror that can withstand the high intensities of the focal spot. The highest threshold metal mirrors available usually consist of a thin layer of gold coated onto a copper substrate and should be able to withstand the intensities required for two photon imaging. Another option might be to design a dielectric mirror instead, however care would need to taken to ensure that it reflects equally at all angles of incidence because the illumination cone set up by the objective lens extends over a large angular range. The issue of mirror ablation can be circumvented completely, however, by using the transmission architecture of Fig. 3.5a but as before this would

restrict the speed at which the system can be scanned along the axis.

Chapter 6

Conclusions and discussion

A common requirement in high-resolution optical microscopy is to obtain information from a three-dimensional object under investigation. This is typically achieved via an intermediate step using an optical sectioning technique, such as confocal microscopy, to eliminate the out-of-focus blur in order to obtain a clean in-focus image of a single plane within the specimen. This process is repeated a number of times at different focal settings and gradually a full three dimensional data set containing information about the whole object is gathered. This information can then be manipulated and displayed on a computer to reveal a wealth of information about the object structure. In most practical implementations a single in-focus image can be acquired very quickly. However, the real bottleneck in three dimensional data acquisition is the process of refocusing the microscope to successive image planes. This thesis has been concerned with the improvement of image acquisition speeds while imaging such volumetric specimens in microscopy.

In chapter 2, a novel technique was developed for two photon fluorescence microscopy that permitted extended depth of field images to be acquired directly in a single image scan. This was done by extending the point spread function of the microscope along the axial direction by illuminating the back aperture of the objective lens with an annular ring of light. The real challenge for two photon microscopy

applications, however, was to develop a technique for producing the annular ring of light in a light efficient manner so that imaging could be carried out without excessive amounts of laser power. We therefore used a binary phase-only grating and this diffractive element was able to produce the required beam with an efficiency exceeding 75%. In this way, two photon fluorescence images were obtained with a depth of field extended by more than an order of magnitude. In addition to the phase mask, we introduced a further step of spatial filtering in the Fourier plane of the mask which enabled us to fine tune the axial profile of the illumination PSF and thus achieve a near constant image intensity throughout the depth of field. It has to be emphasized that all these enhancements in depth of field were achieved without compromising the lateral resolution of the microscope. The potential scope of application of this method was further broadened by demonstrating a stereo imaging capability. This was achieved by obtaining a pair of extended depth of field images from different viewing parallaxes by employing tilted PSFs.

In chapter 3, a new microscope system architecture was described that permits refocusing to be carried out remotely without introducing mechanical movements near the specimen. The standard microscope architecture used in most commercial systems only permits a single specimen plane to be imaged without aberration and it is therefore necessary to physically move the specimen or objective lens to image other planes. With the new architecture, however, aberration-free images can be acquired from an effective focal plane in the specimen that can be shifted along the axis remotely. As a result, information from a range of specimen depths can be acquired without introducing movements near the specimen.

Using a high NA scalar theory, a mathematical analysis was carried out for this architecture which revealed that refocusing could be carried out over an axial range of 140μm for a 1.4 NA 60$\times$ oil immersion objective. This range was calculated by requiring the Strehl ratio to be greater than 0.8 at all points. The analysis also assumed that the objective lenses used conform strictly to the sine condition.

In chapter 4, point spread function measurements were obtained using commercially available objective lenses and it was found that refocusing could be carried out over an axial range of 70μm for the same lens modelled in the theoretical analysis. The discrepancy between these measurements and the theory can be accounted for by the fact that commercial lenses are often optimised to produce a large lateral field of view and hence do not conform strictly to the sine condition.

In chapter 5, some prototype imaging systems were constructed to demonstrate the application of a number of sectioning techniques to the new microscope architecture. Specifically, the techniques of point scanning, line scanning and structured illumination microscopies were all applied and image data recorded from a range of different depths in the specimen. All specimens were held stationary during imaging.

The applications of this approach are, of course, not limited to the few simple cases shown in this thesis. Indeed, any system previously based on the standard microscope architecture could be reconstructed using the new architecture to allow focusing to be carried out remotely. For example, microscopes employing other sectioning techniques such as coherent anti-stokes raman scattering [45, 46], second-harmonic generation [47, 48] and third- harmonic generation [49, 50] could certainly be adapted in this way. This is testament to the extreme generality of this approach.

One of the most important advantages of this new approach is the improvement in axial scan speeds that can be obtained. This is the direct result of the fact that refocusing is carried out by moving a small mirror. In this thesis, the mirror was mounted on an actuator that would allow axial scan speeds of up to 1 kHz over the full focusing range. Through developments, it is expected that this speed could be improved further. In any case, the current situation already permits a considerable improvement over the axial scan speeds that are permitted by commercial microscope systems, which typically lie in the range 10-100 Hz.

The fact that focusing is carried out remotely with this approach could prove useful for certain imaging applications. For instance, up until now, it would have

been hard to acquire a three dimensional image stack of a floating specimen using a water dipping objective lens. This is because the process of refocusing the objective lens mechanically would disturb the medium surrounding the specimen and cause it to move during imaging. Using the new technique, however, focusing would be carried out remotely so the specimen would be imaged without affecting its environment.

Finally, we mention some of the extra imaging modalities that could be orchestrated with the two photon microscope system shown in the previous chapter. As well as being able to acquire two dimensional images from a number of X-Y planes, located at different specimen depths, it should also be possible to use the axial scan motion to permit images to be acquired from other planes having arbitrary orientation and position. In addition to this, images could be recorded from a curved surface. This would be useful, for instance, if biological activity was constrained to take place over a curved surface, as information could be acquired directly in a single scan instead of deriving it from a three dimensional image stack. In certain situations, it may be of interest to monitor biological activity along arbitrary line trajectories in three dimensions at high speed. This would also be possible to orchestrate with the current arrangement. Finally, the focal spot could also be scanned to a discrete set of specimen locations in three dimensions to monitor activity at each point.

In summary, the initial proof-of-principle of this new microscope architecture has been carried out in this thesis and a theoretical model established. As this approach is extremely general there is great potential for applying these ideas to a number of areas in biological imaging and this will be the subject of future work.

Appendix A

Imaging theory and the point spread function

This appendix contains a brief summary of the Kirchhoff-Fresnel scalar diffraction theory and explains how the point spread function is calculated for a low NA lens.

A.1 Kirchhoff-Fresnel scalar diffraction theory

The goal of diffraction theory is to predict how a wave disturbance develops in the course of time. In 1678 Huygens [25] expressed the intuitive conviction that if each point on a wavefront were considered to be a new source of a *secondary* spherical disturbance, then the wavefront at a later instant could be found by constructing the envelope of secondary wavelets. This concept is shown diagrammatically in Fig. A.1 below. Much later, in 1818, this principle was formulated mathematically by Fresnel so for the first time it was possible to make quantitative predictions about the propagation of optical wavefronts. Kirchhoff then made certain assumptions, in 1882, to show consistency between Fresnel's theory and Maxwell's equations of

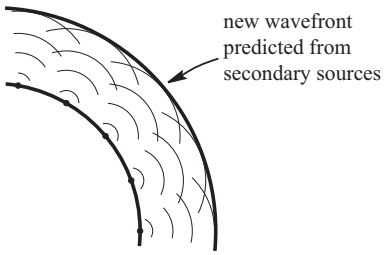

Figure A.1: *Diagrammatic representation of Huygens principle showing how a secondary wavefront is predicted by summing up spherical contributions from a primary wavefront.*

electromagnetism. The Kirchhoff integral can be stated as follows:

$$U_2(x_2, y_2) = \frac{i}{\lambda} \iint_{-\infty}^{\infty} U_1(x_1, y_1) \frac{e^{-ikr}}{r} \left[\frac{1 + \cos\theta}{2}\right] \mathrm{d}x_1 \mathrm{d}y_1 \tag{A.1}$$

where $k = \frac{2\pi}{\lambda}$ and λ is the wavelength of illumination. This expression can be understood with reference to Fig. A.2. Each elemental area of the diffraction plane is the source of a spherical wave, which propagates outwards until it reaches the observation plane. The amplitude and phase of this wave in the diffraction plane is given by the complex scalar function $U_1(x_1, y_1)$. However, in reaching its destination, it diminishes in amplitude and changes in phase, which gives rise to the factors $1/r$ and e^{-ikr} respectively. Finally a term called the obliquity factor is also introduced, $\left[\frac{1+\cos\theta}{2}\right]$, to prevent the spherical waves generating a backward propagating light field. Integration of the spherical waves arriving at each point in the observation plane give rise to the amplitude and phase of the new wavefront formed.

Two approximations can be introduced to develop this expression further. First, we only consider the rays travelling close to the optical axis and hence set $\theta \simeq 0$, which is the paraxial approximation. Second, with reference to Fig. A.2, we consider the case where $a \ll z$, which is known as the Fresnel approximation. Using this approximation, it is possible to make the following binomial expansion:

$$r = \sqrt{z^2 + (x_2 - x_1)^2 + (y_2 - y_1)^2} \approx z \left[1 + \frac{(x_2 - x_1)^2 + (y_2 - y_1)^2}{2z^2} + ...\right], \tag{A.2}$$

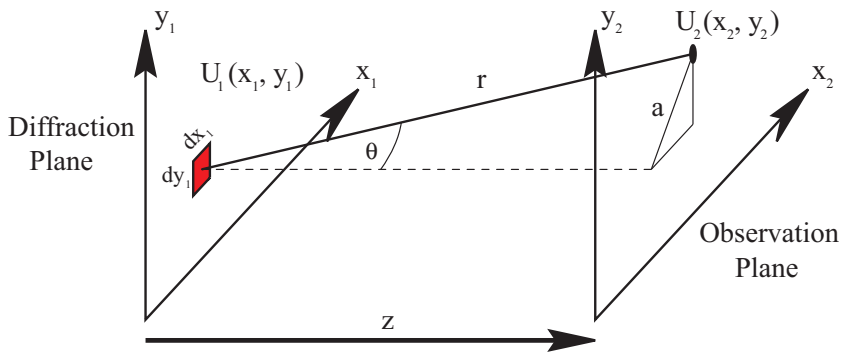

Figure A.2: *The complex field $U_2(x_2, y_2)$ at any point in the observation plane is simply the sum of all the spherical wave contributions from the diffraction plane. This summation is given by the Kirchhoff Integral.*

which is then used in argument of the exponential function in the integrand. Under these approximations the factor $1/r$ in the integrand does not vary so much for small changes in r so it can be replaced by $1/z$ and the expression that emerges is usually referred to as the Kirchhoff-Fresnel integral:

$$U_2(x_2, y_2) = \frac{ie^{-ikz}}{\lambda z} \iint_{-\infty}^{\infty} U_1(x_1, y_1) e^{-\frac{ik}{2z}\left[(x_2-x_1)^2+(y_2-y_1)^2\right]} \mathrm{d}x_1 \mathrm{d}y_1 \tag{A.3}$$

which is simply the convolution of some exponential function with the waveform in the diffraction plane. It is emphasized that the wavefronts considered here are only scalar functions and hence the effects of polarization are not included in this formulation.

A.2 The point spread function

For the situation where a plane wave falls incident on a thin lens, as shown in Fig. A.3, geometric optics predicts that the light is focused to an infinitesimally small spot in the focal plane, with an amplitude distribution described by a delta function $\delta(x_2, y_2)$. In practice, though, this does not happen because the light has a finite wavelength spread and so the limiting aperture of the lens causes the resulting

amplitude distribution to spread out and take significant values over a finite region. This amplitude distribution is known as the point spread function (PSF) of the lens. We can write down a mathematical expression for the PSF using the Kirchhoff-Fresnel integral but first we must understand how the lens transforms the incoming wavefront.

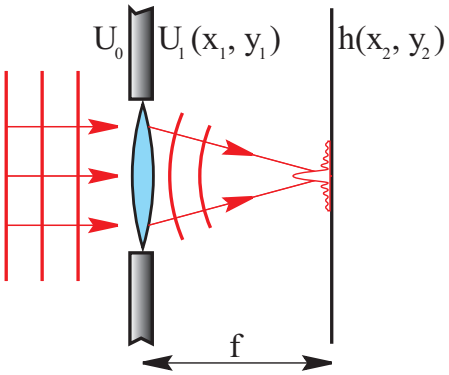

Figure A.3: *A plane wave incident on a thin lens is focused onto the focal plane and forms a complex* point spread function $= h(x_2, y_2)$.

As shown in the Fig. A.3, the lens transforms the plane wave into a spherical wave and also apodizes the incoming waveform. Mathematically, the wavefront that emerges from the lens, as a function of the incident amplitude U_0, is:

$$U_1(x_1, y_1) = U_0 P(x_1, y_1) e^{\frac{ik}{2f}(x_1^2+y_1^2)}, \tag{A.4}$$

where the function $P(x_1, y_1)$ is present to account for the apodization. This is often referred to as the pupil function and takes the form:

$$P(x_1, y_1) = \begin{cases} 1, & \text{inside the lens} \\ 0, & \text{outside the lens} \end{cases} \tag{A.5}$$

The quadratic phase variation describes the transformation of plane waves into spherical waves and is only a good approximation for low NA lenses. The propensity for a thin lens to deform an incoming wavefront is therefore characterized by a single

parameter f, which is referred to as the focal distance. Setting $U_0 = 1$, the PSF in the focal plane can now be evaluated from the Kirchhoff-Fresnel integral:

$$\begin{aligned} h(x_2, y_2) &= \frac{i}{\lambda f} e^{-ikf} \iint_{-\infty}^{\infty} P(x_1, y_1) e^{\frac{ik}{2f}(x_1^2+y_1^2)} e^{-\frac{ik}{2f}\left[(x_2-x_1)^2+(y_2-y_1)^2\right]} \mathrm{d}x_1 \mathrm{d}y_1 \\ &= \frac{i}{\lambda f} e^{-ikf} e^{-\frac{ik}{2f}(x_2^2+y_2^2)} \iint_{-\infty}^{\infty} P(x_1, y_1) e^{\frac{ik}{f}(x_2 x_1 + y_2 y_1)} \mathrm{d}x_1 \mathrm{d}y_1 \end{aligned} \tag{A.6}$$

which is simply the two dimensional Fourier transform of the pupil function. A more general expression, which predicts the PSF in other planes, not just in the focal one, can also be formulated from the Kirchhoff-Fresnel integral:

$$h(x_2, y_2, z) = \frac{i}{\lambda z} e^{-ikz} \iint_{-\infty}^{\infty} P(x_1, y_1) e^{\frac{ik}{2f}(x_1^2+y_1^2)} e^{-\frac{ik}{2z}\left[(x_2-x_1)^2+(y_2-y_1)^2\right]} \mathrm{d}x_1 \mathrm{d}y_1. \tag{A.7}$$

This can be simplified by making a change of variable, $z = f + \Delta z$, and considering only planes with $\Delta z \ll f$ so that $1/z \approx 1/f - \Delta z/f^2$. This results in:

$$h(x_2, y_2, \Delta z) \propto \iint_{-\infty}^{\infty} P(x_1, y_1) e^{\frac{ik\Delta z}{2f^2}\left(x_1^2+y_1^2\right)} e^{\frac{ik}{f}(x_1 x_2 + y_1 y_2)} e^{-\frac{ik\Delta z}{f^2}(x_1 x_2 + y_1 y_2)} \mathrm{d}x_1 \mathrm{d}y_1, \tag{A.8}$$

where all the pre-factors have been omitted as we are mainly concerned with the relative values of $|h(.)|^2$ in this work. For small changes of x_2, y_2 and Δz it is possible to neglect the variation introduced by the final exponential term in the integrand and further simplification can be made introducing normalized co-ordinates in the pupil plane, namely $m = x_1/a$ and $m = x_1/a$. Also, $a/f \approx \sin\alpha$ where α is the semi aperture angle of the objective lens. The PSF is therefore:

$$h(x_2, y_2, \Delta z) \propto \iint_{-\infty}^{\infty} P'(m, n) e^{\frac{ik\Delta z \sin^2\alpha}{2}\left(m^2+n^2\right)} e^{ik\sin\alpha(m x_2 + n y_2)} \mathrm{d}m \mathrm{d}n, \tag{A.9}$$

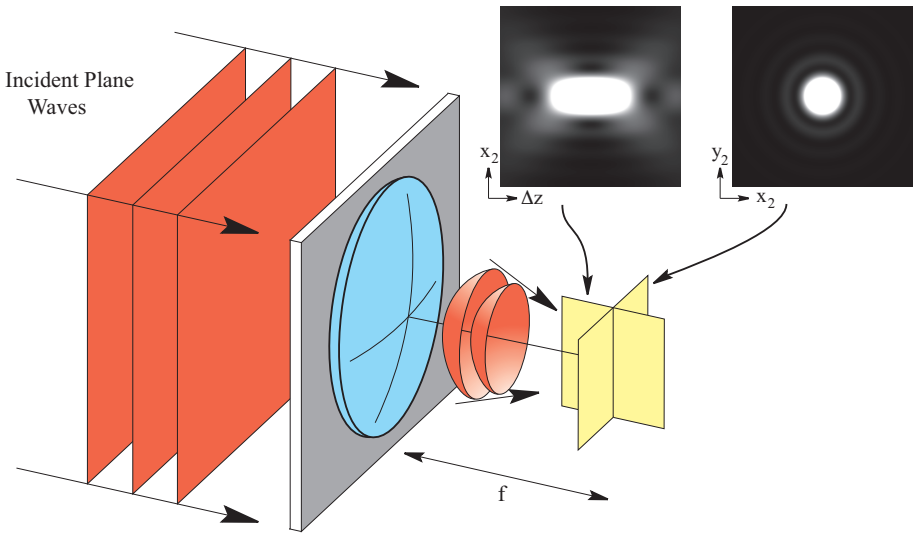

Figure A.4: *Density plots showing the intensity distribution formed by a lens with* $NA = 0.5$ *when illuminated with a plane wave.*

where for a simple lens with no residual aberrations:

$$P'(m,n) = \begin{cases} 1, & \sqrt{m^2+n^2} \leq 1, \\ 0, & \sqrt{m^2+n^2} > 1. \end{cases} \tag{A.10}$$

The intensity distribution set up in the focal region of the lens is proportional to $|h(x_2, y_2, \Delta z)|^2$. Plots of this are shown in the focal plane and meridional plane in Fig. A.4 for a dry lens with $NA = \sin\alpha = 0.5$.

It is noted that although we have evaluated the illumination PSF here the same expression may be used to describe the detection PSF in a confocal system.

Appendix B

The generalized microscope

This appendix contains brief derivations of the various convolution theorems that describe the imaging properties of sectioning microscopes. Fig. B.1 shows the schematic diagram of a confocal fluorescence microscope. A laser illuminates a small pinhole placed in the entrance aperture of a microscope system. This sets up an effective point source of light, which is imaged into the specimen by the 4f system forming the illumination arm of the microscope. The resulting amplitude distribution, known as the illumination PSF, is predominantly confined to a small volumetric region as shown.

In fluorescence mode, molecules lying in the illumination PSF are excited and photons emitted by the subsequent emissions are separated out by a dichroic beam-splitter (DBS) and imaged onto a detection pinhole by a further 4f system. The light transmitted by the pinhole is then measured by a photo-multiplier tube (PMT). It is important to note that phase coherence between the contributions arising from different points in the specimen is lost during the fluorescence process. A three dimensional image stack can then be recorded by physically moving the specimen and measuring the fluorescence emission generated at a matrix of different locations.

We first take a look at the imaging properties of a single 4f system with unit magnification. Fig. B.2 shows how two point sources of light, placed at different

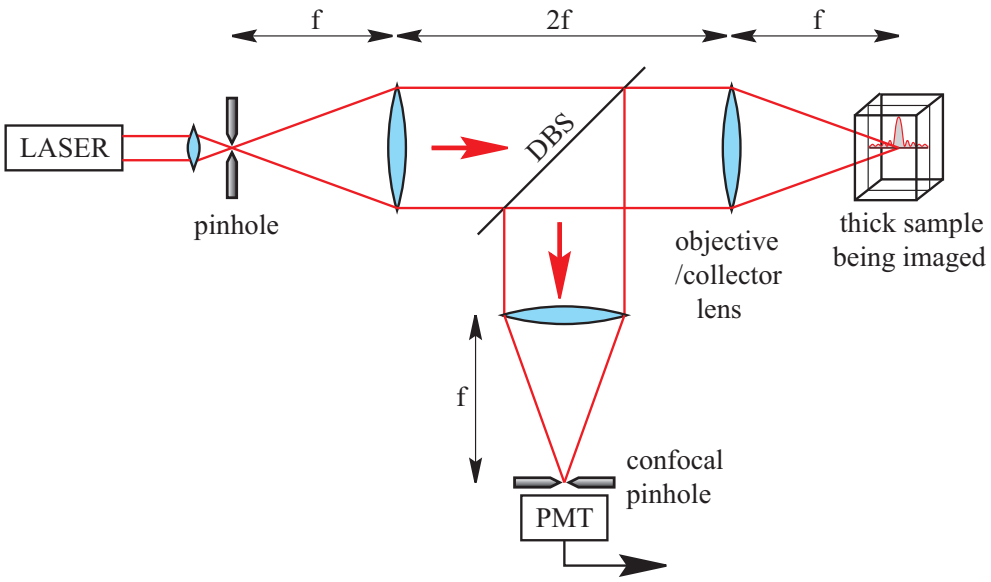

Figure B.1: *Schematic diagram of the confocal microscope*

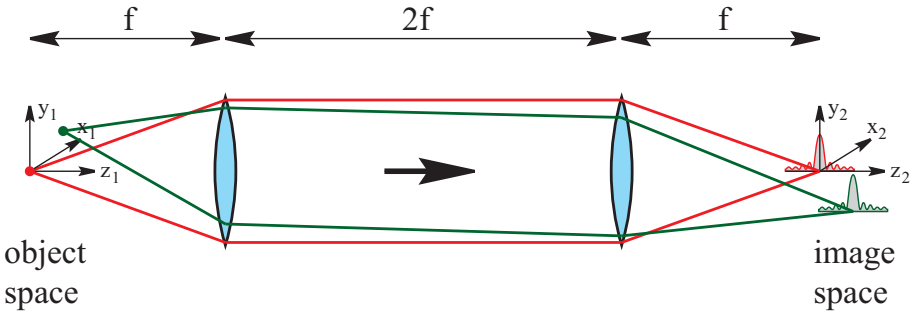

Figure B.2: *The imaging properties of a 4f system of lenses.*

positions, are imaged by this system. Under the assumptions of geometric optics a point source placed at position $\mathbf{r}_1 = (x_1, y_1, z_1)$ should produce a point-like image at $\mathbf{r}_2 = (-x_1, -y_1, z_1)$. The effect of wave optics is to broaden out these images into PSF distributions. The amplitude distribution in image space setup by a point source placed at $\mathbf{r}_1$ in image space is therefore $h(\mathbf{r}_2 - \mathbf{M}\mathbf{r}_1)$, where M is defined as:

$$\mathbf{M} = \begin{pmatrix} -1 & 0 & 0 \\ 0 & -1 & 0 \\ 0 & 0 & 1 \end{pmatrix} \tag{B.1}$$

This result will be used in the following sections to derive the imaging properties

of a fluoresence confocal microscope and a two photon microscope.

B.1 Fluorescence confocal imaging

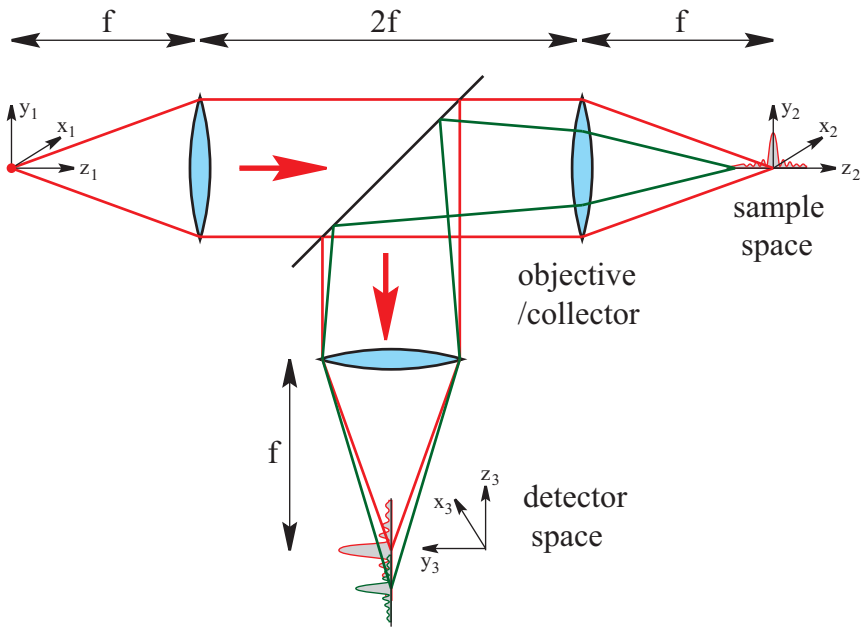

Figure B.3: *Each point in sample space sets up a further PSF in detector space.*

In fluorescence imaging, contrast is achieved by measuring the density of fluorescent molecules at each point in the sample $\sigma_f(\mathbf{r}_2)$. With reference to Fig. B.3, the laser source at the origin of the $\mathbf{r}_1$ co-ordinate system sets up an illumination PSF, $h_1(\mathbf{r}_2)$, centred on the origin of the $\mathbf{r}_2$ co-ordinate system, where the specimen is placed. Molecules lying at each point in the sample are excited at a rate proportional to the intensity they experience, $|h_1(\mathbf{r}_2)|^2$. The subsequent decay of these molecules at each point once again acts as a new point source that sets up a further PSF in detector space. Assuming no change of wavelength during the fluorescence process, the intensity distribution produced from one such sample point is:

$$I(\mathbf{r}_2, \mathbf{r}_3) = |h_1(\mathbf{r}_2)|^2 \, \sigma_f(\mathbf{r}_2 - \mathbf{r}_s) \, |h_2(\mathbf{r}_2 - \mathbf{M}\mathbf{r}_3)|^2 \tag{B.2}$$

Now, the intensity measured by a pinhole placed at $\mathbf{r}_3 = 0$ is the sum of the intensity contributions from all points in the sample. The reason for summing intensity contributions is that phase coherence is lost during the fluorescence process and hence the interference between the PSFs in detector space arising from different sample points averages to zero over time. The resulting intensity measured at $\mathbf{r}_3 = 0$ is therefore:

$$I(\mathbf{r}_s) = \int |h_1(\mathbf{r}_2)|^2 \, \sigma_f(\mathbf{r}_2 - \mathbf{r}_s) \, |h_2(\mathbf{r}_2 - \mathbf{M}\mathbf{r}_3)|^2 \, \mathrm{d}^3\mathbf{r}_2 \tag{B.3}$$

which we can also re-write using the convolution operator:

$$I(\mathbf{r}_s) = |h_1|^2 \, |h_2|^2 \otimes \sigma_f \tag{B.4}$$

In most cases the illumination and detection paths are identical so we can set $h_1 = h_2 = h$ and the equation describing the imaging properties of a confocal fluorescence microscope is:

$$I(\mathbf{r}_s) = |h|^4 \otimes \sigma_f \qquad \text{... single photon fluorescence mode} \tag{B.5}$$

From this, we can see that the function that we are trying to measure (σ_f) is essentially blurred out by the PSF distribution raised to the fourth power. The PSF function therefore determines the resolution of the system.

B.2 Two-photon fluorescence imaging

In two photon fluorescence microscopy, image contrast is also achieved by measuring the density of fluorescent molecules at each point in the sample $\sigma_{2f}(\mathbf{r}_2)$. A system similar to that shown in Fig. B.3 can be used with the detection pinhole removed so that the full intensity of fluorescence can be measured. As such, the detection

arm of the system serves to collect the fluorescence photons and does not affect the imaging properties of the microscope.

The difference between this mode and the single photon fluorescence mode is that the fluorescence light generated at each point in the specimen by the illumination PSF is the result of two-photon excitation processes. This second order effect has a far reduced likelihood of occurring and produces fluorescence photons at a rate proportional to the square of the illumination intensity, i.e. $|h_1|^4$. As such the fluorescence generation in the sample can therefore be evaluated as:

$$I(\mathbf{r}_s) = |h_1|^4 \otimes \sigma_{2f} \qquad \text{... two photon fluorescence mode.} \tag{B.6}$$

The detection path collects a proportion of these photons and measures them. This equation therefore describes the imaging properties of a two-photon microscope and it can be seen from this that the detection path has no effect on the imaging properties of this system. From Eqs. B.5 and B.6 we see that the resolution of both these microscopes is the same if we neglect the effects of noise.

Appendix C

High NA scalar theory and spherical aberration

In this appendix we develop the expression for the PSF derived in appendix A further to find a more appropriate form that is specific for high NA objective lenses.

Fig. C.1 shows a standard microscope configuration comprising a high NA objective lens and tube lens. A pinhole is placed in the image plane and is associated with a PSF, $h(x, y, z)$, which can be interpreted in two different ways. First, for the case where laser light is introduced into this system via the pinhole, it can be interpreted as the illumination PSF and $h(x, y, z)$ describes the amplitude distribution set up in the focal region of the objective. Second, for the case where the pinhole is used to filter light emanating from the specimen in object space, $h(x, y, z)$ tells us what regions of the specimen the pinhole is sensitive to.

In appendix A, an expression for $h(x, y, z)$ was derived that was appropriate for lenses with low NA:

$$h(x, y, z) = \iint_{-\infty}^{\infty} P(m, n) e^{\frac{ikz \sin^2 \alpha}{2}\left(m^2+n^2\right)} e^{ik \sin \alpha (mx+ny)} \mathrm{d}m\mathrm{d}n. \tag{C.1}$$

Here, $k = 2\pi/\lambda$, where λ is the illumination wavelength, m and n are the normalized

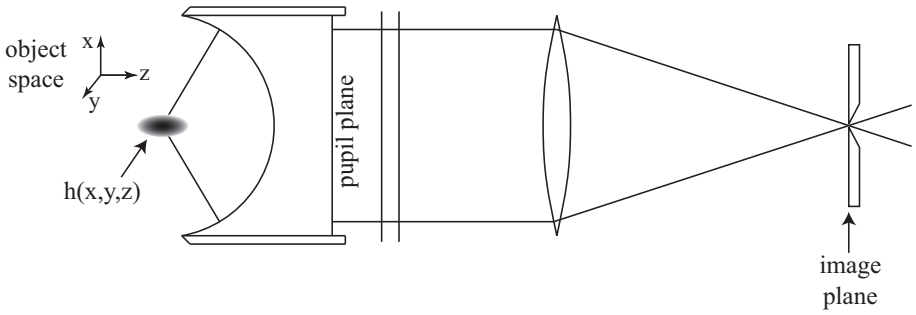

Figure C.1: *Standard microscope detection PSF*

Cartesian co-ordinates in the pupil plane and α is the semi-angular aperture of the lens. For a lens with no residual aberrations the pupil function, $P(m,n)$, is defined as being unity over the unit circle and zero elsewhere. We note that the phase profile described by the exponential terms in the integrand is simply equivalent to that produced in the pupil plane when a point source is placed at position (x,y,z) in the focal region of a low NA lens. In chapter 3 (Pg. 49) we found an equivalent expression for the phase profile generated in the case of a high NA lens:

$$\Psi(\rho,\phi;\mathbf{r}) \approx -k\sin\alpha\left\{mx+ny+z\sqrt{cosec^2\alpha-\rho^2}\right\}, \tag{C.2}$$

where a radial co-ordinate, $\rho=\sqrt{m^2+n^2}$, is used in the pupil plane for convenience. This profile differs slightly from the case of a low NA lens in the final term. Eq. C.1 can therefore be restated in a way that is more appropriate for high NA lenses:

$$h(x,y,z)=\iint_{-\infty}^{\infty} P(m,n)e^{-ikz\sin\alpha\sqrt{cosec^2\alpha-\rho^2}}e^{-ik\sin\alpha(mx+ny)}\mathrm{d}m\mathrm{d}n. \tag{C.3}$$

It is noted that in cases where the lens uses an immersion media, this expression is still valid if k is multiplied by the refractive index of the immersion media.

Consider now the situation shown in Fig. C.2, where the pinhole is displaced a distance z_p along the axis of the system. The pinhole here is sensitive to a single spatial mode that corresponds to the phase profile shown in the pupil plane of the

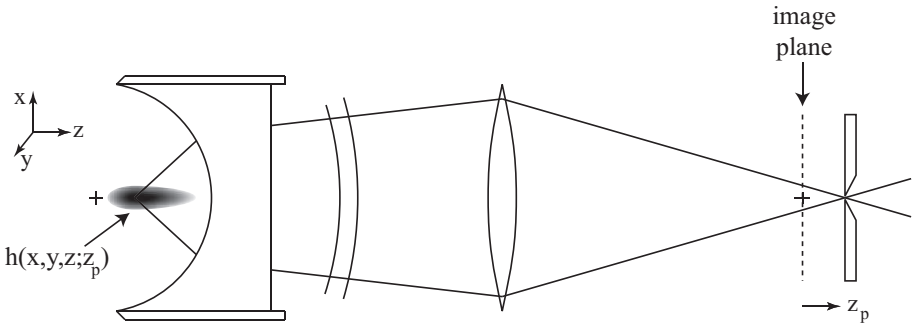

Figure C.2: *Standard microscope detection PSF*

objective lens. This phase profile is determined by the low NA tube lens and can be described by the following quadratic expression:

$$\psi(z_p) = \frac{kz_p \sin^2 \alpha}{2M_a}\rho^2, \tag{C.4}$$

where M_a is the axial magnification of this optical system. A complete expression for the PSF in this case, whether for illumination or detection, can therefore be written as:

$$h(x,y,z;z_p) = \iint_{-\infty}^{\infty} P(m,n) e^{i\frac{kz_p \sin^2 \alpha}{2M_a}\rho^2} e^{-ikz \sin\alpha\sqrt{cosec^2\alpha - \rho^2}} e^{-ik\sin\alpha(mx+ny)} \mathrm{d}m\mathrm{d}n, \tag{C.5}$$

Example density plots of $|h(.)|^2$ in the meridional plane of object space are shown in Fig. C.3 for three different axial locations of the pinhole ($z_p(mm) = -15, 0, 15$). An oil immersion objective lens from Olympus 1.4 NA 60× was assumed from these calulations along with a tube lens of focal length 180mm and wavelength $\lambda = 633nm$. Three main conclusions can be drawn from looking at these PSFs. The first is that the process of moving the pinhole has effectively refocused the PSF along the axis so that the system is sensitive to a different region of the specimen. The second is that the PSF shape has broadened out along the axis, which will lead to a deterioration of the sectioning performance of the system. The third is that the peak intensity

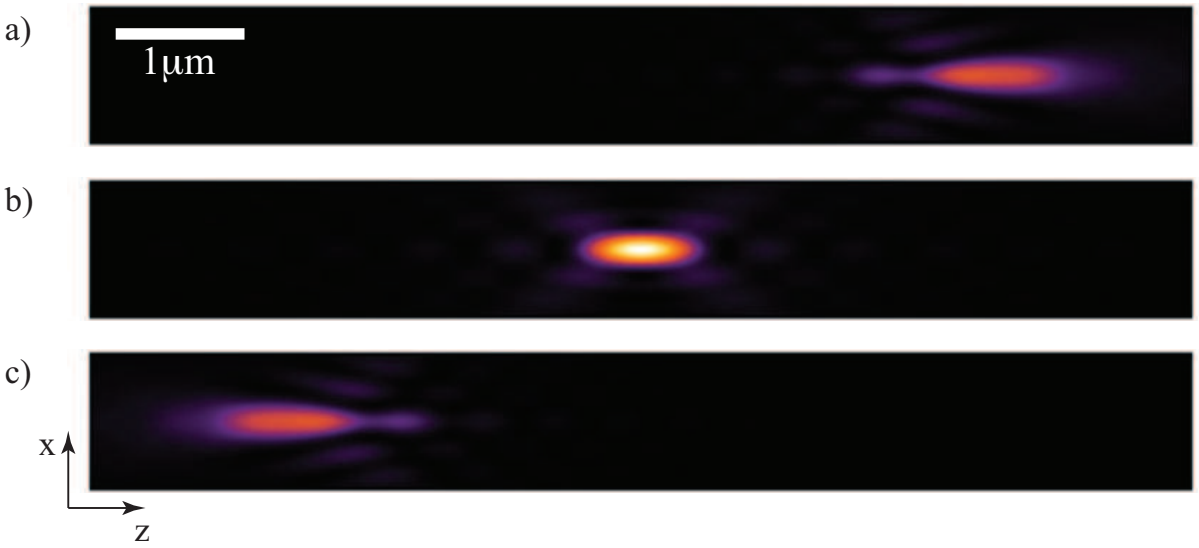

Figure C.3: *Plots of the PSF distribution in the meridional plane for different axial locations of the pinhole. a)* $z_p = 15mm$*, b)* $z_p = 0$ *and c)* $z_p = -15mm$*. See text for details.*

value is reduced for axially displaced positions which ultimately leads to a reduction in signal strength that will be collected from such regions.

Finally, we note that the pupil function can be recast in the following way:

$$h(x, y, z; z_p) = \iint_{-\infty}^{\infty} P(m, n, z; z_p) e^{-ik \sin\alpha (mx+ny)} \mathrm{d}m\mathrm{d}n, \tag{C.6}$$

where

$$P(m, n, z; z_p) = \begin{cases} e^{i\frac{kz_p \sin^2\alpha}{2M_a}\rho^2} e^{-ikz \sin\alpha \sqrt{cosec^2\alpha - \rho^2}}, & \rho \leq 1 \\ 0, & \rho > 1 \end{cases} \tag{C.7}$$

This expression is the one used in chapter 4.

Appendix D

High NA vectorial theory

In Appendix A, the derivation of the PSF distribution stemmed from the Huygens-Fresnel diffraction integral in Eq. A.3. This integral was derived from the scalar wave equation and is only applicable in the regime of paraxial optics, where the light rays propagate along directions close to the optical axis. Commercial objective lenses, however, refract light rays through large angles and so do not strictly operate in the paraxial regime. As a result, the expressions we have derived so far for the PSF are no longer valid. The Huygens-Fresnel integral can be adapted, however, using the Debye theory [35] in order to provide us with a mathematical description for high NA lenses.

D.1 The Debye theory

It has already been shown in Eq. A.4 that the effect of a thin lens is to convert a plane wave to a spherical wavefront that converges towards the focal point. Previously, to find the amplitude distribution around the focal point, we summed up contributions from secondary sources lying in a *plane* immediately following the lens. For high NA lenses, however, it is more appropriate to sum up contributions from secondary sources lying on our newly formed *spherical* wavefront, as shown in Fig.

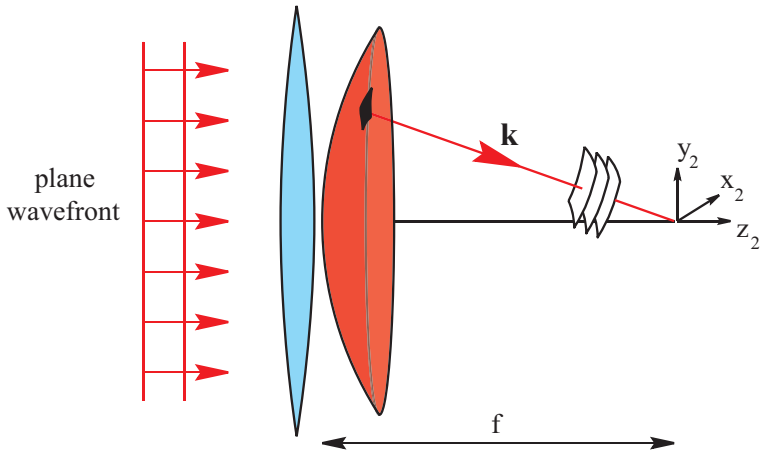

Figure D.1: *A plane wave is converted to a spherical wave by a lens. In the Debye theory, the secondary source contributions from this new wavefront are assumed to be flat by the time they reach points near the origin and are therefore approximated as plane waves.*

D.1. Although these secondary sources produce spherical wavelets, it is found that for very small displacements from the focal point ($r_2 \ll f$) these wavelets appear to be flat, to within a fraction of a wavelength, and can therefore be approximated as plane waves $\sim e^{-i\mathbf{k}\cdot\mathbf{r}_2}$. Summing the amplitude and phase contributions of all these secondary sources gives the following expression:

$$U(\mathbf{r}_2) = \frac{i}{\lambda}\int P(\theta,\phi)e^{-i\mathbf{k}\cdot\mathbf{r}_2}\mathrm{d}\Omega \tag{D.1}$$

where the integral is over the full solid angle subtended by the lens and a complex pupil function $P(\theta,\phi)$ has been introduced to account for the amplitude variation over the spherical wavefront and any aberrations caused by the lens. In summary, the field can be expressed as a superposition of plane waves of different propagation directions within the solid angle subtended by the lens. For a full mathematical justification of this see Gu[35].

Fig. D.2 shows how a commercial lens, following the *sine condition*, maps uniformly distributed rays on a plane wave to a spherical wavefront. It can be seen that the density of rays becomes lower as θ increases and the consequent reduction

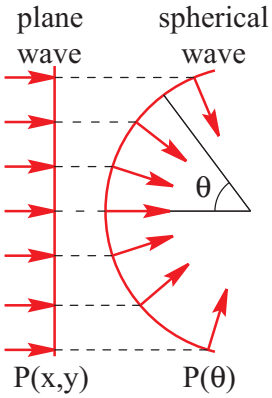

Figure D.2: *This figure shows how a high NA objective lens, following the* sine condition, *maps uniformly distributed rays on a plane wave to a spherical wavefront.*

in amplitude that results from this must be taken into account by modifying the pupil function.

$$P(\theta, \phi) = P(x, y) \cos^{1/2} \theta \qquad \text{...the sine condition} \tag{D.2}$$

where $P(x, y)$ is the pupil function that would have been used in the paraxial case, an example of which is given in Eq. 2.1.

D.2 Vectorial Debye theory

The Debye theory can be developed further to take account of the vectorial nature of the electric field so that theoretical predictions of polarization effects, that become important for high NA lenses, can be made.

Referring to Fig. D.3, a plane wave with arbitrary polarization in the x_1-y_1 plane propagates towards the lens. The polarization of $\mathbf{E}_i$ at any point on the wavefront can be expressed with a radial component along $\hat{\mathbf{r}}$ and azimuthal component along $\hat{\boldsymbol{\phi}}$. According to the Debye theory, each point on this initial wavefront gives rise to a plane wave contribution in the vicinity of the focal point and as illustrated, the lens causes the component along $\hat{\mathbf{r}}$ to be rotated about the $\hat{\boldsymbol{\phi}}$-axis into this new plane

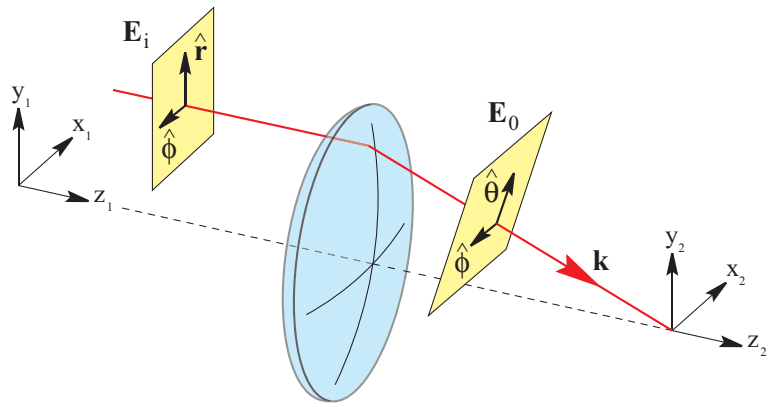

Figure D.3: *During refraction, a lens causes the component of polarization along* $\hat{\mathbf{r}}$ *to be rotated about the* $\hat{\boldsymbol{\phi}}$*-axis into a plane that is at a tangent to the spherical wavefront shown in fig.D.1.*

during refraction. The resulting field therefore has components of polarization along the x_2, y_2 and z_2.

The formal expression for the electric field amplitude near the focal point of a lens that operates according to the sine condition can therefore be expressed as:

$$\mathbf{E}(\mathbf{r}) = \frac{i}{\lambda}\int \mathbf{E}_0 e^{-i\mathbf{k}\cdot\mathbf{r}_2}\cos^{1/2}\theta \mathrm{d}\Omega \tag{D.3}$$

where once again the integration extends over the solid angle subtended by the lens and $\mathbf{E}_0$ is the rotated version of $\mathbf{E}_i$ as shown in Fig. D.3. This can be manipulated further to give:

$$\mathbf{E}(r_2,\phi_2,z_2) = \frac{\pi i}{\lambda}\begin{pmatrix} I_0 + I_2\cos 2\phi \\ I_2 \sin 2\phi \\ -2iI_1\cos\phi \end{pmatrix} \tag{D.4}$$

where the integrals I_0, I_1 and I_2 are defined as:

$$I_0 = \int_0^\alpha \cos^{1/2}\theta\ \sin\theta\ (1+\cos\theta)\ J_0(kr_2\sin\theta)\exp(-ikz_2\cos\theta)\mathrm{d}\theta \tag{D.5}$$

$$I_1 = \int_0^\alpha \cos^{1/2}\theta\ \sin^2\theta\ J_1(kr_2\sin\theta)\exp(-ikz_2\cos\theta)\mathrm{d}\theta \tag{D.6}$$

$$I_2 = \int_0^\alpha \cos^{1/2}\theta\ \sin\theta\ (1-\cos\theta)\ J_2(kr_2\sin\theta)\exp(-ikz_2\cos\theta)\mathrm{d}\theta \tag{D.7}$$

J_0, J_1 and J_2 represent zero, first and second order Bessel functions of the first kind respectively and α is the maximum angle of convergence of the objective lens. These equations are known as the Richards and Wolf integrals [26].

Bibliography

[1] Robert Hooke. *Micrographia: or Some physiological descriptions of minute bodies made by magnifying glasses with observations and inquiries thereupon.* New York: Dover, reprint of the 1st edition edition, 1665(1961).

[2] E. Abbe. Beiträge zur theorie des mikroskops und der mikroskopischen wahrnehmung. *Archiv für mikroskopische Anatomie (printed for John Martyn)*, 9:413–668, 1873.

[3] T. Wilson and C.J.R. Sheppard. *Theory and practice of Scanning Optical Microscopy.* Academic Press, London, 1984.

[4] Tony Wilson. *Confocal Microscopy.* Academic Press, 1990.

[5] M. Minsky. Microscopy apparatus. *United States Patent No.3,013,467*, 1961.

[6] M. Petráň, M. Hadravsky, M. Egger, and R. Galambos. Tandem-scanning reflected-light microscopy. *J. Opt. Soc. Am.*, 58:661–664, 1968.

[7] G. Brakenhoff, P. Blom, and C. Bakker. Confocal scanning light microscopy with high aperture optics. *Proc. ICO Conf., Madrid, Spain*, pages 215–218, 1978.

[8] G. Brakenhoff, P. Blom, and C. Bakker. Confocal scanning light microscopy with high aperture immersion lenses. *J. Microscopy*, 117:219–232, 1979.

[9] W. J. Denk, J. P. Strickler, and W. W. Webb. Two-photon laser scanning fluorescence microscopy. *Science*, 248:73–76, 1990.

[10] D. H. Burns, R. B. Hatangadi, and F. A. Spelman. *Scanning*, 12:156–160, 1990.

[11] G. J. Brakenhoff and K. Visscher. Confocal imaging with bilateral scanning and array detectors. *J. Microsc.*, 165:139–146, 1993.

[12] J. C. Maxwell. On the general laws of optical instruments. *Quart. J. Pure Appl. Maths.*, 2:233–246, 1858.

[13] G. Toraldo di Francia. Super-gain antennas and optical resolving power. *Nuovo Cimenta Suppl.*, 9:426–438, 1952.

[14] Z. Zalevsky and D. Mendlovic. *Optical Superresolution.* Springer, 2004.

[15] M. A. A. Neil, R. Juškaitis, T. Wilson, Z. J. Laczik, and V. Sarafis. Optimized pupil-plane filters for confocal microscope point-spread function engineering. *Optics Letters*, 25:245–247, 2000.

[16] M. J. Booth, M. A. A. Neil, R. Juškaitis, and T. Wilson. Adaptive aberration correction in a confocal microscope. *Proceedings of the National Academy of Science*, 99:5788–5792, 2002.

[17] S. Quabis, R. Dorn, M. Eberler, O. Glockl, and G. Leuchs. Focusing light to a tighter spot. *Optics Communications*, 179:1–7, 2000.

[18] M. A. A. Neil, F. Massoumian, R. Juškaitis, and T. Wilson. Method for the generation of arbitrary complex vector wavefronts. *Optics Letters*, 27:1929–1931, 2002.

[19] T. Wilson. "Active and adaptive optics in confocal microscopy" in *"Nanophotonics"(H. Masuhara and S. Kawata-Eds.)*. Elsevier, 2004.

[20] L.M. Soroko. *Meso-Optics*. World Scientific, 1996.

[21] W.T. Welford. Use of annular aperture to increase focal depth. *J. Opt. Soc. Am.*, 50:749–, 1960.

[22] C. J. R. Sheppard and T. Wilson. Imaging properties of annular lenses. *Appl. Opt.*, 18:3764–3769, 1979.

[23] Max Born and Emil Wolf. *Principles of Optics*. Pergamon Press, 6th edition, 1983.

[24] L.M. Soroko. *Axicons and meso-optical imaging devices" in "Progress in Optics Vol.28" (E. Wolf (Ed.))*. North-Holland, 1989.

[25] J. W. Goodman. *Introduction to Fourier Optics*. McGraw-Hill, 2nd edition, 1996.

[26] E. Wolf and B.Richards. Electromagnetic diffraction in optical systems 2 - structure of the image field in an aplanatic system. *Proc, Roy. Soc. A*, 253, 1959.

[27] T. Wilson, R. Juškaitis, and P. Higdon. The imaging of dielectric point scatterers in conventional and confocal polarisation microscopes. *Optics Communications*, 141:298–313, 1997.

[28] D. Birchon. *Optical Microscopy Technique*. Newnes, London, 1961.

[29] W. Göbel, B.M. Kampa, and F. Helmchen. Imaging cellular network dynamics in three dimensions using fast 3d laser scanning. *Nature Methods*, 4(1):73–79, 2007.

[30] N. Callamaras and I. Parker. Construction of a confocal microscope for real-time x-y and x-z imaging. *Cell Calcium*, 26:271–279, 1999.

[31] H. Oku, K. Hashimoto, and M. Ishikawa. Variable-focus lens with 1-khz bandwidth. *Opt. Express*, 12:2138–2149, 2004.

[32] B. Qi, A. Phillip Himmerb, L. Maggie Gordonc, X.D. Victor Yangc, L. David Dickensheets, and I. Alex Vitkina. Dynamic focus control in high-speed optical coherence tomography based on a microelectromechanical mirror. *Opt. Comm.*, 232:123–128, 2004.

[33] G.D. Reddy and P. Saggau. Fast three-dimensional laser scanning scheme using acousto-optic deflectors. *J. Biomed. Opt.*, 10:064038, 2005.

[34] E. Botcherby, R. Juškaitis, M. Booth, and T. Wilson. Aberration-free optical refocusing in high numerical aperture microscopy. *Opt. Lett.*, 32(14):2007–2009, 2007.

[35] Min Gu. *Advanced Optical Imaging Theory.* Springer, 1999.

[36] C. J. R. Sheppard. Aberrations in high aperture systems. *Optik*, 105:29–33, 1997.

[37] V. N. Mahajan. *Optical Imaging and Aberrations, Part II. Wave Diffraction Optics.* SPIE, Bellingham, Wash, 2001.

[38] D. Shin, A. Chavez-Pirson, S. Kim, S. Jung, and Y. Lee. Diffraction by a subwavelength-sized aperture in a metal plane. *J. Opt. Soc. Am. A*, 18:1477–1486, 2001.

[39] R. Juškaitis. "Characterising high numerical aperture microscope lenses" in *"Optical imaging and microscopy Techniques and advanced systems" (P. Török and F. Kao - Eds.).* Springer, 1 edition, 2003.

[40] R. Juškaitis. "Measuring the real point spread function of high numerical aperture microscope objective lenses" in *"Handbook of biological confocal microscopy"(J. Pawley-Ed.).* Springer, 3 edition, 2006.

[41] W. Lukosz. Optical systems with resolving powers exceeding classical limit. *J. Opt. Soc. Am.*, 56(11):1463–1472, 1966.

[42] J.A. Concello and J. W. Lichtman. Optical sectioning microscopy. *Nat. Methods*, 2:920–931, 2005.

[43] T. Wilson. M. A. A. Neil, R. Juškaitis. Method of obtaining optical sectioning by using structured light in a conventional microscope. *Optics Letters*, 22:1905–1907, 1997.

[44] P. A. Stokseth. Properties of a defocused optical system. *J. Opt. Soc. Am.*, 59:1314–, 1969.

[45] A. Zumbusch, G.R. Holtom, and X.S. Xie. Three-dimensional vibrational imaging by coherent anti-stokes raman scattering. *Phys. Rev. Lett.*, 82:4142–4145, 1999.

[46] M.D. Duncan, J. Reintjes, and T.J. Manuccia. Scanning coherent anti-stokes raman microscope. *Opt. Lett.*, 7:350–352, 1982.

[47] I. Freund and M. Deutsch. Second-harmonic microscopy of biological tissue. *Opt. Lett.*, 11:94–96, 1986.

[48] L. Moreaux, O. Sandre, M. Blanchard-Desce, and J. Mertz. Membrane imaging by simultaneous second-harmonic generation and two-photon microscopy. *Opt. Lett.*, 25:320–322, 2000.

[49] Y. Barad, H. Eisenberg, M. Horowitz, and Y. Silberberg. Nonlinear scanning laser microscopy by third harmonic generation. *Appl. Phys. Lett.*, 70:922–924, 1997.

[50] J.A. Squier, M. Müller, G.J. Brakenhoff, and K.R. Wilson. Third harmonic generation microscopy. *Opt. Express*, 3:315–324, 1998.